

Beyond the Local Volume: Surface Densities of Ultracool Dwarfs in Deep HST/WFC3 Parallel Fields

CHRISTIAN AGANZE,¹ ADAM J. BURGASSER,¹ MATHEW MALKAN,² CHIH-CHUN HSU,¹
CHRISTOPHER A. THEISSEN,¹ DANIELLA C. BARDALEZ GAGLIUFFI,³ RUSSEL RYAN,⁴ AND
BENNE HOLWERDA⁵

¹*Department of Physics, University of California, San Diego, CA 92093, USA*

²*Department of Physics & Astronomy, University of California, Los Angeles, CA 90095, USA*

³*Department of Astrophysics, American Museum of Natural History, Central Park West at 79th Street, NY 10024, USA*

⁴*Space Telescope Science Institute, 3700 San Martin Dr., Baltimore, MD 21218*

⁵*Department of Physics and Astronomy, 102 Natural Science Building, University of Louisville, Louisville KY 40292, USA*

ABSTRACT

Ultracool dwarfs (UCDs) of the L, T, and Y spectral classes are the lowest-mass and coldest objects in the Milky Way. Like stars, they are tracers of Galactic structure and star-formation history, while the cooling of substellar UCDs provide additional probes for galactic archeology and chemical evolution. Wide-field optical and infrared surveys have uncovered thousands of UCDs, but primarily in the immediate solar neighborhood ($d < 100$ pc). To push to larger distances, we have searched over 0.5 deg^2 of the WFC3 Infrared Spectroscopic Parallel Survey and the 3D-HST parallel survey with low-resolution near-infrared spectra. We report the discovery of 193 M7-T9 and T dwarfs with spectro-photometric distances up to ~ 2 kpc for L dwarfs and ~ 400 pc for T dwarfs. We model the number density distribution with population simulations incorporating various assumptions of the intrinsic MF and birth rates, accounting for UCD evolutionary models and Galactic structure. We find observations generally con-

sistent with predictions from different two sets of evolutionary models. We find the scale height of L dwarfs to be 20–300 pc while the T dwarf scale height is ≥ 400 pc. Future infrared sky surveys conducted with the James Webb Space Telescope (JWST) or the Euclid mission will put finer constraints on the luminosity of UCDs at large distances. We predict that Euclid will yield $\sim 10^3 - 10^4$ L and T dwarfs spectra in the Euclid South and Euclid Fornax fields alone for a limiting magnitude of J=24, providing enough statistics to fully characterize UCDs in the Galactic context.

1. INTRODUCTION

The structure and evolution of the Milky Way is largely inferred from heterogeneous spatial and kinematic distributions of its stars. Star-count data show that the overall structure conforms to a younger population fit to one or more exponential disks and an older population fit to a power-law or oblate spheroid (de Vaucouleurs & Pence 1978; Bahcall & Soneira 1981; Jurić et al. 2008); and models show that the disk started forming stars 8–11 Gyr ago, while the halo star-formation history dates to 10–13 Gyr ago from possible multiple merger events. Hence, halo stellar populations contain stars with ages comparable to the age the universe (Leggett et al. 1998; Tolstoy et al. 2009; Haywood et al. 2013). Questions relating to the formation and evolution of the Galaxy through its stars constitute the field of Galactic archeology (Freeman 1987; Ivezić et al. 2012), which, through the usage of large sky surveys (e.g the Sloan Digital Sky Survey, York & Others 2000), has enabled a 6-dimensional depiction of the Galaxy. The Gaia mission (Gaia Collaboration et al. 2018) has recently contributed to our understanding of the Milky Way. Some of the notable discoveries include major merger events that formed the inner stellar halo and thick disk (Gaia-Enceladus/Gaia sausage: Helmi et al. 2018; Belokurov et al. 2018; Myeong et al. 2018; Gallart et al. 2019, and the Sequoia event: Myeong et al. 2018, 2019), the discovery and characterization of hypervelocity stars (Boubert et al. 2018), stellar streams as probes of the Galactic potential and dark matter profile (Boubert et al. 2018; Malhan et al. 2018; Koppelman et al. 2019). The Gaia mission has also enabled the discovery of substructure

in the solar neighborhood in the galactic disk caused by phase mixing in velocity space, from possible interactions with the spiral structure of the Galaxy (Antoja et al. 2018).

Ultracool dwarfs (UCDs; $M \lesssim 0.1 M_{\odot}$, $T_{eff} \lesssim 3000\text{K}$; Kirkpatrick 2005) provide a new approach for studying the Galaxy (Burgasser 2004; Ryan et al. 2017). They constitute $\sim 50\%$ of the total number of stars and they are abundant in every environment in the Galaxy (Cruz et al. 2007b; Chabrier & Baraffe 2000; Burrows et al. 2001; Bochanski et al. 2010). Stellar UCDs have lifetimes far in excess of the age of the Galaxy ($> 10^3$ Gyr, Laughlin et al. 1997), while substellar UCDs (brown dwarfs) do not fuse hydrogen and hence cool down with time (Hayashi & Nakano 1963). They have distinct spectra shaped by strong molecular absorption bands that are highly sensitive to temperature, surface gravity and metallicity. The evolution of UCDs provides potential age diagnostics that have already been exploited in stellar cluster studies (Basri 1998; Luhman & Mamajek 2012; Martin et al. 2017) and searches of young moving groups near the Sun (Lopez-Santiago et al. 2006, Gagné et al. 2015, Mamajek 2015, Faherty et al. 2018).

UCDs have historically been discovered in red optical and infrared sky surveys (DENIS: Delfosse et al. 1999, SDSS: Schmidt et al. 2010, 2014; Theissen et al. 2017, VISTA: Lodieu et al. 2012; Downes et al. 2014; 2MASS: Cruz et al. 2007b; Kirkpatrick et al. 2010, WISE: Kirkpatrick et al. 2011; Cushing et al. 2011, UKIDSS: Marocco et al. 2015; Day-Jones et al. 2013; Birmingham et al. 2013; Skrzypek et al. 2016, CFHT-LAS: Reyle et al. 2010, Gaia: Reylé 2018; Kiman et al. 2019) but due to their intrinsic faintness, these samples are distance limited ($\leq 100\text{pc}$). Hence, efforts to measure the UCD luminosity function have focused on compiling volume-limited samples within 20–25 pc of the sun (Cruz et al. 2007b; Metchev et al. 2008; Reyle et al. 2010; Kirkpatrick et al. 2019; Bardalez Gagliuffi et al. 2019). Wide-field surveys provide large samples of UCDs, however, these studies do not effectively probe Galactic structure, nor the oldest UCD populations that formed in the early metal-poor Galaxy which may have had a distinct initial mass function (Bate et al. 2002; Bromm & Loeb 2003; Bate et al. 2003). To investigate the complete UCD population of the Galaxy these scenarios, it is necessary to identify UCDs populations beyond the solar neighborhood and further into the thick disk and halo of the Milky Way.

Deep pencil-beam imaging surveys provide a novel approach to use star-count data in characterization of UCD populations beyond the local volume. A common approach is to use photometric selections cuts anchored to known sample. Early work by [Gould et al. \(1997\)](#) conducted an M-dwarf number counts to measure the halo luminosity function of the Hubble Space Telescope's Wide Field Camera 2 (HST-WFC2) and Planetary Camera (PC1) Deep Fields. They found 47 M dwarfs with $M_V > 13.5$, and the distribution was consistent with a power law the mass function that turns at $M \sim 0.6 M_\odot$ from $\alpha = -1$ to $\alpha = 0.44$. Subsequent studies by [Kerins \(1997\)](#); [Chabrier & Mera \(1997\)](#) concluded that the contribution of low-mass stars ($M \sim 0.3 M_\odot$) to the halo luminosity function is less than 1%. [Ryan Jr. et al. \(2005\)](#) searched 15 deep parallel fields from the Hubble Space Telescope star-count optical data obtained with the ACS instrument, selected by their i-z colors. They estimated a scale of ~ 350 pc for L & T dwarfs. Later work by [Ryan et al. \(2011\)](#) found 17 late M, L and T dwarfs in 231.90 arcmin^2 of WFC3 imaging of the GOODS fields using a combination of wide and narrow-band filter colors. They estimated a disk scale height of $290 \pm 39 \text{ pc}$ consistent with work by [Pirzkal et al. \(2005\)](#). In addition to poor estimate of spectral types, these samples were contaminated with various non-stellar sources that could not be identified in the absence of spectral information. To push towards a larger and pure sample, [Holwerda et al. \(2014\)](#) identified 274 in 227 arcmin^2 M-dwarfs (to a limiting magnitude F125W=25) from the HST-WFC3 Brightest of Re-ionizing Galaxies (BoRG, [Pirzkal et al. 2009](#)) survey, using an optical and near-infrared colors and determined their spectral types using V-J color-M-dwarf subtype relation ([Pirzkal et al. 2009](#)). They found a slightly higher density of M-dwarfs identified in the Northern fields compared to the Southern Fields, and a disk scale-height of $0.3\text{--}4 \text{ kpc}$ with a dependence on subtype. The overall M-dwarf scale height was ~ 600 pc, a number that is much larger than previous estimates mostly due to large uncertainties in the fit. [Van Vledder et al. \(2016\)](#) reanalyzed these data using a Markov Chain Monte Carlo method to fit the statistic to a galactic model including a thin disk, thick disk, and halo component. They derived a scale height of $290_{-19}^{+20} \text{ pc}$ and a central number density of $0.29_{-0.13}^{+0.20} \text{ pc}^{-3}$, with no correlation of model parameters with M-dwarf subtype, and consistent with previous studies. However, these studies do not probe statistics for later types. Recent work by [Sorahana et al. \(2018\)](#)

found 3665 L dwarfs brighter than $z=24$ by searching 130 square degrees of the Hyper Suprime-Cam Subaru Strategic Program data and found an average L-dwarf scale height of 340–420 pc. [Carnero Rosell et al. \(2019\)](#) compiled a list of 11,745 photometrically classified L0-T9 dwarfs distances up to ~ 400 pc by searching $\sim 2,400$ deg 2 of the Dark Energy Survey (DES) data at a limiting magnitude of $z=22$. They estimated a large scale height of ~ 450 pc. These last two studies provide another constraint on the number density of L dwarfs in the Galaxy using large samples ($N>10^3$); however, as in many imaging surveys, poor accuracy in spectral types significantly affects the derived parameters. Ultimately, the large uncertainties on spectral types of UCDs in imaging surveys poorly constrain their distances, and deep spectroscopic follow-up of these sources is not a priority for precious HST time.

A parallel approach is to use deep pencil beam samples of spectra in red optical and near infrared (NIR) with no prior selection of source type. NIR spectroscopy, in particular, samples the peak of UCD spectral energy distributions and measure broad molecular features that guide UCD classification schemes ([Kirkpatrick 2005](#)). [Pirzkal et al. \(2005\)](#) identified 18 late M and 2 L dwarfs in the Hubble Ultra Deep Field (HUDF) and estimated their spectral types by fitting templates from [Kirkpatrick et al. \(2000\)](#) to their Gradient-Assisted Photon Echo Spectroscopy (GRAPES, ref) taken with the xxx instrument (ref). This study inferred a disk scale height of 400 ± 100 pc for M and L dwarfs. Another study by [Pirzkal et al. \(2009\)](#) used deep Advanced Camera for Surveys (ACS) slitless grism observations of the Probing Evolution And Reionization Spectroscopically (PEARS) fields (as part the Great Observatories Origins Deep Survey (GOODS) fields, [Giavalisco et al. 2004](#)) down to a $z=25$ and spectroscopically identified 43 M4-M9 dwarfs. Using a thick and thin disk model, the study estimated a scale height for the thin disk of ~ 370 pc, and ~ 100 pc for the thick disk, a halo fraction between 0.00025–0.0005 consistent with previous estimates.

[Masters et al. 2012](#) discovered 3 late T dwarfs the WFC3 infrared Spectroscopic Survey (WISPS) fields ([Atek et al. 2010](#)) identified by their strong CH₄ and H₂O absorption features. The sample size was not large enough to put meaningful constraints on the scale height or the luminosity function L

and T dwarfs beyond the local volume. In this paper, we expand upon this study by developing an effective method to select UCDs in similar surveys.

Section 2 describes the data, section 3 describes the selection process, section 4 discusses the result compared to a Monte-Carlo simulation

2. DATA

We obtained data from two surveys: the WFC3 Infrared Spectroscopic Parallel Survey (WISPS, Atek et al. 2010) and 3D-HST (Momcheva et al. 2016, Brammer et al. 2012a, Skelton et al. 2014). These two surveys used the IR channel of the WFC3 camera (Kimble et al. 2008) providing low-resolution G102 ($\lambda = 0.8\text{--}1.17 \mu\text{m}$, $R \sim 210$) and G141 ($\lambda = 1.11\text{--}1.67 \mu\text{m}$, $R \sim 130$) grism spectra. Removal of the slit mask allows for the overlapping spectra of the 136×123 arcsec inner FOV of the WFC3 camera. Figure ?? shows an WCF3 exposure of one of fields in WISP.

2.1. 3D-HST survey data

3D-HST a parallel survey of 248-orbits spanning ~ 600 arcmin 2 as part of Hubble Cycles 18 & 19. This survey targets four standard deep extra-galactic fields: The All-wavelength Extended Groth Strip International Survey (AEGIS, Davis et al. 2007), Cosmic Evolution Survey (COSMOS, Scoville et al. 2007), Ultra-Deep Survey(UKIDSS-UDS, Lawrence & Others 2007), the Great Observatories Origins Deep Survey (GOODS-South and GOODS-North, Giavalisco et al. 2004), using the ACS/G800L and WFC3/G141 grisms in parallel. The goal of 3D-HST is to obtain as the the Cosmic Assembly Near-infrared Deep Extragalactic Legacy Survey(CANDELS survey, Grogin et al. 2011, Koekemoer et al. 2011. However, 3D-HST is only 70% of the total footprint of the CANDELS. Photometric catalog data products are described in Skelton et al. (2014) and combined data products in Momcheva et al. (2016)

The pointings for 3D-HST are designed to cover CANDELS area, therefore there are additional ground-based and space-based photometry from various other surveys in several optical and infrared filters. Each pointing in 3D-HST is observed by two orbits using the G141 grism and the F140W filter with typical exposure times of 5000 s for G141 AND 800 s for F140W. Observations for most

of the pointings in the survey were conducted from October 2010 to November 2012. However, the GOODS-North field is a part of the A Grism H-Alpha SpecTscopic survey (AGHAST, GO-11600; PI: Wiener) and was observed between sept 16 2009 and sept 26 2010 and re-observed on April 19 and 24 2011, due artifacts and background issue, with exposure times of 800 s for F140W AND 5200S in G141.

Data reduction in 3D-HST involves reducing the both the direct F140W images and G141 grism images. The full description of the image reduction pipeline is described by Brammer et al. (2012b), Skelton et al. (2014) and Momcheva et al. (2016). Raw images were downloaded and passed through a pipeline that consists of removing satellite trails and artifacts through visual inspection, background -subtraction and flat-fielding. The main physical sources of time-dependent background are zodiacal continuum, scattered light and persistence from He emission at 1.083 micron. Both the reduction of the F140W and G141 images involved combining at most four dithered images. A standard method uses a drizzling algorithm implemented by the AXe software (Kuntschner et al. 2013; Kümmel et al. 2009). However, drizzling is designed to work well for a large number of images. The shortcomings of this method include the introduction of correlated noise between adjacent pixels. To avoid these issues, 3D-HST stacked all the dithered images onto one grid, given that the dithered images are all separated by the same number of pixels by the design of the survey. In addition, reducing the grism images require a reference image (different from the obtained F140W direct image) to generate a contamination global model of each pointing, to separate overlapping spectra and orders. The reference image was obtained by coming F125W, F140W AND F160W images of that pointing obtained from Skelton et al. (2014) data products, where the magnitudes of all objects in the fields are scaled to the F140W zero-point, and errors properly propagated. Based on the morphology and the magnitude of each source in the reference image, the full 2D-spectrum of each object was modeled from a 1D SED. This contamination model was then used to correct for overlapping spectra and orders. These 2D-spectra of exactly 312 pixels each are then extracted. The reference image and the direct images are on the same grid, therefore no source matching was required for source identification.

We used data products described by Momcheva et al. (2016) and the photometric catalog of sources in Skelton et al. (2014) retrieved from the survey’s website ¹. The extracted 1D spectra in 3D-HST survey are not continuum-corrected as shown in Figure 5. We obtained a correct continuum of each 3D-SHT spectrum by dividing the flux of the spectrum and the sensitivity curve of the detector provided in the data. We did not perform any additional reduction to the data.

2.2. *WISP survey data*

The WISP survey is a 1000-orbit HST pure-parallel survey covering 390 fields ($\sim 1500 \text{ arcmin}^2$) that follows observing programs accepted on the Cosmic Origins Spectrograph (COS) and Space Telescope Imaging Spectrograph (STIS). The survey’s observing strategy as well as data-reduction is described in Atek et al. (2010). The goal of WISPS is to conduct a census of star-forming high-redshift galaxies. The fields in WISPS were chosen away from the galactic plane and 5.5 and 4.75 arcmin away from the fields of COS and STSIS. Given the pure-parallel nature of this survey, the fields are observed in G102, G141 grism with no dithering between exposure. Reference images were also taken using F110W (corresponding to G102) and F140W (corresponding to G141) imaging cameras. To reach the same depth in both G102 and G141, the ratio of exposure times was fixed at 2.4:1, while the exposure ratio of exposure times for imaging and grism is 6:1.

Data reduction and grism extraction was performed using a combination of **AXe** software (Kuntschner et al. 2013; Kümmel et al. 2009) and custom IDL pipelines to remove additional background and to flag bad pixels. The main sources of background are zodiacal light, and earth thermal emissions. Grisms spectra in WISPS have little crowding of the same fields given their high galactic latitudes, but multiple spectral orders do overlap. WISPS provides an estimate of contamination of each spectrum computed using **AXe** and source catalogs in WISPS were generated using SExtractor (Bertin & Arnouts 1996). We obtained WISPS G102 and G141 grism data as well as broad-band

¹ <https://3dhst.research.yale.edu/Home.html>

F110W, F140W, F160W photometric data and source catalogs from the Mukuliski Archive for Space Telescope (MAST^{[2](#)}).

3. SELECTION OF UCDS

3.1. *Calibration Samples*

To discover new UCDS in the WISPS & 3D-HST data, we created a calibration sample of known UCDS, with similar features, e.g spectral coverage and resolution. We obtained 2056 M7-T9 low-resolution (\sim 75-120), NIR (0.9-2.5 μ m) spectra of nearby brown dwarfs with median SNR $>$ 10 from the SpeX Prism Library (SPL, Burgasser 2014a, ^{[3](#)}) of UCDS. We will refer to this sample as the templates/SpeX sample. In addition, we compiled a list other UCD spectra taken with the same instrument. We used the 77 UCDS from Manjavacas et al. (2018) observed with the WFC3. Finally, we obtained a list of 22 Y dwarfs obtained by Schneider et al. (2015) using the WFC3 camera.

3.2. *Pre-selection*

3.2.1. *Point-source Cut*

We combined all grism data and photometry from the two surveys and obtained a total of 271915 objects that have corresponding photometry in the provided photometric catalogs. To narrow down our selection, point sources were identified using `Source Extractor`'s stellarity index `CLASS_STAR` \neq 0. 3D-HST provides an additional `star_flag` flag for point-sources based on their F160W magnitudes and the flag `FLUX_RADIUS`, but we find that this flag eliminates 3 UCDS from 3D-HST in the selected sample of UCDS, hence the flag was ignored. We reduced the sample down to 110930 spectra, that is 40.7% of the total number of spectra.

3.2.2. *J-band SNR rejection*

UCDs display a strong H₂O and CH₄ molecular absorption features in the J and H bands (1.1-1.6 μ m). We do not expect other objects in this survey to display similar molecular broad features, hence

² <https://archive.stsci.edu/prepds/wisp/>

³ <https://cass.ucsd.edu/~ajb/brownndwarfs/spexprism/library.html>

to narrow down our selection, we defined a signal-to-noise ratio in the J-band continuum (hereafter J-SNR) for $1.2 \mu\text{m} \leq \lambda \leq 1.3 \mu\text{m}$. This J-SNR captures the amount of flux in the J-band, hence we eliminated the lowest SNR objects by making a cut at J-SNR=3 retaining 46370 spectra/grisms, that is 38.7% of the original point-source sample and 15.8% of the total number of spectra including extended objects. We also measured the J-SNR for all the spectra in our calibration samples in a similar fashion.

3.3. Spectral Fitting and F-test

A quick look through data shows that the type of expected contaminants after the point-source cuts includes miss-classified galaxies and emission lines, flat spectra that corresponds to very low SNR objects and/or the continuum of other objects that show features in wavelength regions outside 1.1-1.6 μm , and other artifacts. To further narrow down our selection of UCD after the J-SNR cut, we fitted each spectrum to UCDs SpeX spectra of standards using a χ^2 minimization method, following the method of Kirkpatrick et al. (2010). Hence, we obtained a spectral type classification all point-sources. We also compared every spectrum to a straight line in the same wavelength region and measured χ^2 . These two fits help distinguish between spectra that could potentially have absorption features in this region, and spectra that have no interesting features spectra in this wavelength region. The χ^2 of a line (χ_L^2) or a standard (χ_T^2) is given by

$$\chi_L^2 = \sum_{\lambda=1.15\mu\text{m}}^{1.65\mu\text{m}} \frac{(a + b\lambda - \text{Sp})^2}{\sigma^2} \quad (1)$$

$$\chi_T^2 = \sum_{\lambda=1.15\mu\text{m}}^{1.65\mu\text{m}} \frac{(\text{Sp} - \alpha T)^2}{\sigma^2} \quad (2)$$

α is scale-factor defined as

$$\alpha = \sum_{\lambda=1.15\mu\text{m}}^{1.65\mu\text{m}} \frac{(\text{Sp} - \alpha T)^2}{\frac{T^2}{\sigma^2}} \quad (3)$$

$\text{Sp}(\lambda)$ is a WISP or 3D-HST spectrum and σ^2 is the noise in the WISP or 3D-HST spectrum a and b are the parameters of the best-fit line from least-squares and T is the template.

We used an F-test as a statistical hypothesis testing static to separate noisy/linear spectra from the rest of the sample implemented. We decided to eliminate sources with $F(\chi_s^2/\chi_l^2) < 0.4$ meaning that the probability of the standard being a better fit to the spectrum than a line is <than 40%. This cut yields only 8148 objects, that is 18.9% of point-sources with $J\text{-SNR} > 3$, 7.3% of all point-sources and 3% of the original number of spectra we obtained from both surveys. These three steps eliminated most of the noisy contaminants.

3.4. Spectral Indices

After eliminating noisy and possible extra-galactic contaminants, we narrowed down the selection to true UCDs. As mentioned, UCDs display strong CH₄ and H₂O molecular features in 1.1 μm <λ < 1.7 μm region (Burgasser 2001). Spectral Indices have traditionally been used to determine spectral types (Tokunaga & Kobayashi 1999, Cushing et al. 2000, Allers et al. 2007, Burgasser et al. 2007). Thus, we defined spectral indices in five wavelength bands: 1.15–1.20 μm, 1.246–1.295 μm, 1.38–1.43 μm, 1.56–1.61 μm, or 1.62–1.67 μm; denoted by H₂O-1, J-Cont, H₂O-1, H-Cont, and CH₄ respectively. Each index is the ratio of the median flux in these bands and the uncertainties for each index are estimated by random sampling, assuming these uncertainties are Gaussian-distributed. The index is given by

$$\text{Index} = \frac{\langle F(\lambda_1 < \lambda < \lambda_2) \rangle}{\langle F(\lambda_1 < \lambda < \lambda_2) \rangle} \quad (4)$$

, where at each wavelength i, we draw fluxes normally distributed according to the noise in the spectrum:

$$\{F(\lambda_i)\} \sim \text{Normal}(\langle F(\lambda_i) \rangle, \sigma(\lambda_i)) \quad (5)$$

. $\sigma(\lambda_i)$) is the noise at that wavelength, and $\langle F(\lambda_i) \rangle$ is the flux at that wavelength.

After defining these indices based on the features of interest, we created a selection method that we will refer to as selection criteria. We defined these selection criteria using geometric boxes/parallelograms in each of a given 2-dimensional index-index space. We expect UCDs with similar spectral types to cluster or follow a linear trend away from the contaminants, while the evolution of the relative strength H₂O and CH₄ bands with subtype should distinguish subtype classes.

We chose the following to group objects in the following subtypes: M7-L0, L0-L5, L5-L0, T0-T5, T5-T9, Y dwarfs and subdwarfs.

To define the parameters of each box, we fitted a characteristic line to each index pair (x-index, y-index) within a subtype, defining the slope/direction of the box: $y = m \times x\text{-index} + b$. Each box has four vertices (v_1, v_2, v_3, v_4) . These vertices are computed as $v_1 = (x_{\min}, y_{\max})$, $v_2 = (x_{\min}, y_{\min})$, $v_3 = (x_{\max}, y_{\max})$, $v_4 = (x_{\max}, y_{\min})$, where $(x_{\max}, x_{\min}) = \text{median}(x\text{-index}) \pm 3 \times \text{std}(x\text{-index})$. On the x-axis, if x_{\max} is greater than the maximum of x-index, or if x_{\min} is less than the minimum of the x-index, we set x_{\min} and x_{\max} and the minimum and maximum of x-index. The extent of the boxes on the y-axis are determined by $(y_{\max}, y_{\min}) = m \times (x_{\max}, x_{\min}) + b \pm 0.4 \times dy$, where dy is the range of y-index ($\text{max}(y\text{-index}) - \text{min}(y\text{-index})$). This simple algorithm allows our selection boxes to enclose most of the objects in the subtype, avoid outliers but not extend too far from away the defining sample. For M, L dwarfs, however, we used rectangular boxes, for their simplicity where the vertices were determined in the same manner but with a slope of zero for the line ($m=0$) and a y-intercept of $b = \text{median}(y\text{-index})$.

To assess the effectiveness of this method, we defined a completeness based on our calibration samples and a contamination statistic as follows:

$$CP = \frac{TEMP_s}{TEMP_{tot}} \quad (6)$$

$$CT = \frac{WFC3_s}{WFC3_{tot}} \quad (7)$$

where $TEMP_s$ is the number of templates selected by the box, $TEMP_{tot}$ is the total number of SpeX templates, $WFC3_s$ is the number of WISPS and/or 3D-HST spectra selected by the box, $WFC3_{tot} = 8148$ is the total of spectra. We only employed criteria with the lowest contamination and highest completeness to select UCDs.

As a naming convention, each criteria is named by the ratio of any two indices on the x-axis and the y-axis. To select Y dwarfs, indices are defined by adding the strength of H₂O and CH₄ bands given that these features are weak for these subtypes. For the rest of the subtypes, we defined one best

selection criteria with the lowest contamination and with $\sim 90\%$ completeness; they are summarized in Table 2. The best selection criteria for each subtype are: (H_2O-1/J -Cont, H_2O-2/H_2O-1) for L0-L5 measuring the strength of H_2O relative to the J-continuum, (H_2O-1/J -Cont, CH_4/H -Cont) for L5-T0 measuring the strength of H_2O and CH_4 relative to both the J and H-continua, (H_2O-1/J -Cont, CH_4/H_2O-1) for M7-L0 measuring the strength of H_2O and CH_4 relative to the J-continuum, (H_2O-2/J -Cont, H -cont/J-Cont) for T0-T5 subtypes measuring the strength of H_2O in the H-band and CH_4 relative to both continua, (H_2O-2/J -Cont, CH_4/H -Cont) for T5-T9 measuring the strength of CH_4 relative to both continua, and (H_2O-1/J -Cont, H -cont/J-Cont) for subdwarfs measuring the strength of H_2O and CH_4 relative to the J-continuum. There are 45 possible combinations of these 10 index ratios but we chose these for their low contamination. Finally, to select Y dwarfs, as stated, we added the strength of H_2O and CH_4 in both bands given the flux in these regions for Y dwarfs is extremely weak. The index of choice is ($H_2O-2+CH_4/J$ -contm $H_2O-1+CH_4/H$ -cont) for Y dwarfs. Having decided on the selection criteria, we applied these to the 8148 objects. We selected a total of 2174 objects for visual inspection selected per subtype as follows: L0-L5=530, L5-T0=437, M7-L0=1413, T0-T5=160, T5-T9=14, Y dwarfs=19, subdwarfs=314. The greatest contribution to the contamination comes from the M7-L0 box given the relative weakness of absorption features for these earlier types.

As a final step, after all selection has been applied, we visually inspected all the candidates UCDs to confirm their spectral type, and to remove missed outliers. We estimated the false positive rates for our methods after visual inspection and characterization of the UCDS. The false positive rate (FP) is given by

$$FP = 1 - \frac{WFC3_{true}}{WFC3_s} \quad (8)$$

where $WFC3_{true}$ is the total number of objects that are in the spectral type range, and that are true UCDs. Our best selection criteria all have FPs between 70-100% which is to be expected given the number of true UCDs is much smaller than the number of spectra. Nevertheless, the number of spectra targeted for visual contamination have been down-selected from >200000 to ~ 2000 .

3.5. Random Forest Classifier

[MIGHT HAVE TO REMOVE THIS SECTION] As an alternative to using selection boxes in 2D-space, we trained a random forest classifier by deploying `RandomForestClassifier` implementation by `scikit-learn` (Pedregosa et al. 2012) to classify potential UCDs in both surveys. Random forests have been shown to reliably predict M-dwarf subtypes based on their photometric colors (Hardegree-Ullman et al. 2019), which are analogous to spectral indices. In addition, random forests have been proven to perform star-galaxy classification in transient surveys, using photometry alone (Miller et al. 2017). Random forest algorithms use a set of independent decision trees constructed from a random choice of features, they assign a final label by averaging the classifications obtained by each decision tree. Furthermore, random forests are practical method to classify large datasets, given that the algorithm is relatively fast, unbiased by noisy features. We constructed a training set of 6308 objects made of 3612 visually inspected contaminants obtained from several iteration of the box-selection method, 2677 objects from the spex-prism library and 19 objects from the Schneider set. We labeled these sources using two labels: UCDs, which are objects with spectral types $\geq M6$, and non-UCDs which are objects with spectral types $\leq M6$ and/or part of the set of visually confirmed contaminants. Although the difference between an M6 UCD and M7 UCD is not as rigid, we make this cut to reduced biases in selection objects with subtypes $\geq M7$. In addition, all objects in the training set have a J-SNR ≥ 3 . This labeling results in 4009 objects labeled as UCDs (label=1) 2299 and with label=0 Choosing an appropriate set of features is an important part of designing a good machine learning classifier. By intuition, spectral indices are a good set of features to use. We added the J-SNR, χ_L^2 , χ_T^2 and the F-test value as additional features. For missing features, we replaced those values with -99999.9 and scaled all features in the range [0, 1] using `MinMaxScaler`. To test the accuracy of our classifier, we used 2-fold cross validation score (CV) and split the training by 50% and 50% partitions (similar to the procedure of Miller et al. 2017) and obtained a CV accuracy score of $\sim 97.6\%$. We then used the classifier on the 110930 point-source objects in both surveys with J-SNR>3, classifying 78 sources as UCDs. The false positive rate (FP) for this method, using the same definition is $\sim 37\%$. The great advantage of using a random forest is its low overall false

positive rate compared to the previous method, making the visual inspection easier. In addition, this method selects . However, one needs a fully characterized training set to use this method.

3.5.1. *Absolute Magnitude Spectral Type Relations*

Given the absence of reliable absolute F110W, F140W and F160W absolute magnitude spectral type relations covering the spectral type range of M5–Y2 in literature, we created an absolute magnitude-spectral type relation to estimate distances of objects in our observed sample, created from J, H relations by [Pecaut & Mamajek \(2013\)](#). We computed an offset/color between J and H magnitudes and AB F110W, F140W, F160W magnitudes and used this offset to obtain new relations. We used a sample of 322 spectra the SpeX Prism library with measured parallaxes and measured the magnitude and a list of Y dwarfs from the Schneider sample [should change this to Y dwarfs with parallaxes] (3.1) and measured their absolute magnitudes by convolving the flux-calibrated spectrum (the spectrum scaled to its absolute magnitude) with the filter profiles shown in 4. The uncertainty in each convolution is computed by random sampling. The offset in convolutions between HST filters and J and H filters is then added to the absolute magnitude-spectral type relations in J, H from [Pecaut & Mamajek \(2013\)](#) to obtain an absolute F110W, F140W, F160W magnitude. We then used an linear interpolation method to compute J, H magnitudes and a 6-degree polynomial fit to obtain the relations for F110W, F140W, and F160W. Error propagation through for these steps is done by standard error propagation formula i.e $\sigma^2(F110W - J) = \sigma^2(J) + \sigma^2(F110W)$ for instance. We report these relations and their intrinsic scatter in Table 1 and show them in Figure 7

3.6. *Sample Characterization*

3.6.1. *M dwarfs & General Sample Statistics*

We found 121 objects with spectral types of M7–M9, these objects are defined by the H₂O absorption features. We show the distance distribution of all the UCDs in the sample in Figure 8, we find M and L dwarfs up to $\sim 3\text{kpc}$ while T dwarfs are limited in the nearby ~ 500 pc. The observed galactic distribution of the UCDs is consistent with the galactic distribution and depths of the pointings in the survey, with a few more sources in the northern fields. Many of the M dwarf detection are

robust i.e the major H₂O absorption feature between 1.3 – 1.45 μ m is distinguishable from noise in the spectrum. For WISP spectra, there are additional G102 data displaying other H₂O and FeH and TiO features present in UCD atmospheres, confirming their spectral type classification. As an additional check, we visually inspected photometric images obtained using the coordinate positions from the photometric catalogs, and reference images of each pointing in respective filters to visually confirm point-sources and eliminate galaxies or other extended objects missed by the point-source cut and our selection methods. Nevertheless, we included some borderline objects in our sample that possible UCDs based on their 1D G141 spectrum but with unidentifiable in the photometric image, given that source might have moved compared to the reference images used to derive positions of objects in the catalogs. That is the case for M7 GOODSN J1237+6210, WISP J1224+6112, WISP J2005-4139, COSMOS J1000+0217 and WISP J1006-2953.

3.6.2. *L & T dwarfs*

Early L0-L5 Dwarfs—We identified 26 early (L0-L5) L dwarfs in both surveys and 16 in WISP. There are four L0s all in WISP: WISP J1618+3340, WISP J0246-0104, WISP J1429+3224 WISP J1007+1004 and WISP J1715+0455. All four L0 are relatively good fit to the L0 spectral standards and have additional G102 data to confirm their spectral classification, in addition to being identifiable in their photometric cutouts. WISP J1715+0455 G102 spectrum is noisier than its G141, nevertheless the fit to the spectral standard is not robust. These objects are located at distances of \sim 800 pc, 1.3 kpc, 1.1 kpc and 1.4 kpc respectively. We found seven objects classified as L1: UDS J0217-0509, WISP J0015-7955, WISP J1408+5657, GOODSS J0332-2742, WISP J1154+1941, WISP J0927+6027 and WISP J1150-2033 all identifiable in their photometric images except for GOODSS J0332-2742 whose F160W image obtained from the catalog position points to a nearby extended objects. Nevertheless, its 1D- G141 shows molecular absorption features present in UCDs with a J-SNR of 5. As a feature of the WISP survey, G102 spectra are nosier than G141 spectra but the fit to the spectral standard remains robust. We estimated spectro-photometric distances of \sim 700 pc, 1.1koc, 1 kpc, 1.2kpc, 900 pc, 200 pc, and 260 pc respectively for these sources. The next subtype is L2 and we identified two objects all in the GOODS Northern field: GOODSN J1236+6211 and GOODSN J1236+6209

are both identifiable by their G141 spectra and as point-sources in their photometric images, despite GOODSN J1236+6211 being in a crowded field. We estimated distances of ~ 900 pc and 2.4 kpc for both respectively. This makes GOODSN J1236+6211 with a J-SNR of 5, the most distant L/T dwarf in the sample. Next, we discovered three L3 dwarfs, all in the WISP fields: WISP J1544+4844, WISP J1154+1939 and WISP J1133+0328. The first two objects are borderline cases given their low J-SNR, but all three L3s show strong H₂O absorption at $\sim 1.4 \mu\text{m}$ confirming their spectral types. We estimated distances of 1kpc, 1.3 kpc and 600 pc respectively. In terms of L4s, we found nine objects: WISP J0125-0001, COSMOS J1000+0219, GOODSS J0333-2751, WISP J1019+2743, WISP J1625+5721, GOODSN J1236+6209, WISP J1004+5258, GOODSN J1236+6214, GOODSS J0332-2749. Their spectral traces are all robust, except for WISP J1004+5258 which shows extra flux at 1.4 μm from possible contamination with nearby objects. GOODSS J0333-2751 is the highest SNR object in this set and it shows a poor fit on both ends of spectrum that we attribute to the contamination in the spectrum. These nine objects are located at distances of ~ 1.1 kpc, 1.2 kpc, 500 pc, 750 pc, 500 pc, 1.9 kpc, 850 pc, 670 pc and 1.2 kpc respectively. Finally, GOODSN J1235+6211 is the lone L5 object in the sample located at $\sim 1\text{kpc}$ with no particular interesting features and a low J-SNR of 6.

L/T transition objects—There are two mid-L objects: WISP J1124+4202 and UDS J0217-0509 are both low-SNR objects but they have robust H₂O features confirming their classification. They are located at ~ 460 pc and 960 pc respectively.

T dwarfs—T dwarfs are characterized by stronger H₂O absorption CH₄ features. In our sample, we identified 13 T dwarfs. WISP J1003+2854 is classified as T0 at ~ 1 kpc. The G141 spectrum displays deep H₂O feature at 1.4 μm , but the spectrum is a poor fit to spectral standards towards the edge of the detector. This object has a magnitude of F160W=23.1 placing it at ~ 600 pc. COSMOS J1000+0217 is also classified as T0 at a distance ~ 900 pc. There are 3 T1 objects in the sample: WISP J1115+5257, WISP J0326-1643 and WISP J1150-2033 at distances of 950 pc, 770 pc and 620 pc respectively. The first two objects have additional G102 spectra that further confirm

their classification while WISP J1150-2033 does not appear in the photometric cutout, making it a borderline detection. For later types, the strength of the CH₄ absorption feature at $\sim 1.61 \mu\text{m}$ is more pronounced. We found 2 T3 dwarfs: GOODSS J0332-2749 and WISP J0437-1106 at respective spectro-photometric distances of ~ 450 and 820 pc respectively. WISP J0437-1106 additional G102 data further confirms its spectral classification. In terms of mid-to late T dwarfs, we found 3 objects previously discovered by Masters et al. (2012). WISP0307-7243 is classified as T4 at ~ 500 pc, WISP J1232-0033 is classified as T7 at ~ 200 pc and WISP1305-2538 is classified as T9 at ~ 300 pc. Our classifications and distances agree with the previous classification. We found another T dwarf in AEGIS-03, AEGIS J1418+5242 is classified as T4, with a high SNR (J-SNR=21) and apparent magnitude of F140W=22.7 implying a distance of ~ 500 pc. The spectrum is a good fit to the spectral standard and there is no visible contamination by nearby objects in the field or other spectral orders. Finally, GOODSS J0332-2741 is latest T dwarf that in the sample that has not been identified by other works. The 1D G141 spectrum of this spectrum fits to the T6 spectral standard, although the water feature at $1.2 \mu\text{m}$ is stronger. There is also excess flux in the continuum at $1.6 \mu\text{m}$ not present in the spectral standard pointing to a possible bad telluric correction in the standard and/or poor estimation of the contamination of this object. Nevertheless, with a magnitudes of F140=22.1 and F160W=22.9, we estimate a spectro-photometric distance 254 ± 51 pc for this object.

3.6.3. Subdwarfs, Y dwarfs & Spectral Binaries

We searched for subdwarfs and Y dwarfs by creating selection criteria for these subtypes. However, we did not find any obvious subdwarfs or binaries in the sample with the two methods. In general, the sample are relatively good fits to spectral standards with no peculiar excess fluxes that could not be attributed to the noise or the contamination in the spectrum. This is unsurprising given that estimates of the ratio of subdwarfs to dwarfs is 1/400 (ref) and the binary fraction of UCDs is very low <10%.

4. PROBING GALACTIC STRUCTURE

4.0.1. Point-Source Limiting Magnitudes

Momcheva et al. 2016 reported the effective depths of all the pointings in 3D-HST, however, given various cuts that we made and a variation in exposure times per pointing, we estimated a limiting magnitude for each individual pointing separately. We fitted a Gaussian kernel density estimator (KDE) to the distribution of magnitudes of point-sources with $J\text{-SNR} > 3$ in each filter, to obtain a probability distribution (PDF) of the magnitudes. The choice of using a KDE is advantageous for pointings with only a few point-sources, while using a simple histogram might be subject to visual biases depending on the width of the bins. The faint-limit is set at the maximum of the computed PDF while we set an automatic bright end at 16 based on the tail end of the overall distribution of magnitudes (Figure 13). These brightness and faintness limits are then used to estimate the effective volume of each pointing based on the absolute magnitude-spectral type relations defined in this work.

4.1. Monte-Carlo Simulation

The observed number of stars in a given observational sample depends on the local luminosity function, the probed effective volume, and selection biases. For UCDs, it is also necessary to take into account brown dwarf evolution. We constructed a Monte-Carlo simulation to fully integrate these effects following methods based Reid et al. (1999) and Burgasser (2004), explained in this section.

4.1.1. Local Luminosity Function

The local UCD luminosity function ($\text{LF} = \frac{dN}{d\log L} = \Phi_L$ in $\text{SpT}^{-1} \text{ pc}^{-3}$) of UCDs have been measured by several groups (Reid 2003; Cruz et al. 2007a; Bochanski et al. 2010; Metchev et al. 2008; Reyle et al. 2010; Kirkpatrick et al. 2019; Bardalez Gagliuffi et al. 2019). Ryan & Reid (2016) approaches this problem using a parametrized LF matched to observations. Because our sample of UCDs probes large distances, we simulated a luminosity function from two fundamental stellar distributions: the mass function and the age distribution.

- **Mass (M):** We draw a sample of 10^5 objects from a power-law mass function parametrized by α for masses between $0.001 M_\odot$ and $0.1 M_\odot$.

$$P(M) = \frac{dN}{dM} \sim \left(\frac{M}{M_\odot} \right)^{-\alpha} \quad (9)$$

. We adopt $\alpha = 0.6$ based on results from Kirkpatrick et al. (2019), consistent with the mass function of UCDs in young clusters. Masses are drawn by inverting the cumulative distribution (CDF) of the mass-function the mass function as $M = CDF^{-1}(x)$ for $x \in [0, 1.]$.

- **Age (τ):** We assigned ages drawn from a uniform uniform age distribution spanning 100 Myr–10 Gyr. Although there are different parametrization of the star-formation history of the Galaxy (REFS), a uniform age distribution reasonably matches the local stellar population.
- **SpT $\leftarrow T_{eff} \leftarrow (\text{Mass}, \text{Age})$** : We determined effective temperatures, L_{bol} , Log g, radii to each of the simulated objects, using a log-linear interpolation of solar-metallicity evolutionary model grids of Baraffe et al. (2003) valid for stellar masses of 0.0005 to $0.1 M_\odot$ and solar-metallicity hybrid models of Saumon & Marley (2008) valid for stellar masses of 0.0002 to $0.85 M_\odot$. We scaled these temperature distributions to the measured LF of Kirkpatrick et al. (2019) of $\Phi = 0.63 \times 10^{-3} \text{pc}^{-3} K^{-1}$ for T_{eff} values between 1650–1800 Kelvin and defined the scaling factor from the distribution of effective temperature $n(T_{eff})$ as $N_0 = 0.00063 \text{pc}^{-3} \sum_{1650K}^{1800K} n(T_{eff})$. We then converted effective temperatures to spectral types (M7-T8) using a linear interpolation of T_{eff} and spectral types from Pecaut & Mamajek (2013) and accounting for the scatter in this relation of $\Delta T_{eff} = 108 \text{ K}$, that is the temperature is chosen from a Gaussian centered around the interpolated value with a width of 108K. A comparison between the prediction of from evolutionary models and the measured LF (Figure 9) shows a general agreement between models and the empirical LF of Kirkpatrick et al. (2019) except for the parameter space where the models are invalid. As an additional check, we compared the luminosity functions of Bardalez Gagliuffi et al. (2019); Cruz et al. (2007a) to the predictions from models using a conversion between spectral type and absolute J magnitude of Dupuy & Liu (2012) by normalizing the distribution of magnitude to $\Phi(J \in [11.75, 12.25]) = 0.0015 \text{mag}^{-1} \text{pc}^{-3}$. Both sets of models show an agreement with the measurements of Bardalez Gagliuffi et al. (2019) within the domain of validity of the absolute-magnitude relations. Note that these models assume solar metallicity field predictions. As discussed further below, ratio of the

number of field objects to metal-poor halo and thick disk objects is too small to be detected in sample of L & T dwarfs ~ 40 .

4.1.2. Effective Volumes

The observed effective volume of each pointing depends on the scale height and the limiting magnitude of the survey. We compute these volumes using the following steps:

- Having obtained the limiting magnitude of each pointing, we computed distance limits for a given spectral type and pointing d_{lim} determined by

$$\log d_{\text{lim}} = \frac{1}{5}(m_{\text{lim}} - M(\text{SpT})) + 1 \quad (10)$$

where m in the faint or the bright limit of the survey and $M(\text{SpT})$ is the absolute magnitude for that spectral type. We estimate the limiting distance in each available filters and obtain an effective limiting distances by average estimates in all filters using our absolute magnitude calculations described in Section 3.5.1. An accurate treatment of the limiting depth would account for the effect of dust extinction; however, 3D-HST and WISPS pointings are located at high enough galactic latitudes to avoid this issue in this study.

- We assume a simple single-component axisymmetric exponential disk model parametrized by $\theta = (H, L)$ where H and L are the vertical scale height and radial scale length of the stellar number density given by

$$\rho(\vec{r}) = \rho(R, z) = \rho_{\odot} \cdot \exp\left(\frac{-|z - Z_{\odot}|}{H}\right) \cdot \exp\left(-\frac{R - R_{\odot}}{L}\right) \quad (11)$$

where R, z are cylindrical coordinates centered around the Galactic center, L is assumed at 2600 pc while H was allowed to vary from values of 200 pc, 250 pc, 275 pc, 300 pc, 325 pc, 350 pc and 1000 pc. R_{\odot} and Z_{\odot} are the sun's position from the galactic center, fixed at 8300 pc and 27 pc respectively. The vector \vec{r} is the galacto-centric position vector and can be related to the star's distance from the Sun as

$$\vec{r} = \left(R_{\odot} - d \cos(\beta) \cos(l), -d \cos(\beta) \sin(l), Z_{\odot} + d \sin(\beta) \right) \quad (12)$$

where (β, l) are Sun-centric galactic coordinates for that star.

- \mathbf{V}_{eff} : given the Galactic structure model, we compute the effective volume of a pointing along a line of sight (R, z) as

$$V_{eff} = \Delta\Omega \int_{d_{min}}^{d_{max}} d|\vec{r}| \cdot \frac{\rho(\vec{r})}{\rho_\odot} \cdot |\vec{r}|^2 \quad (13)$$

. Where the $\Delta\Omega$ is the solid angle of each pointing in this study fixed at the field of view of the WFC3 with $\Delta\Omega 3.47 \times 10^{-7}$ radian², $|\vec{r}|^2 = R^2 + z^2$ is the distance along that line of sight, and (d_{min}, d_{max}) are the limiting depths d_{lim} . This is an one-dimensional integral along a line of sight (β, l).

4.1.3. Selection Effects

Because we applied several selection criteria to narrow down our sample for visual confirmation, it is possible we may have missed a few UCDs in the WISPS/3D-HST fields; particularly low SNR or peculiar objects due, in part, to uncertainties in spectral indices. Hence, the observed volumes objects must corrected by a factor proportional to our selection biases. To fully quantify these effects, we generated a distribution of low-resolution spectra uniformly sampling our SNR distribution across a wide range of SNRs and measured their recovery rate through this selection process by augmenting the SpeX sample to cover 3 orders of magnitude in SNR. To create this sample, we picked the top 20 highest SNR spectra with a median SNR between 50 and 200 M7-T9 objects in the SpeX sample obtaining a total of 298 spectra. We also added the WFC3 spectra of the Schneider set to the sample. We then degraded each spectrum by Gaussian iteration of 10^2 creating a new sample of 21800 spectra accross signal-to-noise. Each new "degraded" spectrum is created as

$$\{F(\lambda_i)\} \sim \text{Normal}(< F(\lambda_i) >, \sigma^t(\lambda_i)) \quad (14)$$

. $\sigma^t(\lambda_i)$ is the target noise at a wavelength λ_i , and $< F(\lambda_i) >$ is the flux of the original spectrum at that wavelength. We computed all relevant statistics for each of the degraded spectra, including J-SNR, spectral indices, F-test, and the two χ^2 s. We applied our selection processes to this sample of simulated spectra by measuring spectral indices and applying first F-test criterion where F-test < 0.4 , box index-index selection criteria and the random forest classifier.

With a perfect selection function, we would recover the entire ideal sample of spectra across signal-noise ratio, however, we expect to lose some of the lowest J-SNR objects. Hence, we defined our selection probability in a given sigma-to-noise range (Δ J-SNR bin of 2.0 as $\mathcal{S}(\text{J-SNR}, \text{SpT})$)

$$\mathcal{S}(\text{J-SNR}_i, \text{SpT}) = \frac{N_{s,i}}{N_{tot,i}} \quad (15)$$

where N_s is the number selected spectral type and SNR bin, and N_{tot} is the total number of objects in that bin. Where $N_{s,i}$ is the number of objects in a bin (i) and $N_{tot,i}$ is the total number of spectra in that signal-to-noise ration bin. For instance, if we simulated 100 M7 objects for $\text{J-SNR} \in [10, 12]$ and recovered 70 objects classified as M7, then $\mathcal{S}(\text{J-SNR} \in [10, 12], \text{M7}) = 0.7$. These selection probabilities for each selection method are showcased in Figure 12. As expected the highest signal-to-noise objects are selected across all spectral types, but lose a few of them for low-SNR as indices become more uncertain. However, our selection methods turn out to be generous selecting objects down to our SNR cut.

- **Distance (d):** To apply this selection process to our Monte-Carlo simulation, we assign a distance to each of drawn from the Galactic structure model. The likelihood of distance (d) is

$$P(d) \sim \rho(d, \beta, l) \cdot d^2 \quad (16)$$

, where β and l are the direction a random pointing in 3D-HST or WISPS. We do not account for the directionality in this likelihood, they are drawn uniformly from the distribution of pointings in 3D-HST and WISPS for simplicity. For a given spectral type we assign a distance is limited to $d_{\min}/2 < d < 5 \times d_{\max}$ to account for objects scattered in the observed volume. Samples for this part of the simulation were generated using Pymc for a number of samples $N=10^4$, sampling each scale height independently using a standard Metropolis-Hastings Algorithm. To make this step and the next steps pointing-independent, given that the limiting magnitudes are a function of pointing, we averaged the limiting magnitude and the limiting distances for within each subtype.

- **Signal-to-noise ratio (J-SNR) :** With this distance distribution, and parameters of the surveys, we can estimate an observable signal-to-noise ratio in the J-band (J-SNR) as observed by

the WFC3 instrument based on the observed UCD sample. We fit a second-degree polynomial to the observed magnitudes (F110W, F140W, F160W) and SNR-J of our observed sample and use our derived absolute-magnitude spectral type relations to estimate the apparent magnitude of each object in our simulated sample based on its randomly-assigned distance and spectral type. The apparent magnitude- J-SNR relation is then used to estimate a signal-to-noise ratio as observed with the WFC3 instrument. We chose to use the apparent F140W magnitude to estimate the J-SNR for simplicity.

- **Selection Probability (\mathcal{S}) :** Given a J-SNR and SpT, we can now assign a selection probability \mathcal{S} to each object.
- We compute the expected number of expected objects per spectral type by a simple product of selection probabilities, effective volume scaled by the normalization factor

$$N_{sim}(\text{SpT}) = N_0 \cdot V_{eff}(\text{SpT}) \cdot \sum_i \mathcal{S}(\text{J-SNR}_i, \text{SpT}) \quad (17)$$

. We compared these numbers to the observed numbers of UCDs for each age distribution in figure 14

4.2. Results

The resulting T_{eff} distribution (Figure 9) from interpolating mass and ages onto both evolutionary models grids is consistent with expectations given atmospheric cooling effects (Burgasser 2004). As UCDs age, they quickly pile up on at the lower end of the spectral type distribution and cooler temperatures, though Saumon & Marley (2008) models incorporate clouds and predict a bump at $T_{eff} \sim 1200$ K. Figure 14 shows the effect of scale height on the probed effective volume. The predicted number density (Figure 14) matches scale height assumptions of $\sim 200\text{-}300$ pc for late M and early L dwarfs and $\sim 200\text{-}400$ pc for early T dwarfs, which are not inconsistent with compiled literature values. For L/T transition objects, we predict a slightly lower scale height and a slightly larger scale height for early T dwarfs compared to other typical members of their respective spectral classes. This mismatch between observations and predictions is perhaps due to a failure to truly resolve

the nature of L/T transition phase using our interpolation methods. Moreover, the L/T transition region is sensitive to unresolved binaries (Bardalez Gagliuffi et al. 2014) and Burgasser (2007) shows this effects causes an increase in the number of density of T0-T5 up to 10–15%. Metallicity effects affect the number of subdwarfs we expected in this sample. UCDs in the thick disk and the halo have similar kinematic ages with stellar populations in these parts of the Galaxy; and UCDs at different metallicities follow different evolutionary tracks. L subdwarfs in the local neighborhood are therefore rare, and this study does not significantly probe large volumes in the thick disk and halo. Lodieu et al. (2017) found $0.04 \times \text{deg}^{-2}$ L subdwarfs in the UKIDSS/SDSS fields; in fact, we expect the number of subdwarfs to be ~ 400 times lower than the expected number of dwarfs in the sample. Nevertheless, the scale height of L5-T0 and late T dwarfs remains unconstrained by this sample given their small number.

5. SUMMARY

The WISPS & 3D-HST surveys provide NIR G141 (1.1-1.14 μm) spectroscopic data and broadband F140W, F110W & F160W photometry for thousands of galaxies and point-sources observed in parallel mode with other on-going HST surveys. We made a point-source cut using in the surveys and obtained 271915 point-sources. Using NIR spectral indices that sample the prominent H₂O and CH₄ absorption features in UCD atmospheres, we created selection criteria based on a calibration sample of templates. We have presented two methods for selecting UCDs in deep HST surveys potentially applicable future infrared parallel surveys. Both methods rely on spectral indices defined to trace H₂O and CH₄ features prominent in the NIR band of UCDS. The box selection method is efficient (completeness $>90\%$) but with relatively high contamination rates that could be significantly reduced by eliminating the lowest SNR sources. This method is not effective for selecting very low SNR sources due to large scatter in indices and early M-dwarfs as the absorption features in these wavelength ranges are shallow. However, these spectral indices are designed to selected T-dwarfs with high accuracy (completeness $>90\%$, contamination $<1\%$). The overall contamination/false positive rate for this method for spectral types of L0–L5 is $\sim 87\%$. A second method uses a random forest classifier to distinguish UCDs from other extragalactic contaminants or artifacts with an accuracy

score of 99.5% in cross-validation. The false positive rate of this method for spectral types of L0–L5 is $\sim 62\%$. Both methods rely on a training set of known UCD samples and can be combined. With these two methods, we have used these data to obtain 166 spectra of M7-T9 UCDs up to distances ~ 4 kpc.

We estimated the expected number of UCDs given a galactic structure model with scale height (h) as a free-parameter. Using a point-source limiting magnitude, we measured the effective volumes of the survey for various values of the scale height. To address intrinsic biases in our selection method, we use a Monte-Carlo simulation to reproduce a distribution of spectral type based on a set of fundamental distribution: mass function, age distribution and conversion/polynomial relation from UCD evolutionary models and our sample. We use the galactic structure model to draw a distribution of distances. With these distributions, we create a selection probability function based on sample of "degraded" templates. The final steps involve summing over selection probabilities. The predicted number of UCDs is consistent with a scale height of $325 \text{ pc} \leq h \leq 350 \text{ pc}$.

Future space missions such as JSWT, Euclid will be contaminated by UCDs. [Ryan & Reid \(2016\)](#) predicted that the number density of UCDs (M8–T8) in JSWT fields peaks around $J \sim 24$ mag with a total surface density of $\Sigma \sim 0.3 \text{ arcmin}^{-2}$. With the *Large-Scale Synoptic Telescope* (LSST), and the *Wide-Field Infrared Survey Telescope* (WFIRST), we expect an increase in both sample size and spectral type accuracy, expanding the parameter space necessary to put significant constraint on the star formation history of the Milky Way in general and the mass function of UCDs in particular ([LSST Science Collaboration et al. 2009](#), [Spergel et al. 2015](#)).

ACKNOWLEDGMENTS

This work is based on observations taken by the 3D-HST treasury program (GO 12177 and 12328) with the NASA/ESA HST, which is operated by the Association of universities for Research in Astronomy, Inc. under NASA contract NAS5-26555.

CA thanks the LSSTC Data Science Fellowship Program, which is funded by LSSTC, NSF Cyber-training Grant #1829740, the Brinson Foundation, and the Moore Foundation; his participation in the program has benefited this work.

Software: Astropy([Collaboration et al. 2013](#)), Matplotlib ([Hunter 2007](#)), SPLAT([Burgasser 2014b](#)), Scipy([Virtanen et al. 2019](#)), Pandas, Seaborn ([Waskom et al. 2014](#)), Daft, Pymc3([Salvatier et al. 2016](#))

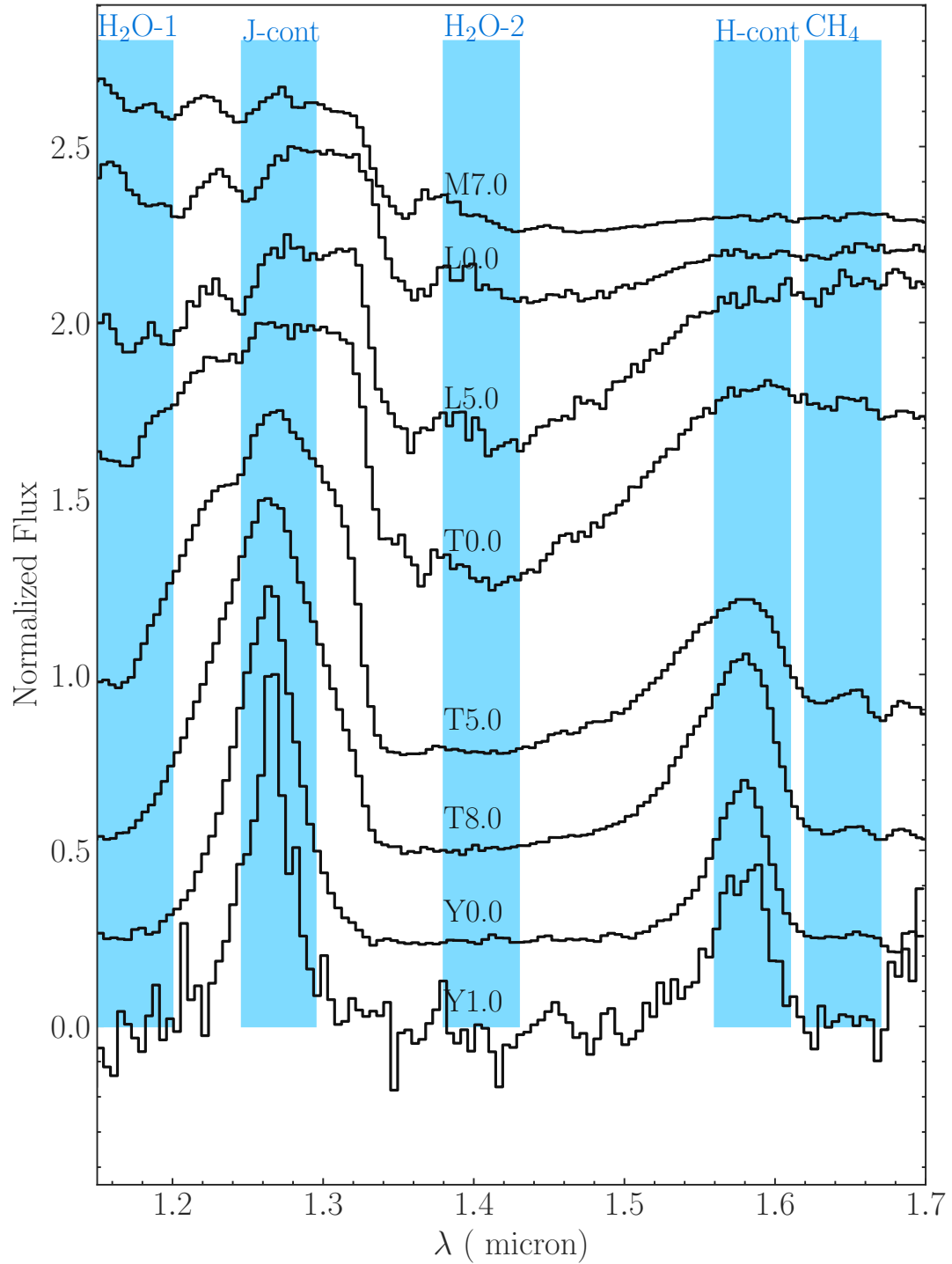


Figure 1. Demonstration of spectral bands used to defined spectral indices in this study plotted against low-resolution SpeX spectral standards (Kirkpatrick et al. 2010)

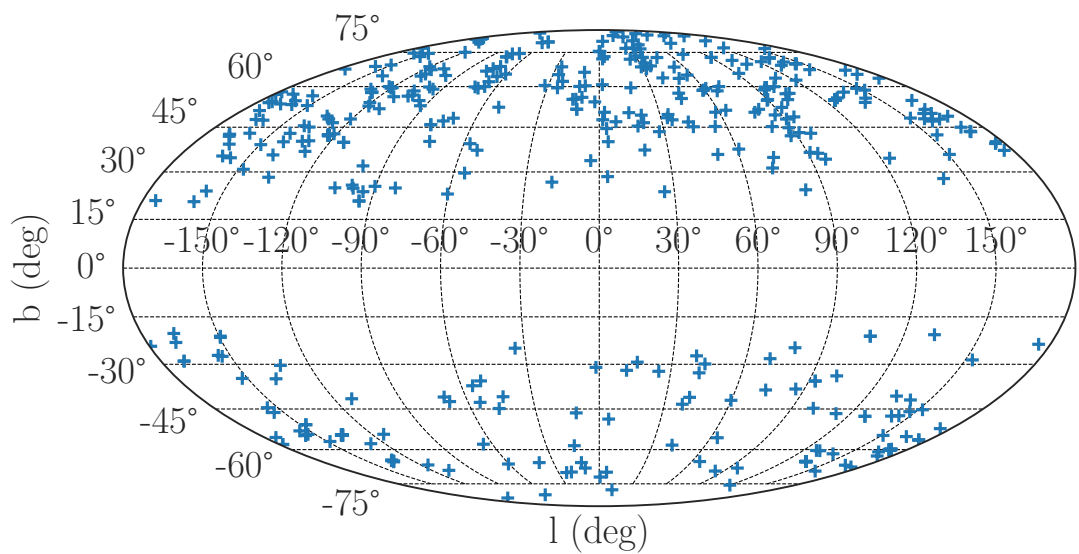


Figure 2. Galactic distribution of pointings in WISPS and 3D-HST

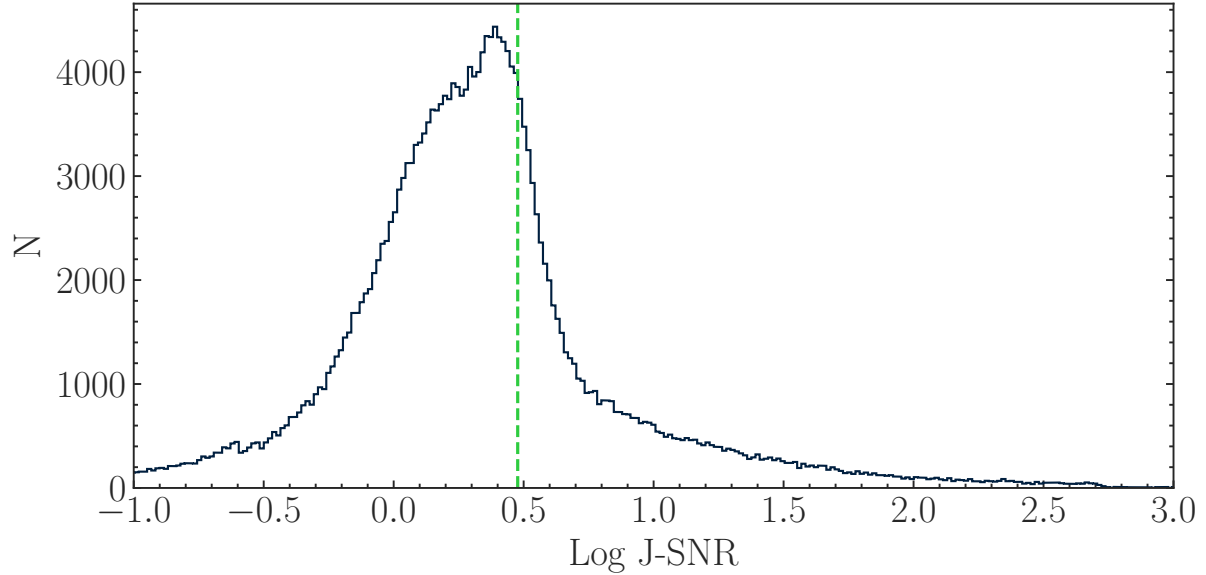


Figure 3. J-SNR distributions of all Spectra in both surveys showing the cut at J-SNR=3

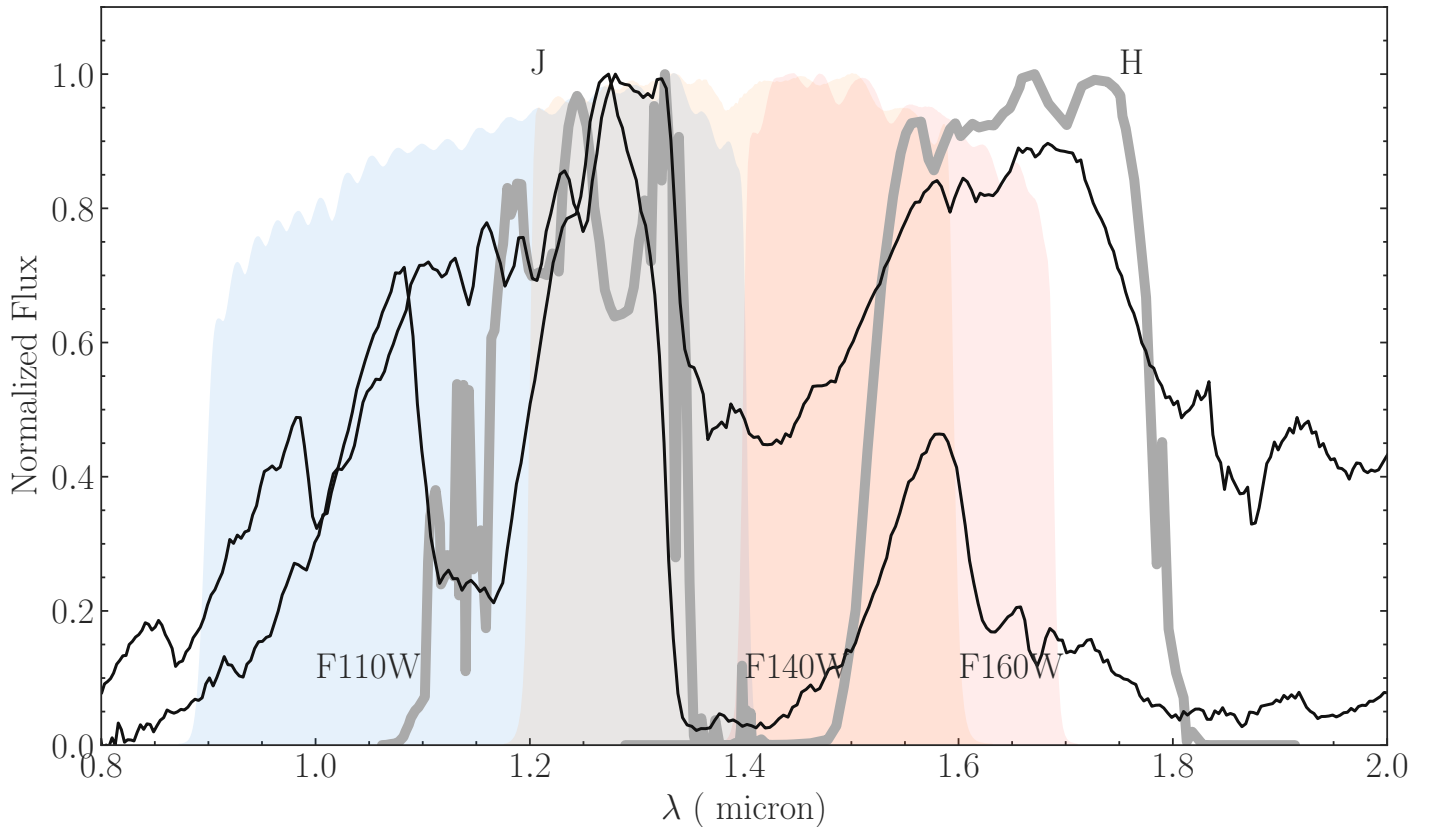


Figure 4. Comparison between spectral coverage of different WFC3 and 2MASS filters used in this study plotted against a typical M7 and T5 dwarf

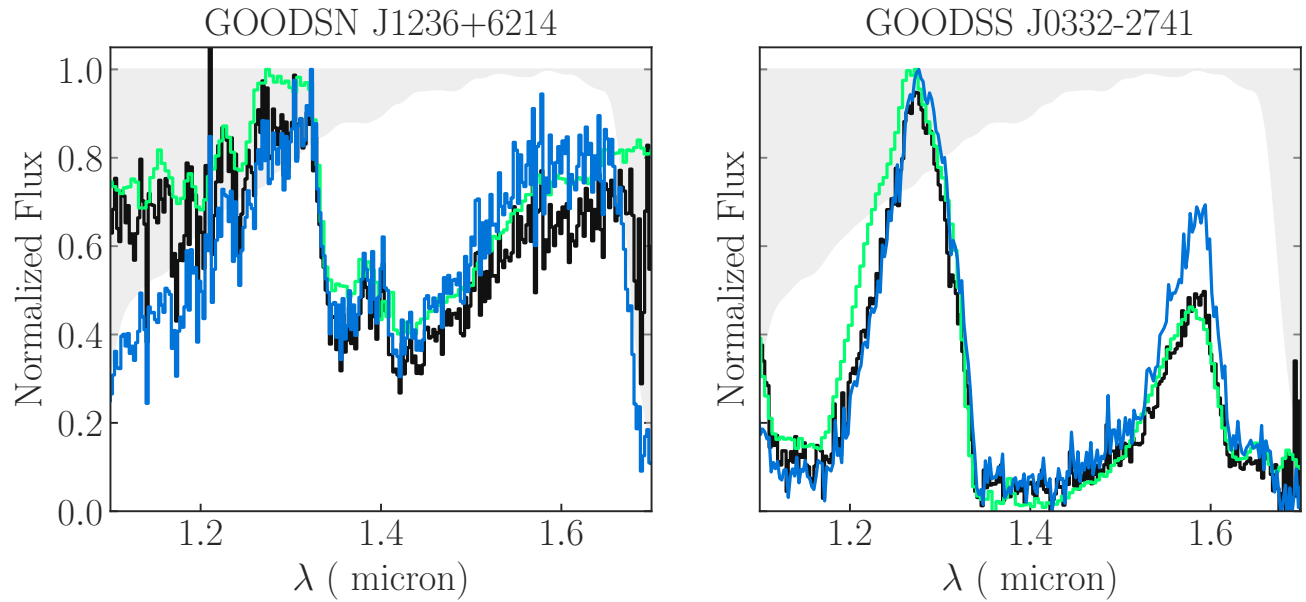


Figure 5. Example of two 3D-HST Spectra before and after continuum correction. The spectrum in green is the spectral standard showing a better fit to a continuum-corrected 3D-HST spectrum (black) and a poor fit to the original spectrum (blue). The spectrum sensitivity is shown in grey

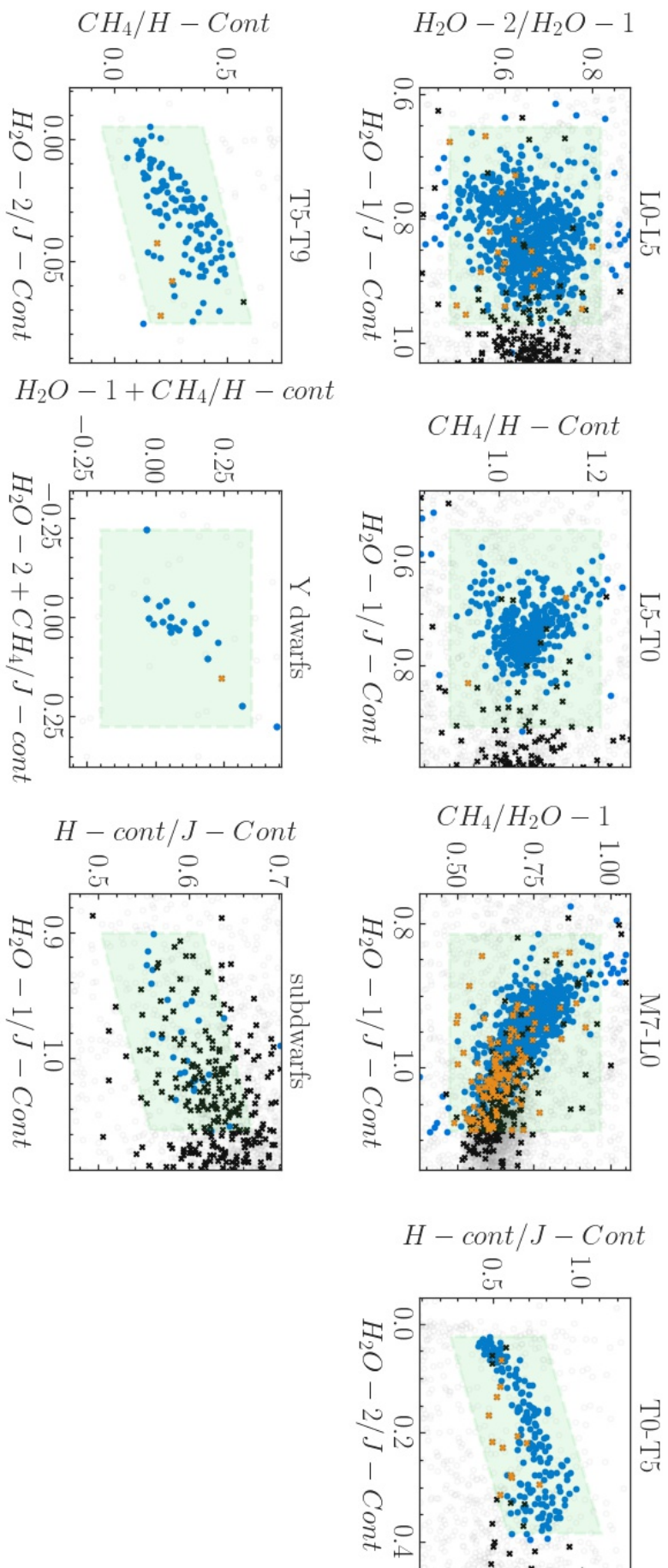


Figure 6. Best selection criteria for different subtype ranges. The grey points are the contaminants after we applied both a J-SNR cut and and F-test cut, the blue points are the set of templates (from the calibration samples) used to define these boxes. The crossed black points are the real UCDs confirmed after visual inspection and the orange crosses are the UCDs that have spectral types for each particular box (e.g a L2 UCD would be colored orange in the L0-L5 while an L7 would be colored black the L0-L5 box)

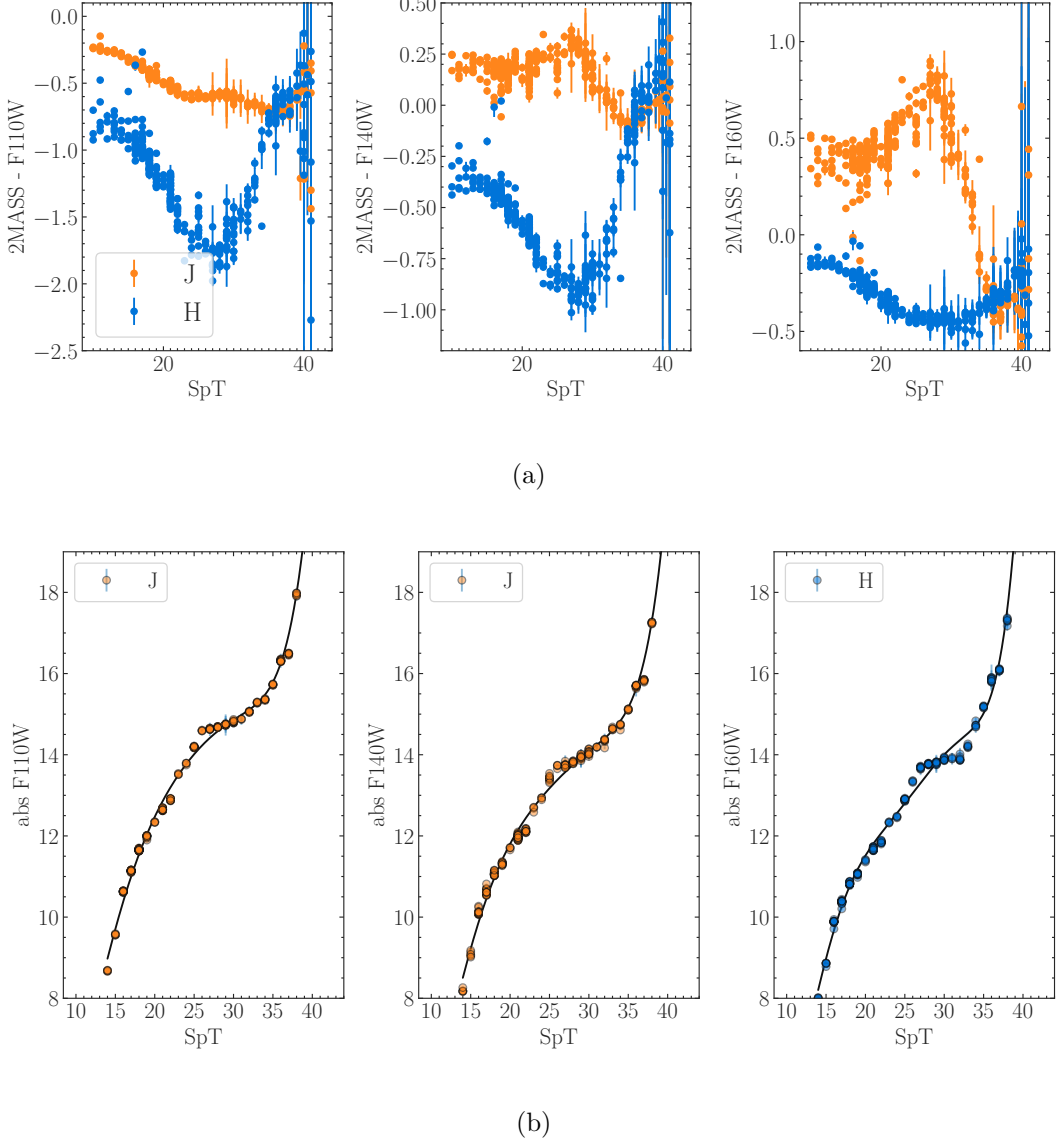


Figure 7. (a) Offsets between 2MASS J, H magnitudes and HST F110W, F140W, F160W magnitudes as a function of spectral type (b) Absolute magnitude-spectral type relations for HST and 2 MASS filters. Orange points show derived relations using the J filter while blue points show derived relations using the H filter. We used the J filter, given its little deviation as function of spectral type for the relations in F110W and F140W and the H filter for the F60W relations for the same reason. The solid line shows a best-fit 6th-order polynomial. We report the coefficients of these polynomials in Table 1

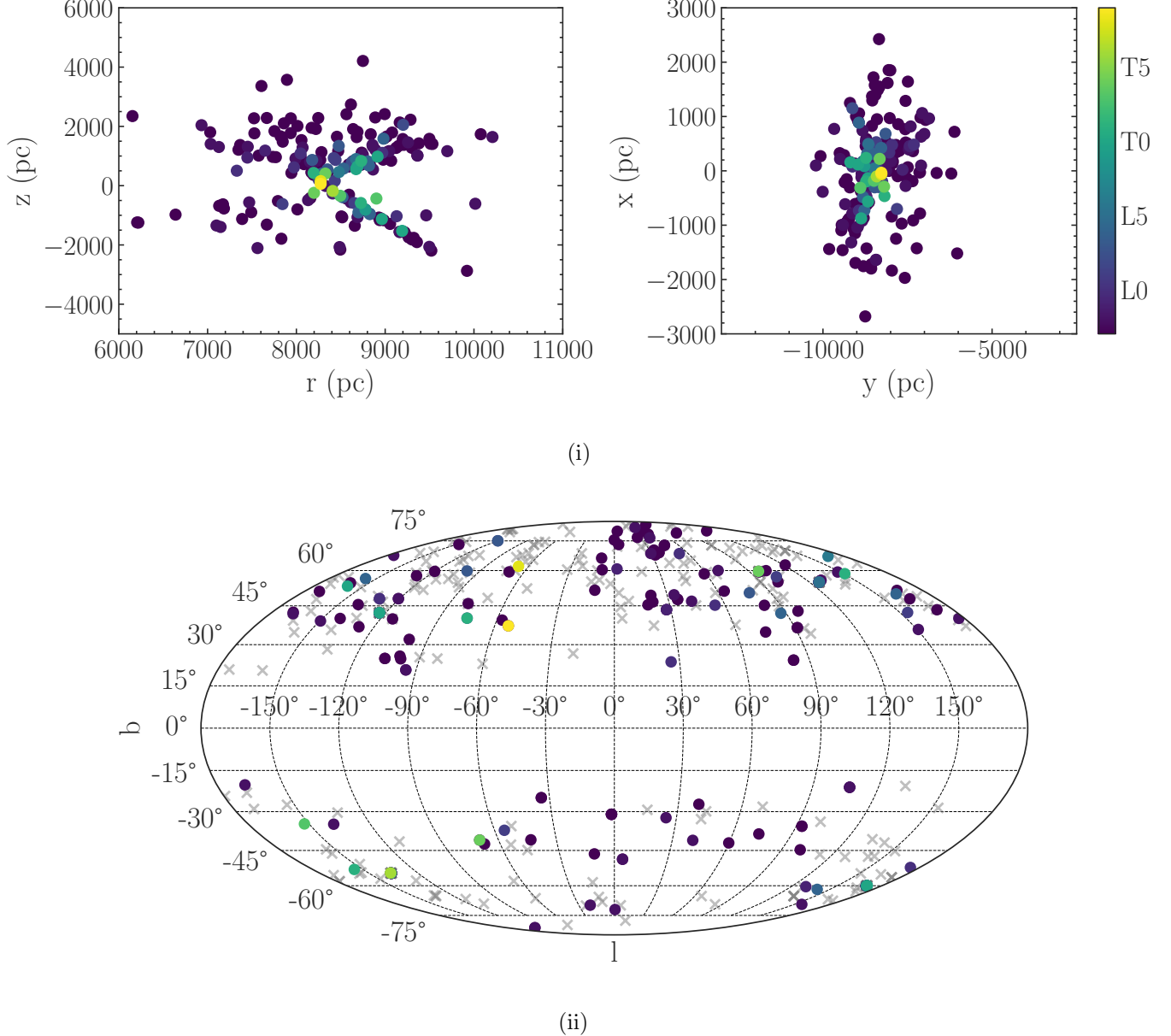


Figure 8. (i) Distance distribution of the UCD sample (ii) Galactic distribution of the sample. Grey symbols show pointings without any UCDs.

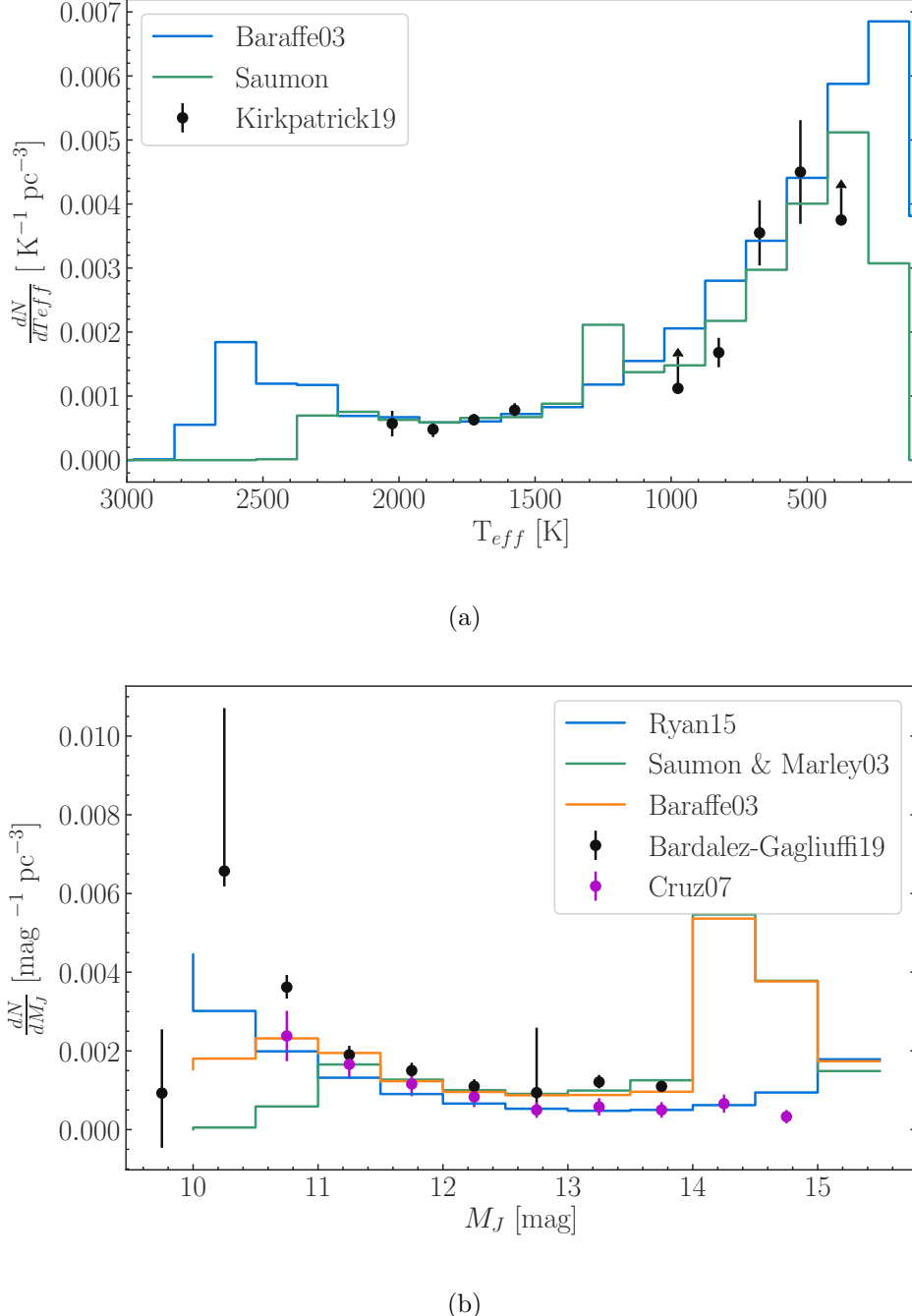
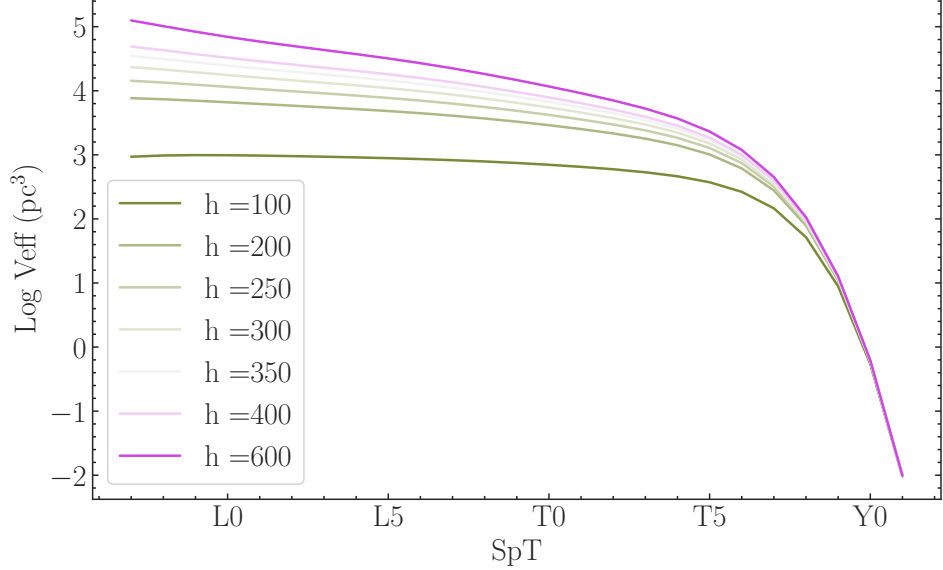
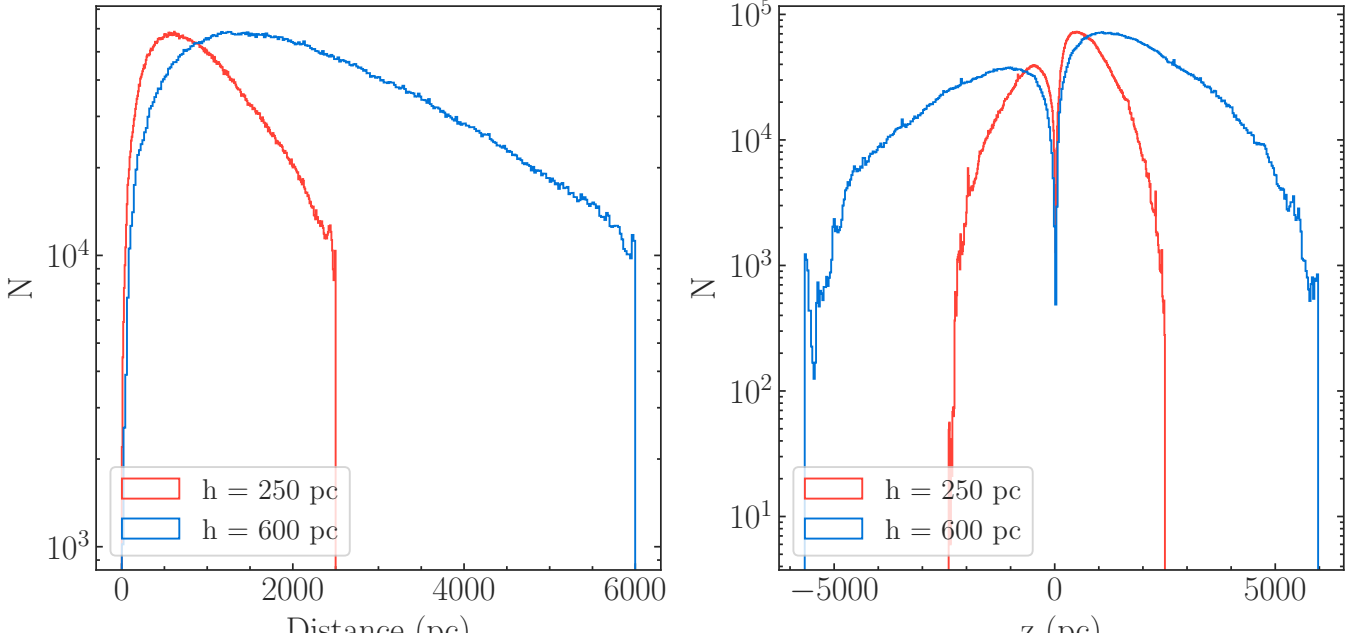


Figure 9. (a) Comparison between our simulated distribution of T_{eff} using evolutionary models of Saumon & Marley (2008) and Baraffe et al. (2003) scaled to the measured luminosity of Kirkpatrick et al. (2019) (b) Comparison between simulated distributions of Jmags using SpT-mag relations of Dupuy & Liu (2012) and measured LFs of Bardalez Gagliuffi et al. (2019); Cruz et al. (2007a) and the polynomial fit of Ryan & Reid (2016)



(a)



(b)

Figure 10. Comparing the effects of scale height: (a) Dependence of computed effective volumes for each spectral type with a volumes = $\Delta\Omega \times \text{dlim}^3$. (b) comparison between distributions of distances drawn from all the pointings in this survey assuming two different scale heights (h) up to a distance of $10h$

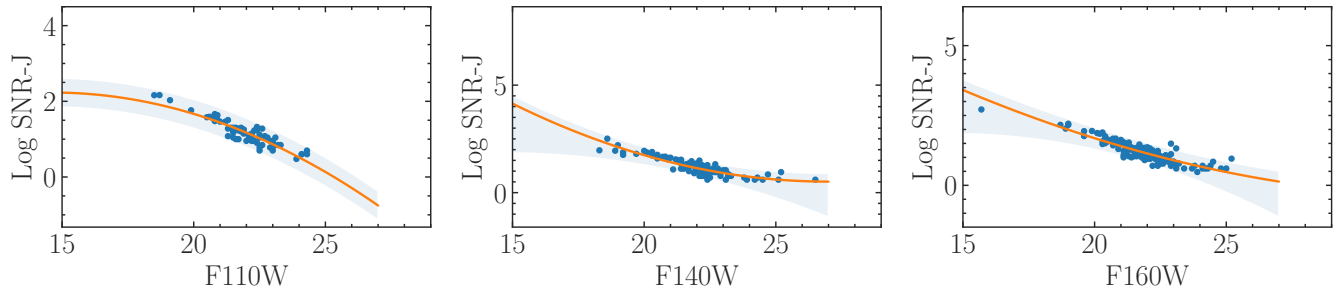


Figure 11. Linear fits between SNR-J and apparent F110W, F140W, F160W magnitudes using the sample of UCDs. These relations are reported in table 1 and used to estimate SNR-J for different apparent magnitudes

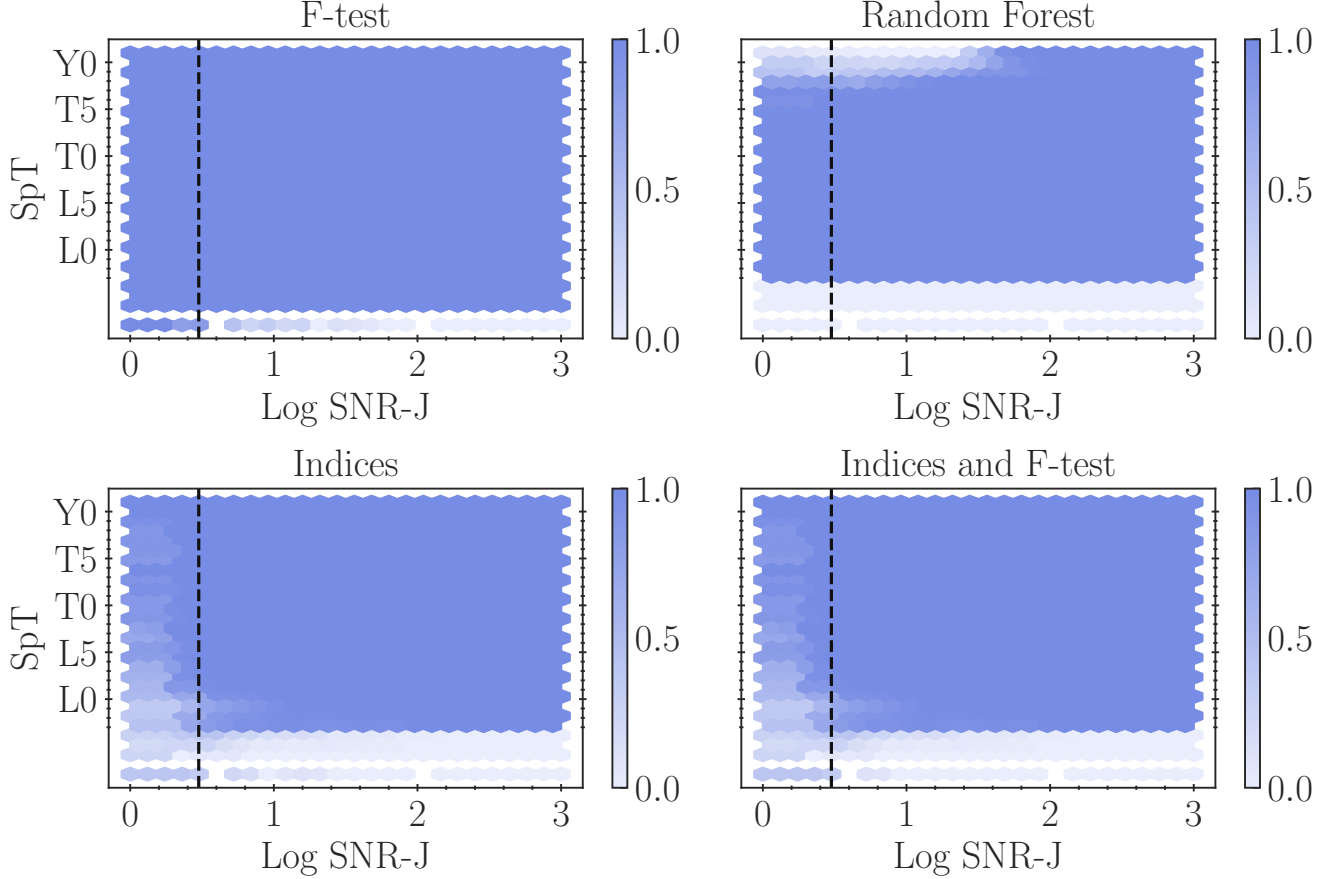


Figure 12. Visualization of our selection function as a function across spectral type and SNR-J. The label "F-test" indicates spectra with $F\text{-test} < 0.4$, the label "RF" indicates the spectra labeled as UCDs by the random forest classifier, and the label "Indices" indicates the spectra selected by our best selection criteria. The bar indicates the selection probability defined as the number of spectra selected over the total number of spectra in each SNR-J, spectral type bin. In the Monte-Carlo simulation, we use the most-selective selection function.

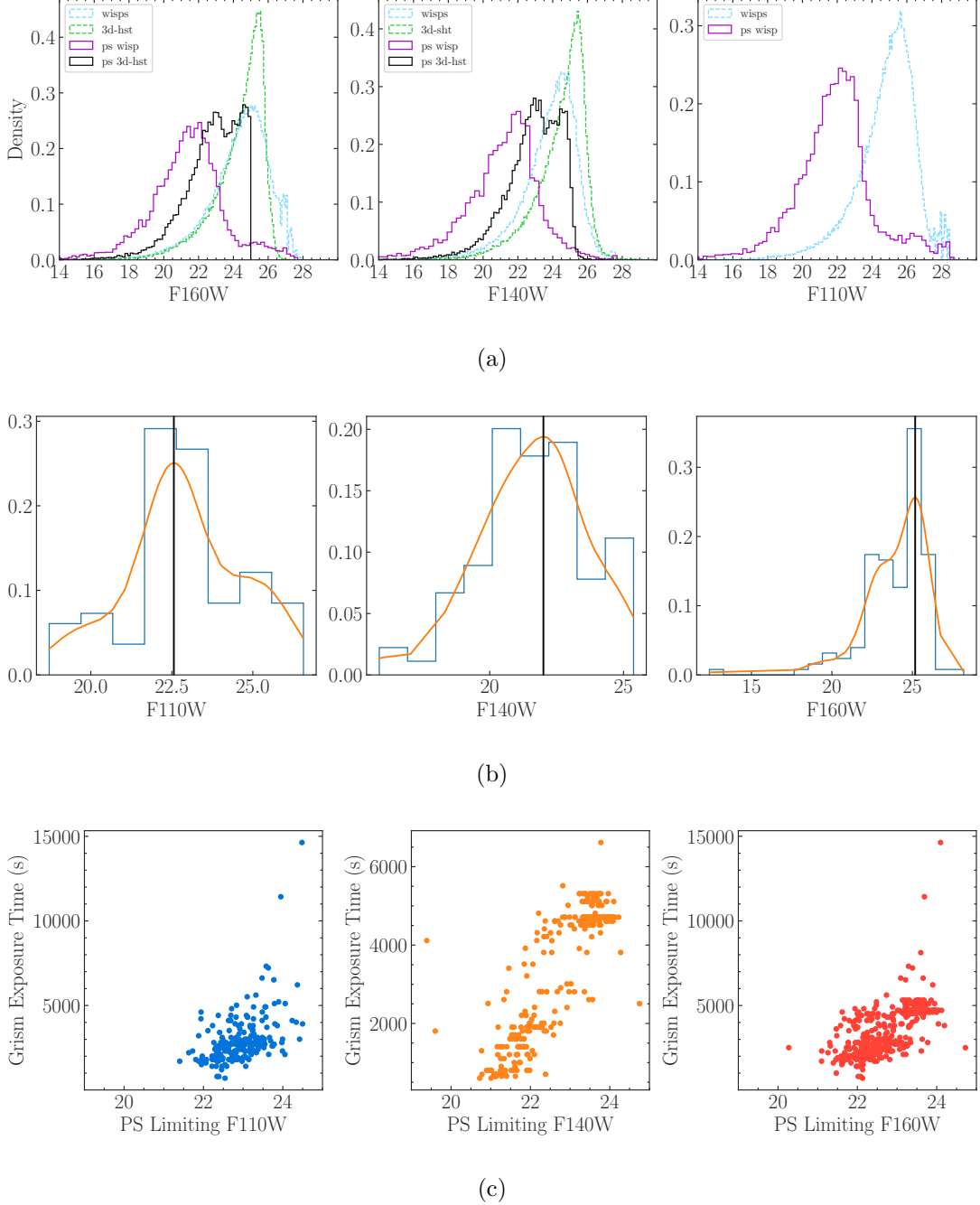


Figure 13. (a) Distribution of magnitudes for sources in both surveys, dotted lines show point sources. (b) Illustration of the estimation of the limiting magnitude of for a select set of pointings. The orange line shows the KDE, while the black line shows the adopted faint limit based on the maximum of the PDF (c) Distribution of faint limits for all the pointings in this work plotted against the integration time in G141 for that pointing

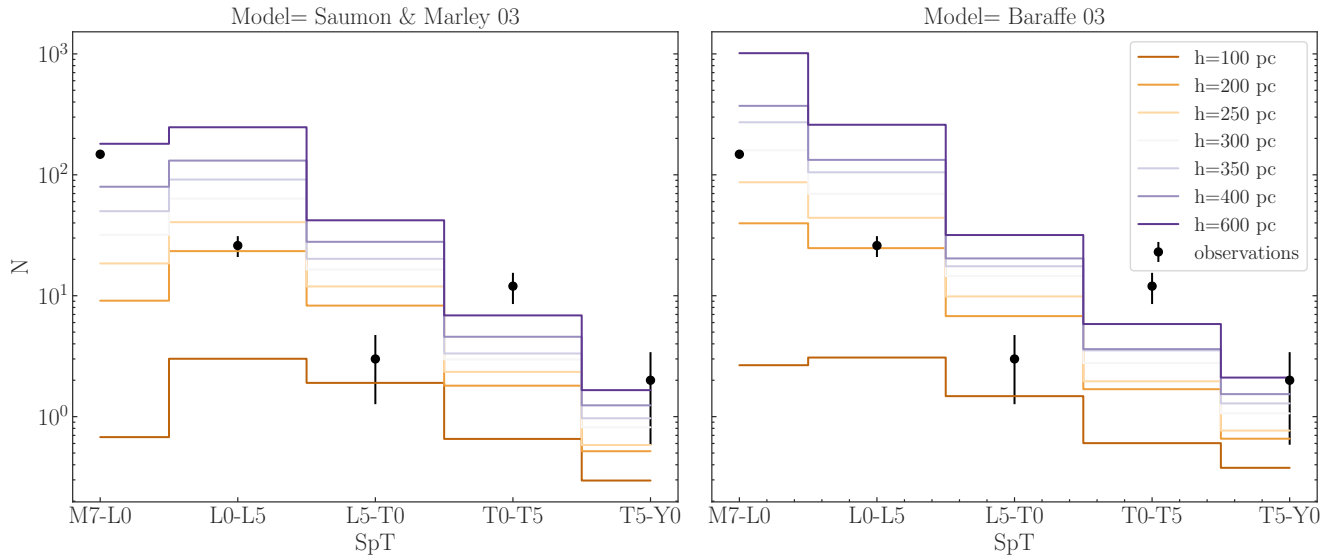


Figure 14. Comparison between the measured number densities and the expected number densities based on the Monte-Carlo simulation based on different age distributions and models

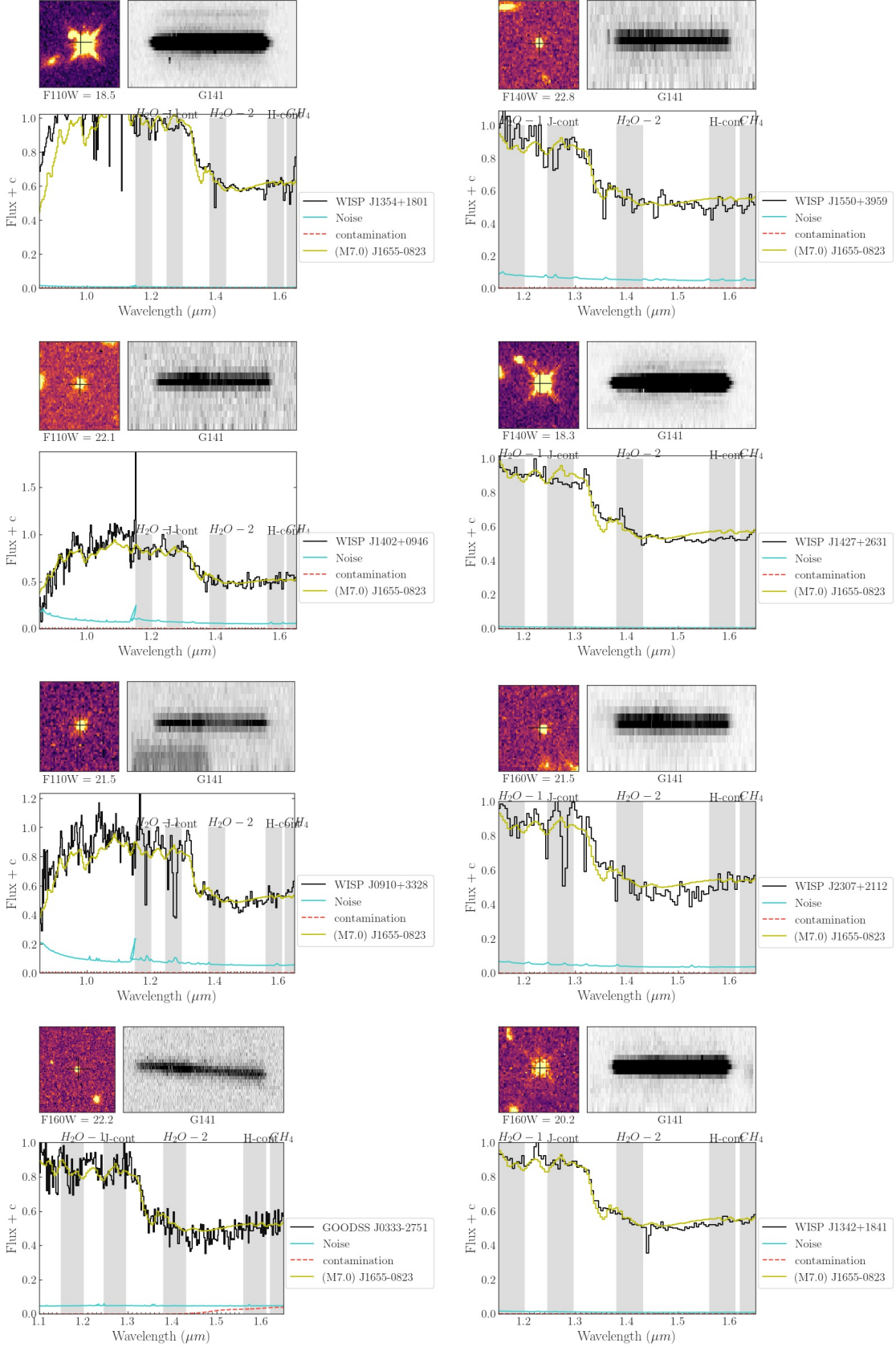


Figure 15. Spectra of UCDs in both surveys. The bottom plot shows the 1D spectrum fit to a spectral standard. The noise and the contamination are also shown, the top left plot shows the WFC3 image acquired in either F140W, F160W or F110W filter and the top-right plot shows the cutoff of the G141 spectrum for that extracted object.

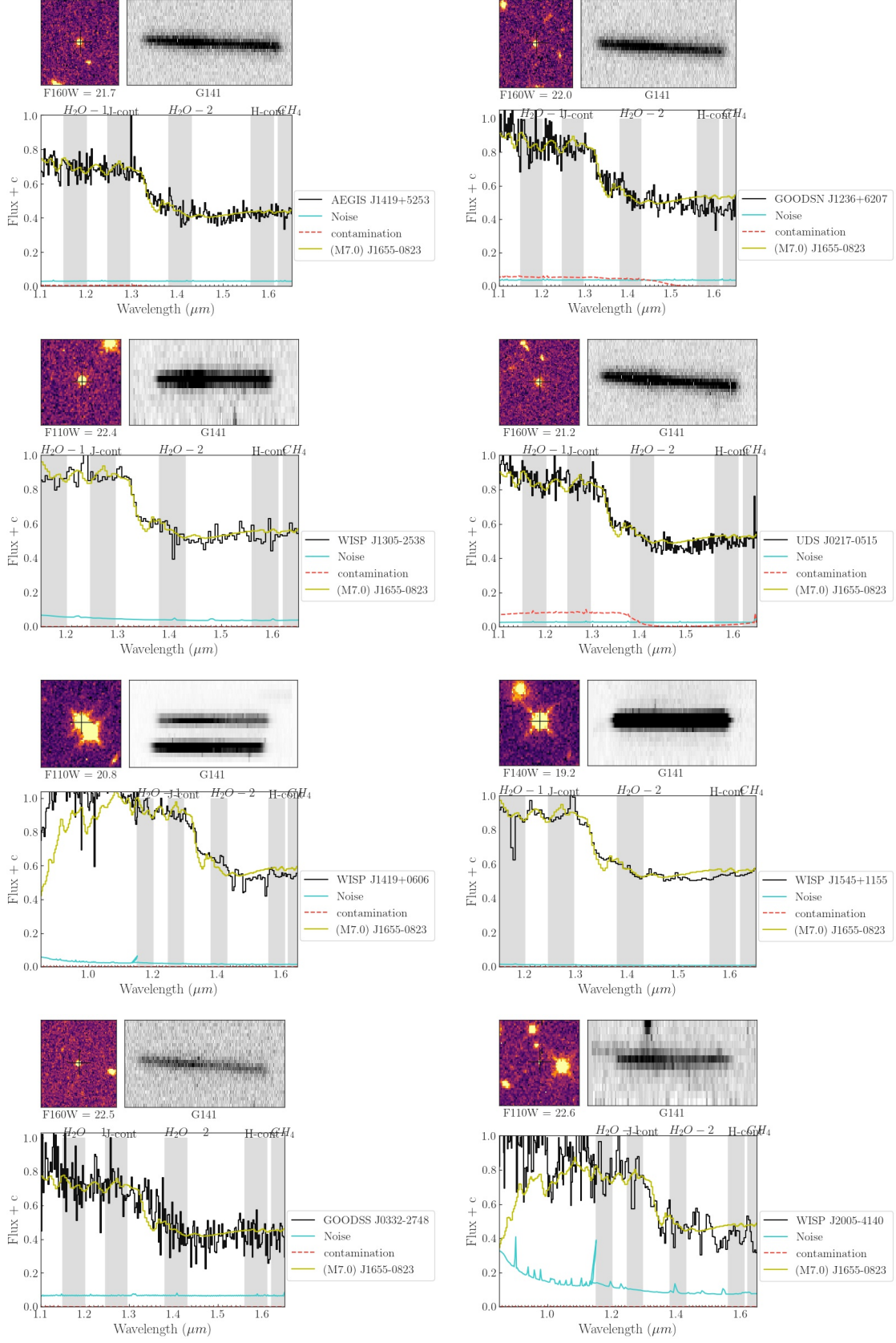


Figure 16. cont.

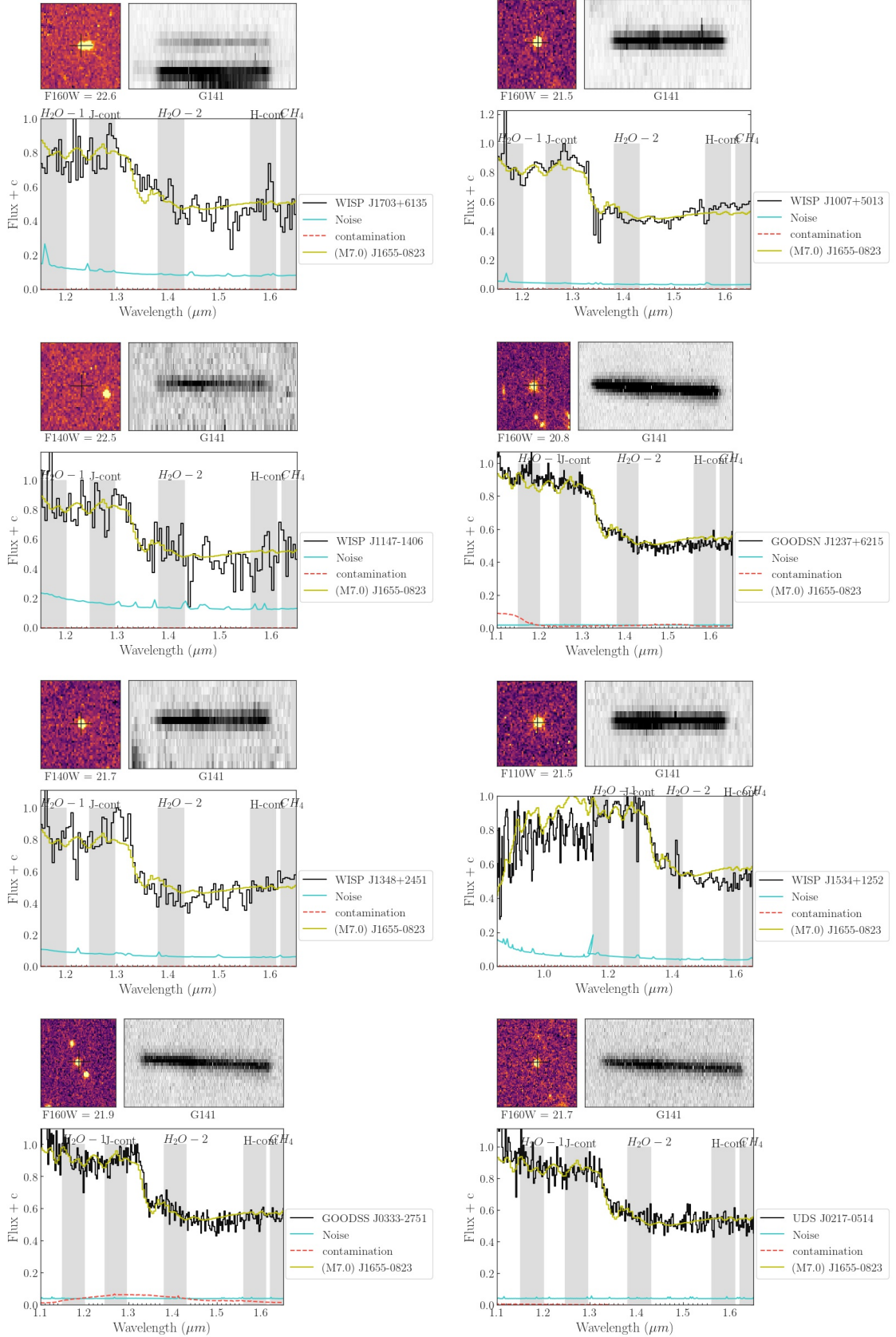
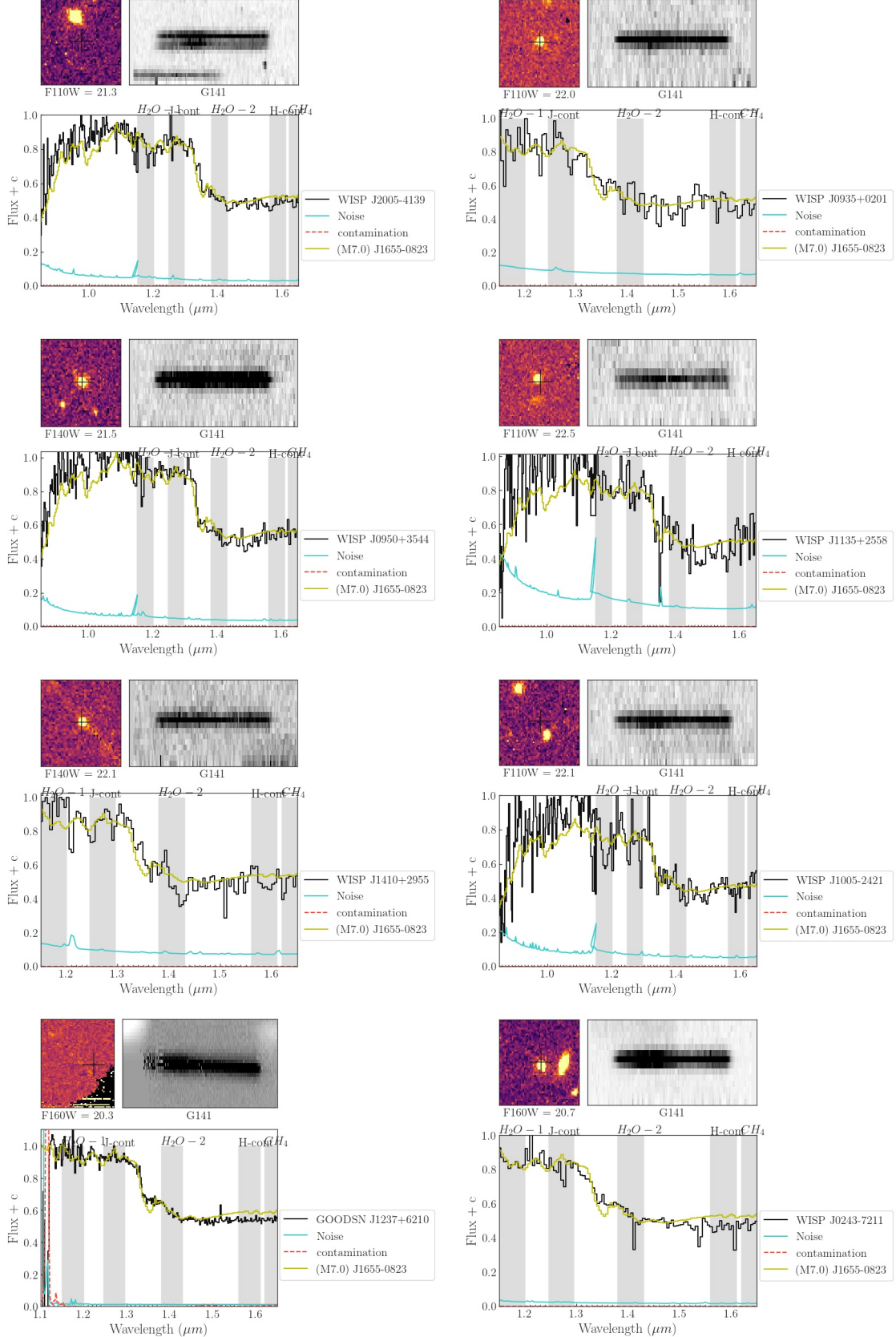
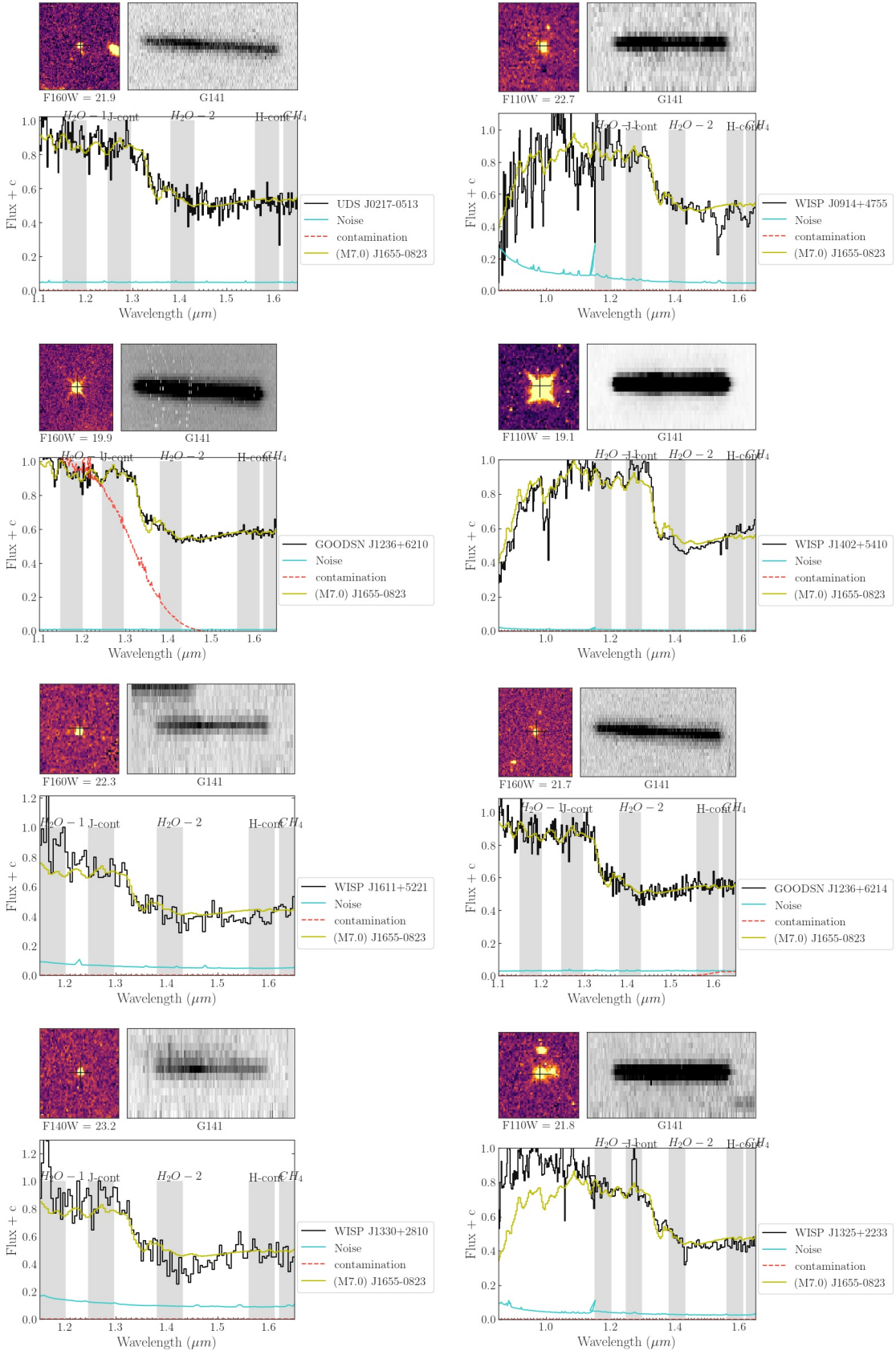


Figure 17. cont.

**Figure 18. cont.**

**Figure 19.** cont.

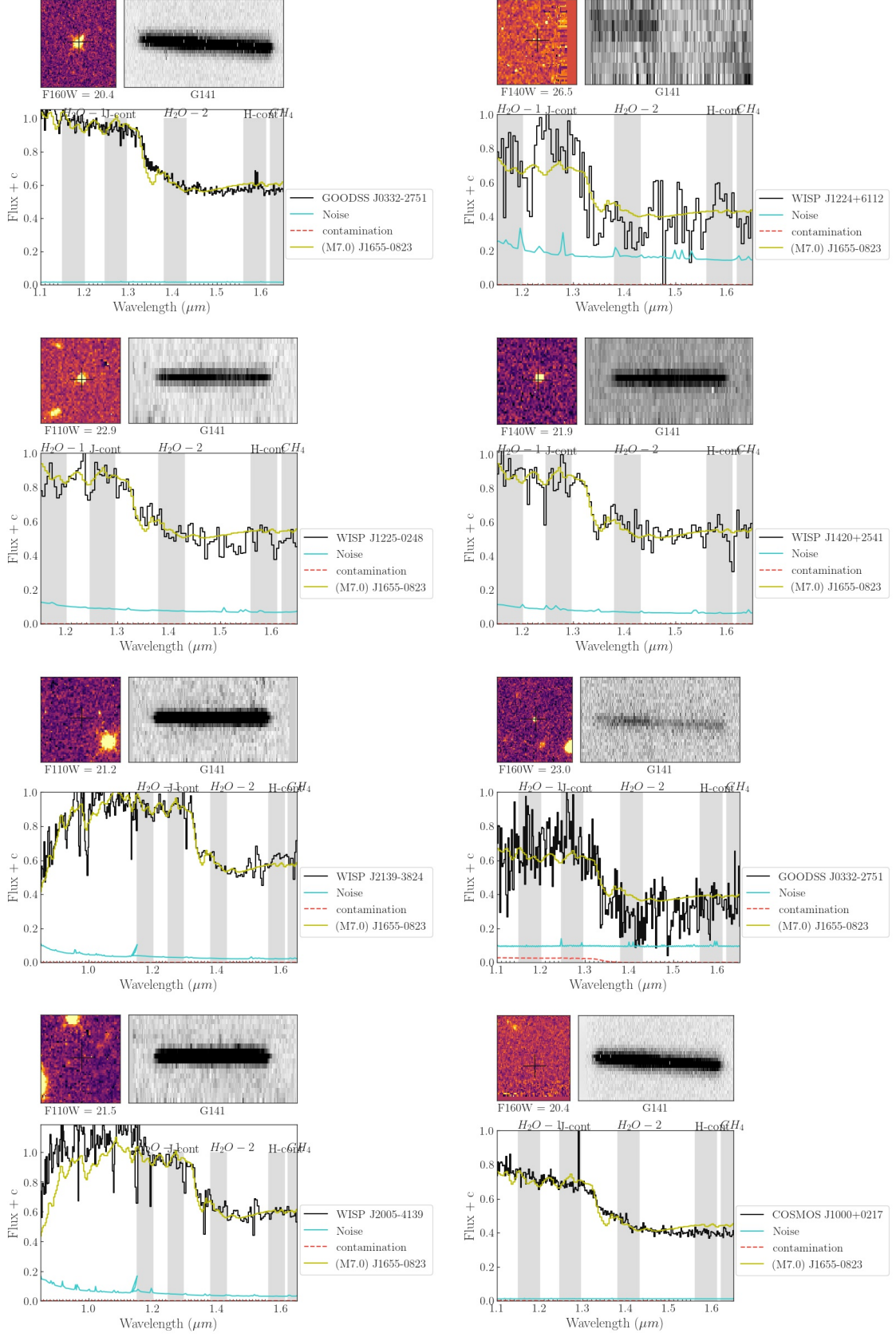


Figure 20. cont.

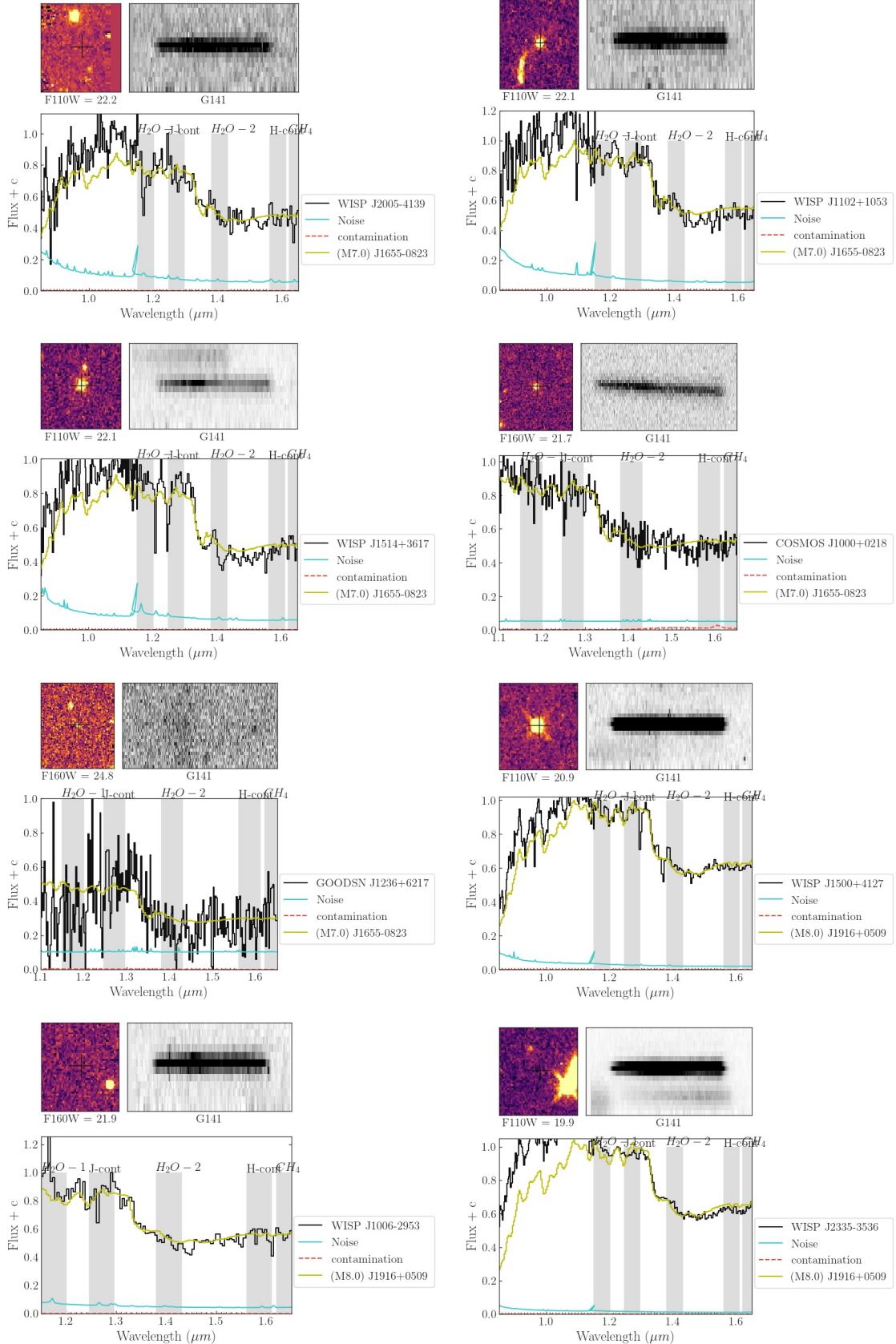
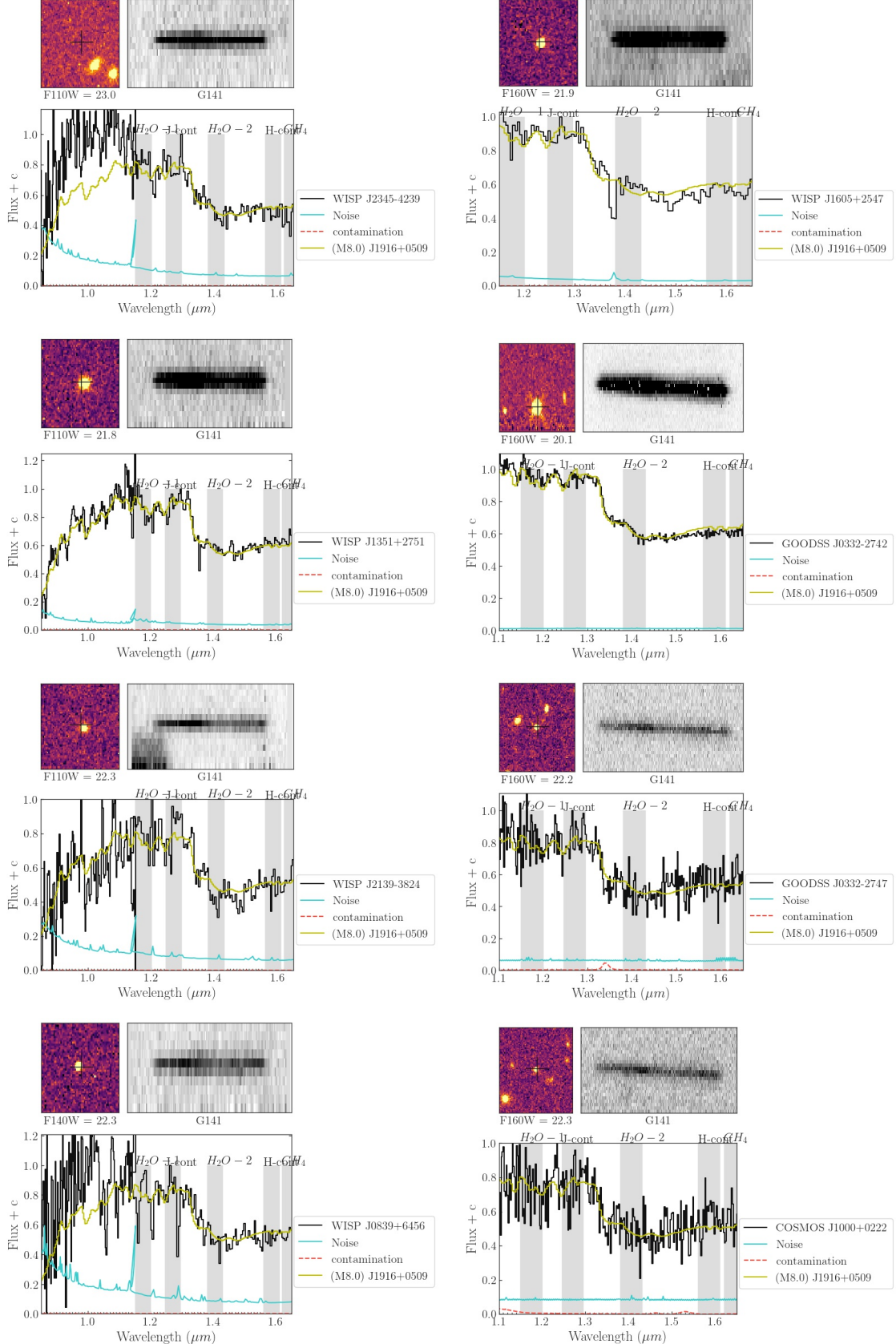
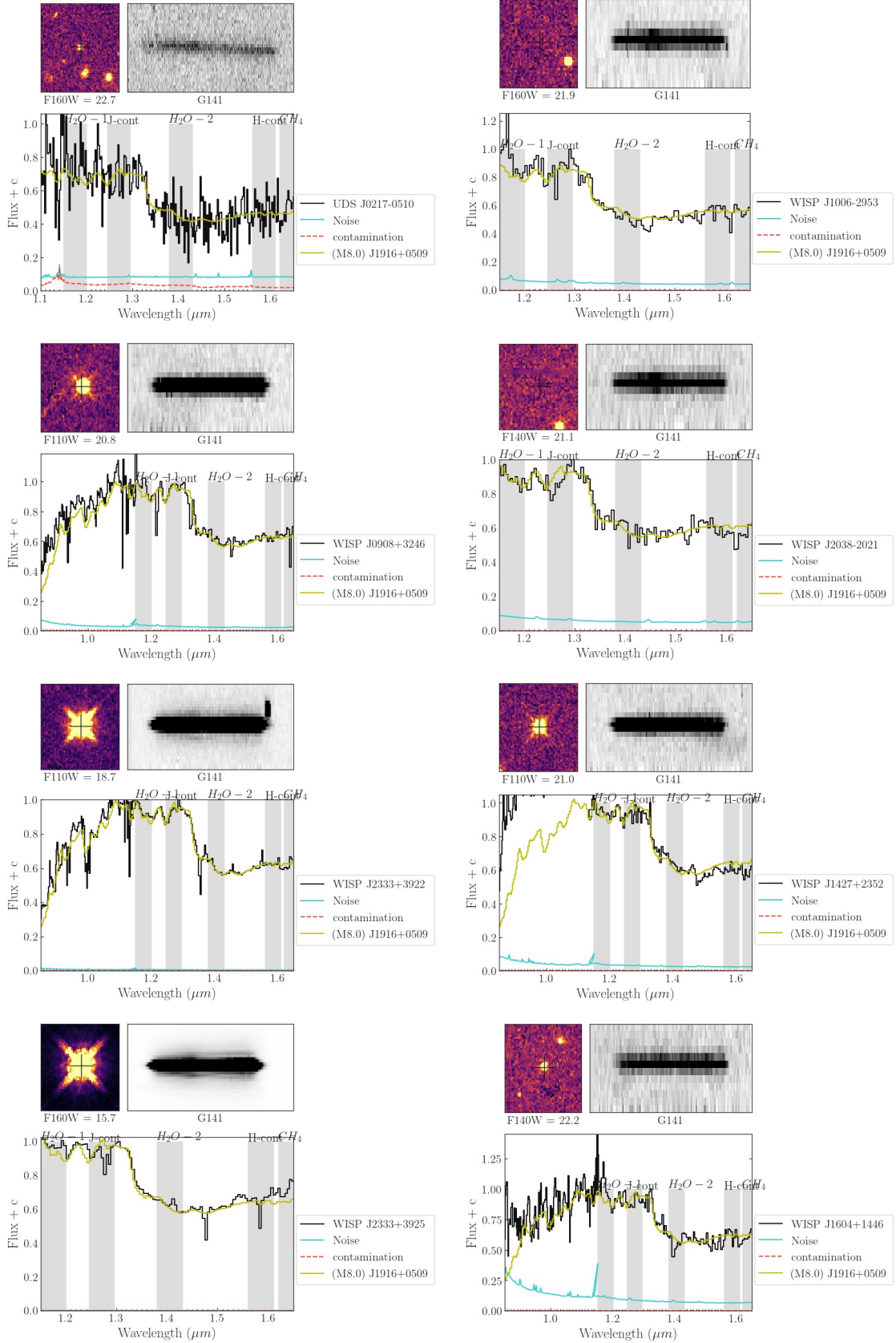
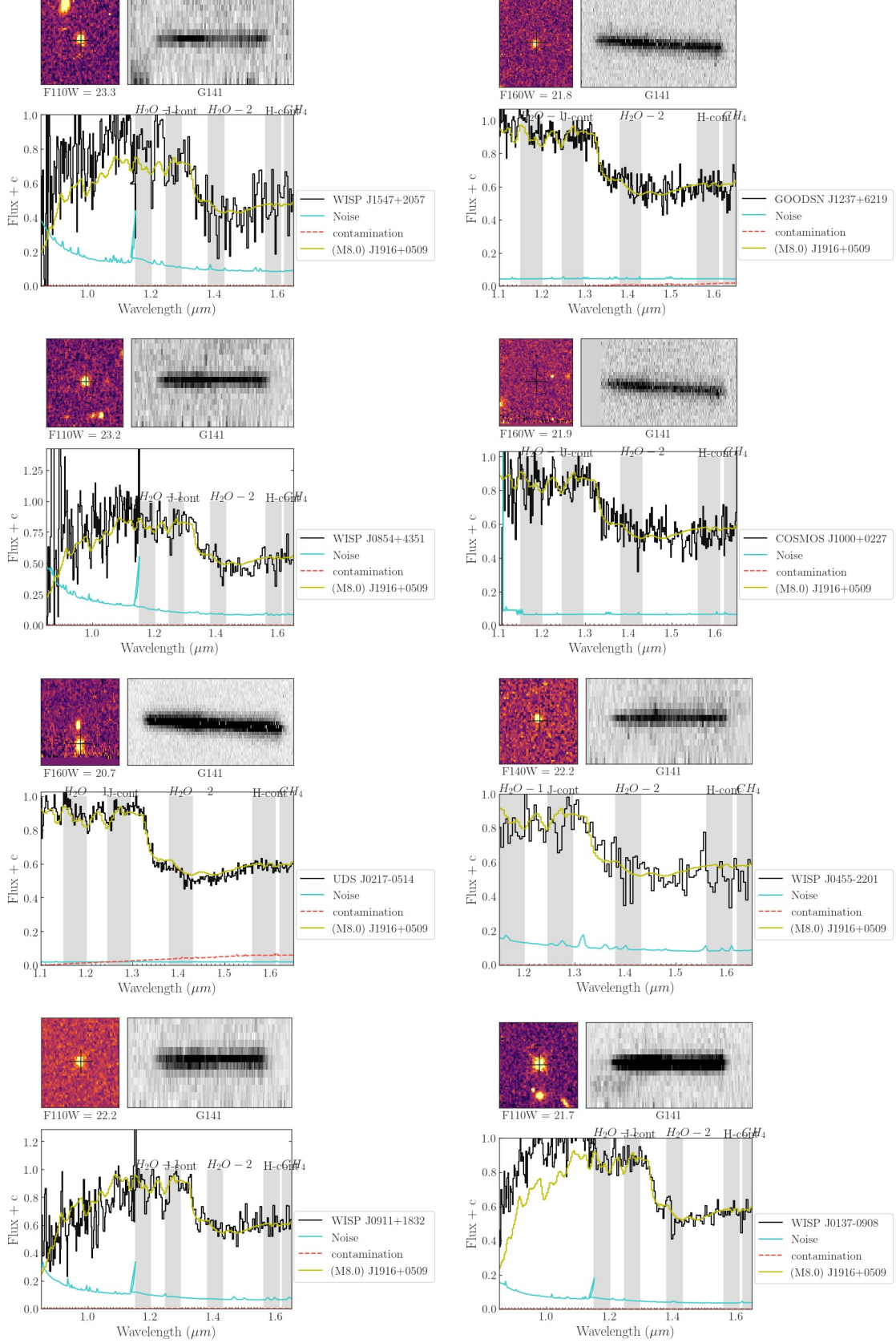
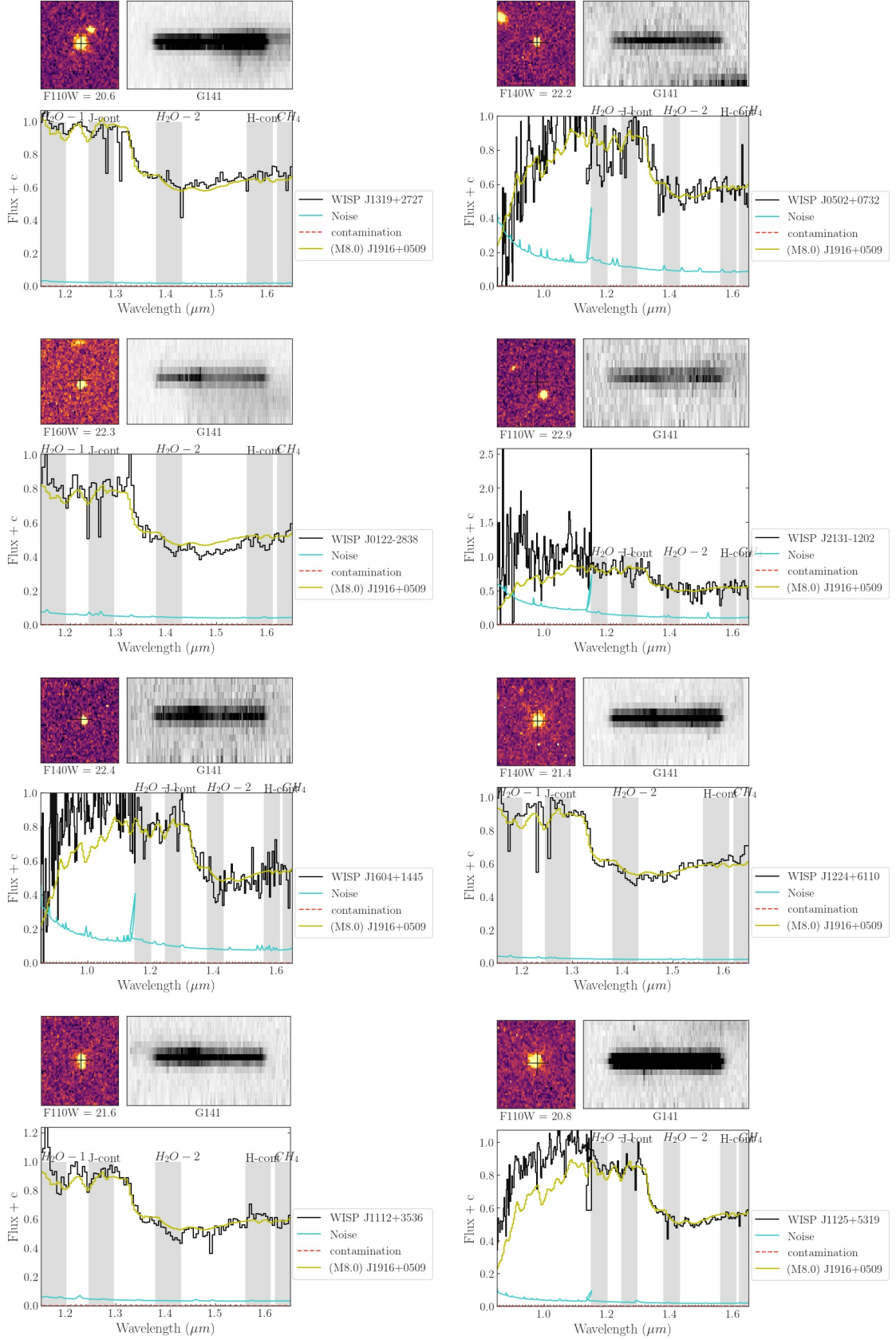


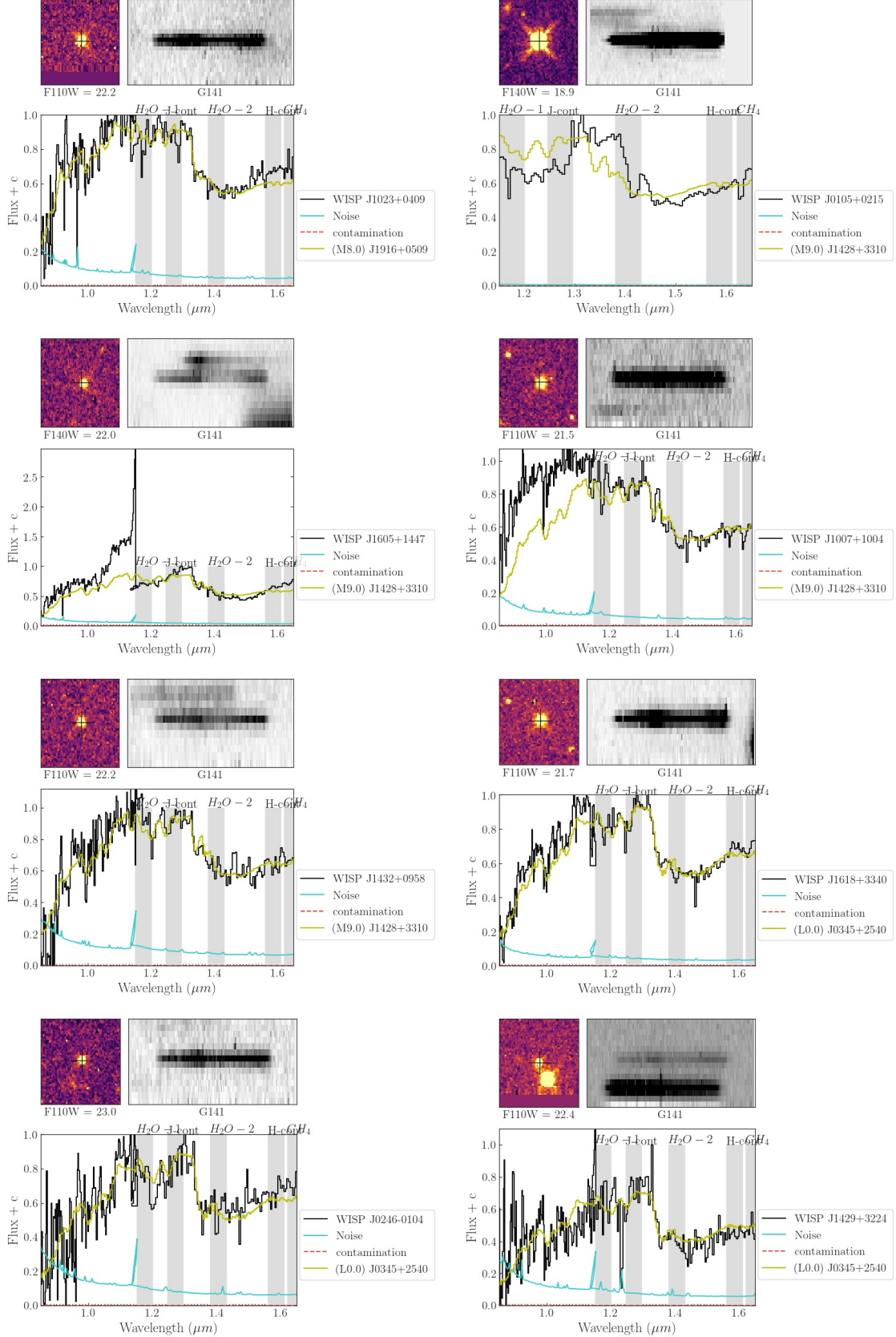
Figure 21. cont.

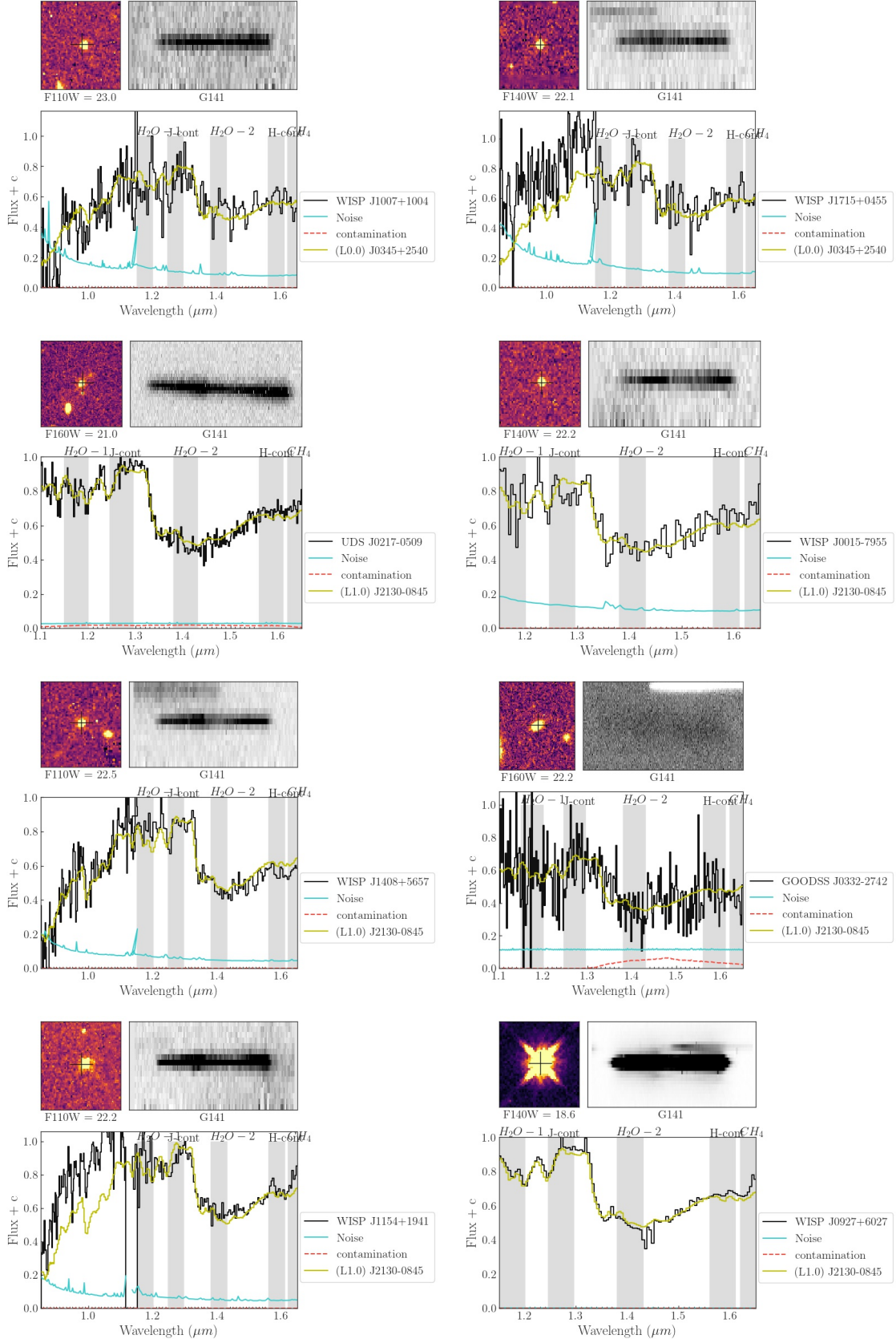
**Figure 22.** cont.

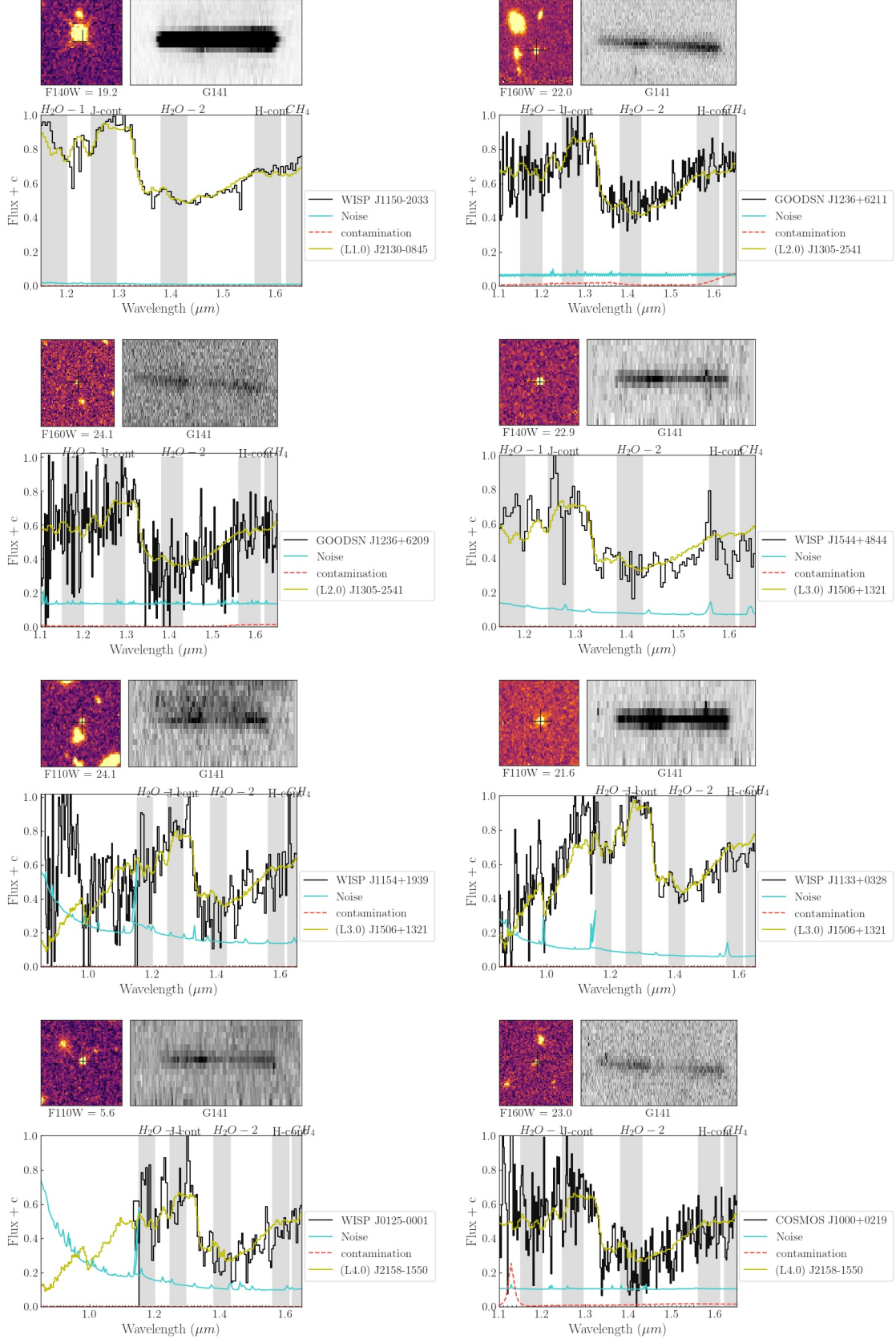
**Figure 23.** cont.

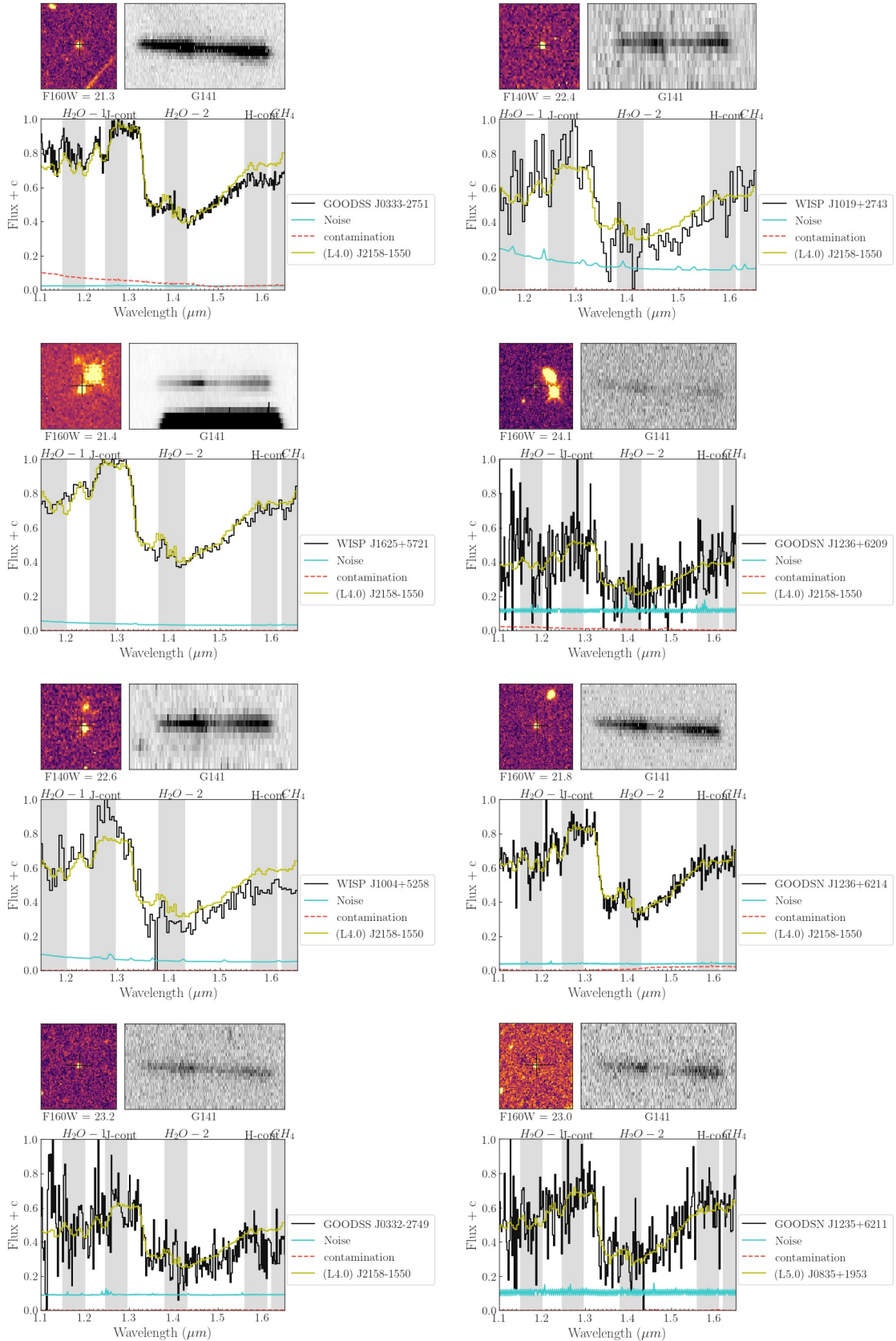
**Figure 24.** cont.

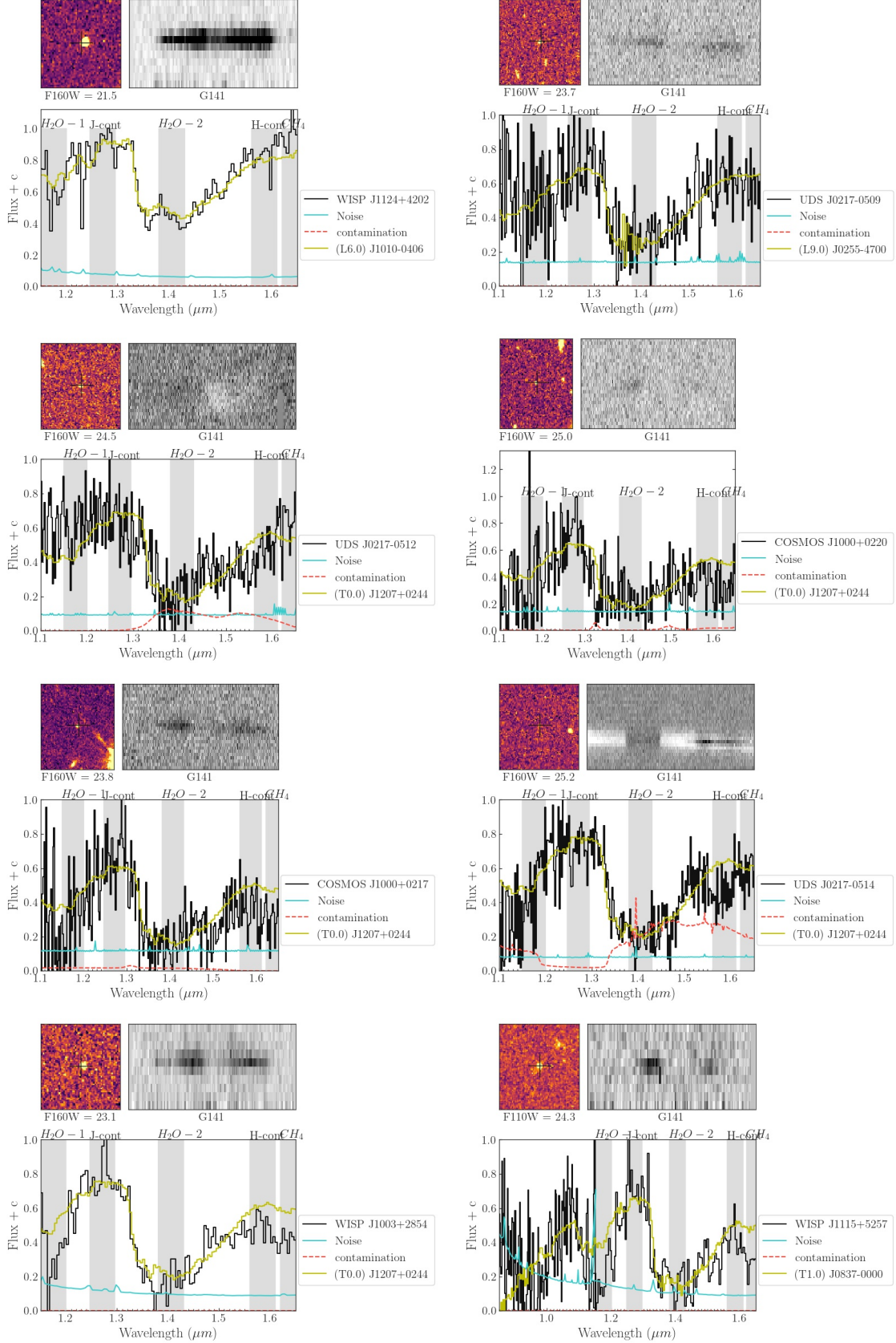
**Figure 25. cont.**

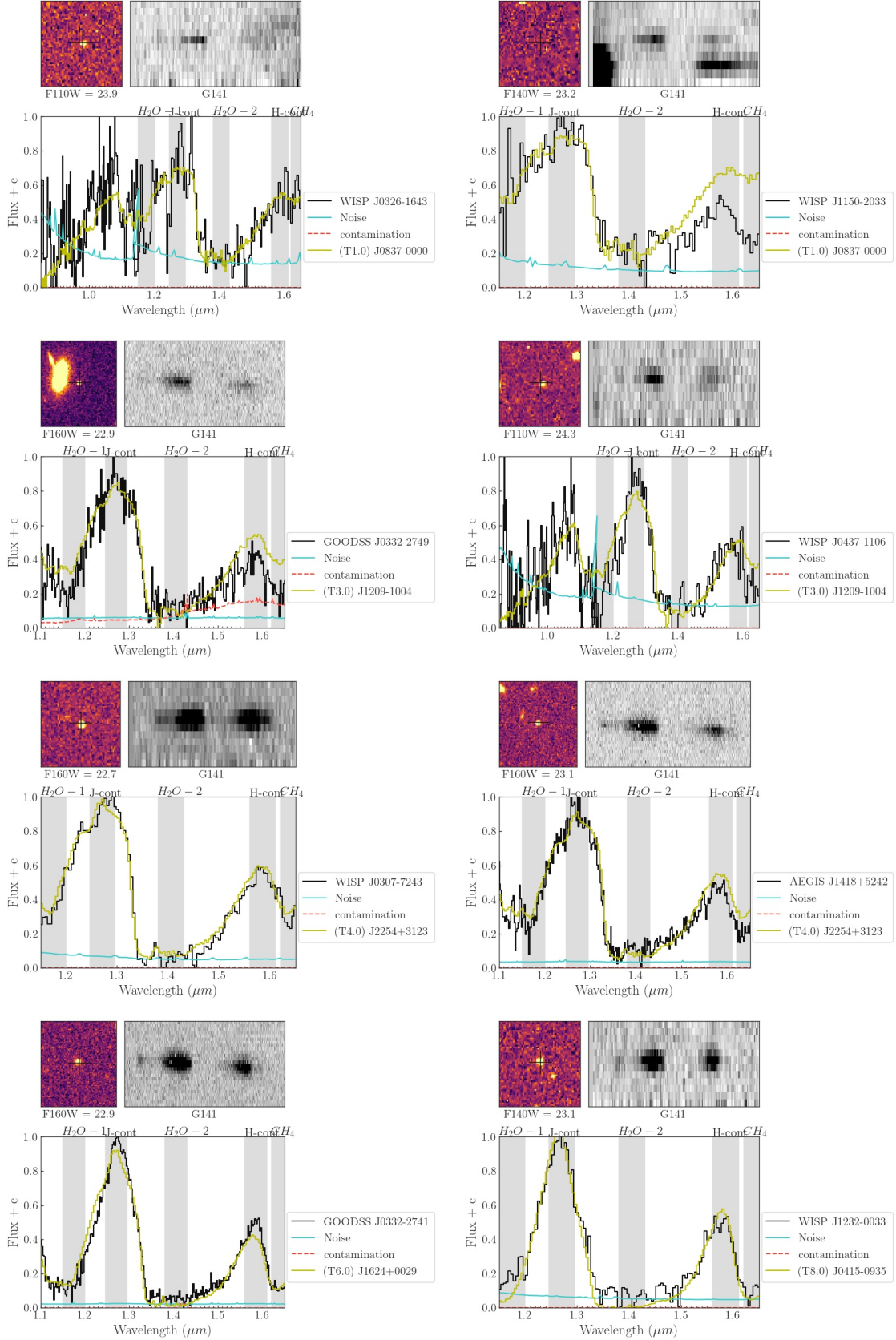
**Figure 26.** cont.

**Figure 27. cont.**

**Figure 28.** cont.

**Figure 29.** cont.

**Figure 30.** cont.

**Figure 31. cont.**

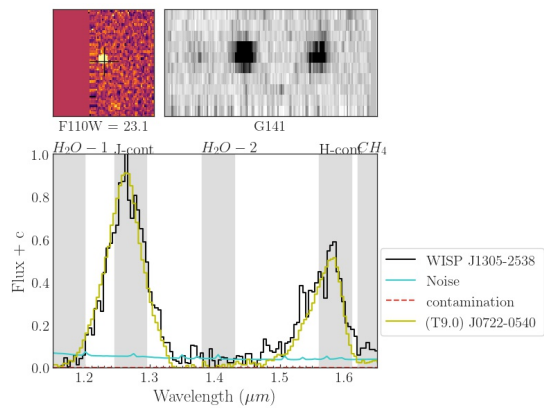


Figure 32. cont.

Table 1. Polynomial relations used in this work. They are computed as $y = \sum_{n=1}^7 c_n x^n$ and the symbol E denotes powers of 10.

x	y	rms	coefficients						
			c7	c6	c5	c4	c3	c2	c1
SpT	AbsF110W	0.06	3.63345085E-07	-5.02613549E-05	2.84851659E-03	-8.39195901E-02	1.32290107	-9.72381583	3.09629558E+01
SpT	AbsF140W	0.06	4.22490192E-07	-5.96021230e-05	3.42842203E-03	-1.01908640E-01	1.61590803	-1.21235933E+01	3.83212564E+01
SpT	AbsF160W	0.07	9.52399647E-07	-1.35594583E-04	7.81820247E-03	-2.32176348E-01	3.70383710	-2.92211368E01	9.38498953E01
F110W	logSNR-J	0.4				-0.01948568	0.56986169	-1.93458271	
F140W	logSNR-J	0.4				0.02524522	-1.36255952	18.89785712	
F160W	logSNR-J	0.4				1.02681325E-02	-7.04396841E-01	1.16675349E+01	

Table 2. Selection Criteria

SpT Range	X-axis	Y-axis	v1	v2	v3	v4	CP	CT	FP
L0-L5	H ₂ O-1/J-Cont	H ₂ O-2/H ₂ O-1	(0.65, 0.82)	(0.97, 0.82)	(0.97, 0.48)	(0.65, 0.48)	0.97	0.065	0.9
L5-T0	H ₂ O-1/J-Cont	CH ₄ /H-Cont	(0.54, 1.21)	(0.92, 1.21)	(0.92, 0.9)	(0.54, 0.9)	0.96	0.054	0.95
M7-L0	H ₂ O-1/J-Cont	CH ₄ /H ₂ O-1	(0.81, 0.97)	(1.09, 0.97)	(1.09, 0.48)	(0.81, 0.48)	0.96	0.173	0.81
T0-T5	H ₂ O-2/J-Cont	H-cont/J-Cont	(0.02, 0.78)	(0.39, 1.1)	(0.39, 0.58)	(0.02, 0.25)	0.98	0.02	0.88
T5-T9	H ₂ O-2/J-Cont	CH ₄ /H-Cont	(-0.01, 0.39)	(0.08, 0.61)	(0.08, 0.16)	(-0.01, -0.06)	0.98	0.002	0.71
Y dwarfs	H ₂ O-2+CH ₄ /J-cont	H ₂ O-1+CH ₄ /H-cont	(-0.22, 0.35)	(0.28, 0.35)	(0.28, -0.2)	(-0.22, -0.2)	0.93	0.002	1.0
subdwarfs	H ₂ O-1/J-Cont	H-cont/J-Cont	(0.9, 0.61)	(1.06, 0.67)	(1.06, 0.56)	(0.9, 0.5)	0.86	0.039	1.0

Table 3. List of L0-T9 UCDs

ShortName	GrismID	SNR-J	SpT	RA	DEC	F110W	F140W	F160W	Distance(pc)	Distance
WISPJ1354+1801	PAR361-00004	145	M7	208.564117	18.033100	18.5		19.0	442	117
WISPJ1550+3959	PAR59-00072	13	M7	237.595795	39.991620		22.8		2906	92
WISPJ1402+0946	PAR143-00045	11	M7	210.603149	9.769180	22.1		21.9	1908	234
WISPJ1427+2631	PAR218-00004	93	M7	216.788986	26.524500		18.3		366	11
WISPJ0910+3328	PAR431-00028	11	M7	137.621338	33.466900	21.5		21.3	1468	201
WISPJ2307+2112	PAR166-00041	17	M7	346.821686	21.208400			21.5	1834	79
GOODSSJ0333-2751	GOODSS-28-G141_12490	18	M7	53.262383	-27.853979		22.0	22.2	2238	213
WISPJ1342+1841	PAR139-00010	70	M7	205.607071	18.696800			20.2	1002	42

Table 3 continued on next page

Table 3 (*continued*)

ShortName	GrismID	SNR_J	Spt	RA	DEC	F110W	F140W	F160W	Distance(pc)	Distance
WISPJ1556+2107	PAR308-00020	12	M7	239.138168	21.131900	21.3		21.1	1341	190
WISPJ1431+2447	PAR385-00049	11	M7	217.854019	24.797000	22.8		22.2	2436	106
AEGISJ1418+5244	AEGIS-25-G141_18460	10	M7	214.742126	52.745266		22.8	22.8	3141	219
WISPJ0947+5126	PAR478-00038	17	M7	146.750015	51.442600	22.3		21.6	1867	90
WISPJ1847-6858	PAR134-00163	9	M7	281.901306	-68.969000			22.6	3013	127
WISPJ1556+2108	PAR308-00050	6	M7	239.120377	21.136500	22.5		22.5	2409	405
WISPJ1250-2331	PAR325-00034	20	M7	192.672379	-23.530000	21.6		21.3	1492	138
WISPJ0944-1940	PAR293-00045	13	M7	146.159622	-19.679000		21.5		1639	52
WISPJ1437-0149	PAR66-00029	20	M7	219.364258	-1.828590	21.4		21.6	1541	340
WISPJ1847-6858	PAR134-00071	24	M7	281.901581	-68.969000			21.2	1554	63
WISPJ2040-0644	PAR248-00079	17	M7	310.109924	-6.737800		21.6		1731	55
GOODSNJ1236+6218	GOODSN-16-G141_33587	22	M7	189.242218	62.314220		21.8	21.8	1995	108
WISPJ1005-2305	PAR349-00092	5	M7	151.402130	-23.096000	23.0		22.9	3018	453
WISPJ1323+3434	PAR186-00091	6	M7	200.928772	34.578900		22.2		2292	73
GOODSNJ1236+6209	GOODSN-21-G141_04680	11	M7	189.057877	62.161026		22.5	22.5	2684	173
WISPJ1009+3000	PAR39-00033	10	M7	152.409225	30.012280	21.7	22.0	21.1	1654	318
WISPJ2225-7212	PAR404-00044	15	M7	336.405060	-72.208000	21.9		21.7	1759	239
GOODSSJ0332-2752	GOODSS-13-G141_07509	16	M7	53.123314	-27.874628		22.0	22.0	2181	117
WISPJ1427+2631	PAR218-00032	13	M7	216.803177	26.519000		21.4		1566	49
WISPJ1832+5345	PAR124-00065	13	M7	278.138306	53.753000	22.1		22.1	2051	342
WISPJ2205-0017	PAR94-00043	13	M7	331.366730	-0.285350	22.2		22.0	2002	271
GOODSSJ0332-2745	GOODSS-09-G141_32414	17	M7	53.080120	-27.762650		22.3	22.1	2378	101
WISPJ1242+3538	PAR439-00106	4	M7	190.664185	35.638200	24.1		23.4	4228	160
WISPJ1011-0447	PAR406-00062	11	M7	152.756714	-4.798300	22.5		22.4	2411	358
UDSJ0217-0513	UDS-15-G141_15337	160	M7	34.263683	-5.226482		19.0	19.0	537	32
AEGISJ1419+5253	AEGIS-06-G141_12749	10	M7	214.981369	52.892410		22.6	22.5	2768	126
WISPJ1046+1302	PAR116-00048	11	M7	161.706467	13.044400			22.2	2488	101
WISPJ1256+5430	PAR110-00085	15	M7	194.249939	54.515200			22.4	2686	113
WISPJ1410+2954	PAR222-00091	4	M7	212.550674	29.914000		23.1		3500	108
UDSJ0217-0509	UDS-25-G141_36035	42	M7	34.340759	-5.155810		21.0	21.0	1381	82
WISPJ2345+1510	PAR77-00045	12	M7	356.250092	15.176390			21.7	1962	81
WISPJ0926+1239	PAR92-00011	27	M7	141.534668	12.664310			20.7	1262	53
WISPJ0944-1941	PAR293-00059	8	M7	146.153305	-19.696000		21.9		2013	63
WISPJ0948+1350	PAR427-00039	21	M7	147.228485	13.841600	22.4		22.1	2172	274

Table 3 *continued on next page*

Table 3 (*continued*)

ShortName	GrismID	SNR_J	Spt	RA	DEC	F110W	F140W	F160W	Distance(pc)	Distance
WISPJ2333+3921	PAR68-00027	38	M7	353.408569	39.359250	20.5		20.3	927	118
WISPJ1024-1843	PAR179-00069	13	M7	156.183685	-18.723000		22.0		2049	66
WISPJ1832+5344	PAR124-00053	18	M7	278.104370	53.743200	21.9		21.8	1789	271
WISPJ2222+0937	PAR50-00007	64	M7	335.595337	9.619006		19.7		715	22
UDSJ0217-0513	UDS-09-G141_17647	21	M7	34.317680	-5.217520		21.6	21.6	1824	124
GOODSSJ0332-2755	GOODSS-05-G141_01783	13	M7	53.086269	-27.917154		22.1	22.1	2269	145
WISPJ2133-4904	PAR133-00012	87	M7	323.482574	-49.083000			19.6	753	31
WISPJ1427+5751	PAR5-00055	19	M7	216.801208	57.850704	22.6	22.4		2297	173
WISPJ1340+2825	PAR433-00047	14	M7	205.238373	28.421200	21.9		22.2	2026	489
WISPJ1703+6136	PAR155-00040	22	M7	255.800537	61.614300			21.6	1925	77
WISPJ0122-2837	PAR128-00034	16	M7	20.700928	-28.631500			21.9	2202	91
UDSJ0216-0513	UDS-21-G141_14877	41	M7	34.248672	-5.227246		20.9	20.8	1275	66
WISPJ2307+2112	PAR166-00044	15	M7	346.819458	21.202500			21.6	1886	77
WISPJ1545+0933	PAR138-00108	7	M7	236.393112	9.559070			22.8	3269	136
UDSJ0217-0508	UDS-05-G141_41125	36	M7	34.384212	-5.136668		20.9	20.9	1316	87
GOODSSJ0332-2750	GOODSS-19-G141_16588	35	M7	53.069553	-27.835718		21.2	21.1	1463	77
WISPJ1023+0409	PAR347-00017	37	M7	155.843842	4.156480	20.7		20.5	1001	126
WISPJ1720+4805	PAR398-00028	32	M7	260.024841	48.085900	21.3		20.8	1227	91
WISPJ0307-7245	PAR130-00076	8	M7	46.930344	-72.760500			22.4	2775	116
COSMOSJ1000+0212	COSMOS-14-G141_02407	23	M7	150.114136	2.203750		21.4	21.4	1653	109
WISPJ1303+2952	PAR35-00023	43	M7	195.952576	29.867760	20.9	20.8	20.5	1107	92
WISPJ1556+6345	PAR154-00054	17	M7	239.238632	63.751900			22.1	2366	100
AEGISJ1419+5253	AEGIS-11-G141_37605	23	M7	214.830063	52.883358		21.7	21.7	1883	90
GOODSNJ1236+6207	GOODSN-31-G141_01429	23	M7	189.105484	62.131878		22.0	22.0	2155	130
WISPJ1305-2538	PAR32-00044	17	M7	196.330322	-25.638200	22.4	22.0	22.4	2234	354
UDSJ0217-0515	UDS-14-G141_05410	31	M7	34.396893	-5.259149		21.3	21.2	1525	88
WISPJ1419+0606	PAR345-00016	46	M7	214.868134	6.107460	20.8		20.7	1079	158
WISPJ1545+1155	PAR290-00009	76	M7	236.311707	11.916900		19.2		556	17
GOODSSJ0332-2748	GOODSS-02-G141_21166	11	M7	53.075310	-27.812702		22.5	22.5	2731	188
WISPJ2005-4140	PAR371-00100	7	M7	301.439331	-41.667000	22.6		22.5	2448	372
WISPJ1703+6135	PAR155-00094	7	M7	255.803131	61.589400			22.6	3013	120
WISPJ1007+5013	PAR98-00038	21	M7	151.942719	50.227020			21.5	1788	77
WISPJ1147-1406	PAR177-00049	5	M7	176.790482	-14.103000		22.5		2681	90
GOODSNJ1237+6215	GOODSN-36-G141_22694	47	M7	189.333832	62.252960		20.8	20.8	1257	79

Table 3 continued on next page

Table 3 (*continued*)

ShortName	GrismID	SNR_J	Spt	RA	DEC	F110W	F140W	F160W	Distance(pc)	Distance
WISPJ1348+2451	PAR243-00025	10	M7	207.047501	24.864700		21.7		1792	57
WISPJ1534+1252	PAR457-00025	16	M7	233.733124	12.881000	21.5		21.6	1569	293
GOODSSJ0333-2751	GOODSS-28-G141_12948	22	M7	53.288685	-27.851252		21.7	21.9	1951	183
UDSJ0217-0514	UDS-14-G141_11264	21	M7	34.419510	-5.239141		21.7	21.7	1855	103
WISPJ2005-4139	PAR371-00045	19	M7	301.436218	-41.656000	21.3		21.2	1368	203
WISPJ0935+0201	PAR34-00057	9	M7	143.753418	2.025816	22.0	22.6	22.3	2300	494
WISPJ0950+3544	PAR192-00026	18	M7	147.742004	35.734600		21.5		1608	50
WISPJ1135+2558	PAR183-00051	5	M7	173.825058	25.980000	22.5		22.4	2376	352
WISPJ1410+2955	PAR222-00047	8	M7	212.553284	29.928500		22.1		2178	68
WISPJ1005-2421	PAR336-00047	10	M7	151.336197	-24.362000	22.1		22.0	2003	321
GOODSNJ1237+6210	GOODSN-43-G141_05553	78	M7	189.291306	62.168911		20.3	20.3	981	67
WISPJ0243-7211	PAR127-00028	33	M7	40.788712	-72.193700			20.7	1226	51
UDSJ0217-0513	UDS-15-G141_14762	17	M7	34.261978	-5.227352		21.9	21.9	2068	99
WISPJ0914+4755	PAR299-00070	12	M7	138.669785	47.929800	22.7		22.4	2477	263
GOODSNJ1236+6210	GOODSN-43-G141_05338	88	M7	189.236938	62.167187		20.0	19.9	837	47
WISPJ1402+5410	PAR458-00004	107	M7	210.689911	54.173500	19.1		18.9	479	65
WISPJ1611+5221	PAR161-00061	11	M7	242.944473	52.355100			22.3	2658	109
GOODSNJ1236+6214	GOODSN-13-G141_20147	29	M7	189.076431	62.240665		21.8	21.7	1921	104
WISPJ1330+2810	PAR52-00082	7	M7	202.618713	28.175410		23.2		3587	118
WISPJ1325+2233	PAR436-00037	20	M7	201.376205	22.555500	21.8		21.2	1529	90
GOODSSJ0332-2751	GOODSS-06-G141_10354	57	M7	53.232479	-27.862617		20.5	20.4	1052	58
WISPJ1224+6112	PAR422-00561	4	M7	186.122742	61.211100		26.5		16818	653
WISPJ1225-0248	PAR38-00076	9	M7	186.307083	-2.805970	22.9	22.8	22.1	2611	254
WISPJ1420+2541	PAR301-00038	9	M7	215.205597	25.691600		21.9		1932	62
WISPJ2139-3824	PAR309-00023	29	M7	324.799408	-38.403000	21.2		20.9	1230	129
GOODSSJ0332-2751	GOODSS-06-G141_11322	7	M7	53.219978	-27.857151		23.2	23.0	3576	150
WISPJ2005-4139	PAR371-00055	20	M7	301.420959	-41.655000	21.5		20.9	1346	62
COSMOSJ1000+0217	COSMOS-12-G141_10098	54	M7	150.127716	2.283806		20.3	20.4	1007	71
WISPJ2005-4139	PAR371-00080	10	M7	301.422119	-41.650000	22.2		21.8	1942	178
WISPJ1102+1053	PAR11-00046	11	M7	165.566360	10.897610	22.1	22.2	21.6	1978	240
WISPJ1514+3617	PAR71-00034	10	M7	228.531723	36.291910	22.1		21.9	1921	249
COSMOSJ1000+0218	COSMOS-26-G141_12464	16	M7	150.081543	2.306208		21.7	21.7	1854	109
GOODSNJ1236+6217	GOODSN-15-G141_29162	4	M7	189.171143	62.285847		25.1	24.8	8556	353
WISPJ1500+4127	PAR391-00011	33	M8	225.079330	41.457200	20.9		20.7	899	123

Table 3 *continued on next page*

Table 3 (*continued*)

ShortName	GrismID	SNR_J	SPT	RA	DEC	F110W	F140W	F160W	Distance(pc)	Distance
WISPJ1006-2953	PAR170-00081	13	M8	151.730759	-29.894000			21.9	1757	74
WISPJ2335-3536	PAR359-00007	58	M8	353.832611	-35.602000	19.9		19.6	542	66
WISPJ2345-4239	PAR356-00057	8	M8	356.253845	-42.658000	23.0		22.7	2275	232
WISPJ1605+2547	PAR148-00044	21	M8	241.354004	25.794100			21.9	1765	76
WISPJ1351+2751	PAR444-00034	16	M8	207.753510	27.852400	21.8		21.5	1293	153
GOODSSJ0332-2742	GOODSS-30-G141_44380	74	M8	53.100697	-27.703068		20.1	20.1	723	35
WISPJ2139-3824	PAR309-00046	9	M8	324.795837	-38.402000	22.3		22.4	1826	346
GOODSSJ0332-2747	GOODSS-02-G141_24465	13	M8	53.075794	-27.796272		22.3	22.2	1959	100
WISPJ0839+6456	PAR250-00051	7	M8	129.813751	64.949100		22.3		1940	61
COSMOSJ1000+0222	COSMOS-25-G141_19163	9	M8	150.107285	2.374017		22.5	22.3	2130	80
UDSJ0217-0510	UDS-23-G141_31620	9	M8	34.259209	-5.170456		22.7	22.7	2418	180
WISPJ1006-2953	PAR171-00081	13	M8	151.730759	-29.894000			21.9	1757	72
WISPJ0908+3246	PAR417-00014	30	M8	137.048172	32.776600	20.8		20.3	774	61
WISPJ2038-2021	PAR197-00054	12	M8	309.592621	-20.363000		21.1		1101	35
WISPJ2333+3922	PAR68-00017	146	M8	353.398834	39.370580	18.7		18.7	339	63
WISPJ1427+2352	PAR346-00021	29	M8	216.753586	23.878400	21.0		20.9	958	169
WISPJ2333+3925	PAR153-00002	518	M8	353.414642	39.418100			15.7	102	4
WISPJ1604+1446	PAR240-00051	10	M8	241.234528	14.782200		22.2		1863	59
WISPJ1547+2057	PAR335-00113	7	M8	236.926895	20.951200	23.3		23.0	2654	297
GOODSNJ1237+6219	GOODSN-27-G141_34168	20	M8	189.308624	62.318092		21.8	21.8	1583	98
WISPJ0854+4351	PAR319-00085	7	M8	133.500824	43.853300	23.2		22.9	2502	274
COSMOSJ1000+0227	COSMOS-08-G141_26927	13	M8	150.126282	2.459579		22.0	21.9	1690	73
UDSJ0217-0514	UDS-10-G141_10211	46	M8	34.368454	-5.242865		20.7	20.7	959	42
WISPJ0455-2201	PAR194-00039	7	M8	73.960762	-22.023700		22.2		1811	56
WISPJ0911+1832	PAR271-00055	10	M8	137.887695	18.541900	22.2		21.8	1562	143
WISPJ0137-0908	PAR317-00032	17	M8	24.328993	-9.148480	21.7		21.1	1170	79
WISPJ1319+2727	PAR47-00010	39	M8	199.900848	27.450940	20.6	20.5	20.5	813	107
WISPJ0502+0732	PAR189-00077	7	M8	75.559814	7.535803		22.2		1863	60
WISPJ0122-2838	PAR128-00052	14	M8	20.687748	-28.646200			22.3	2116	84
WISPJ2131-1202	PAR342-00050	6	M8	322.946167	-12.045000	22.9		22.6	2161	250
WISPJ1604+1445	PAR240-00058	8	M8	241.243622	14.766600		22.4		2013	64
WISPJ1224+6110	PAR422-00021	30	M8	186.109833	61.182500		21.4		1233	38
WISPJ1112+3536	PAR44-00044	19	M8	168.058868	35.607950	21.6	22.2	21.6	1457	312
WISPJ1125+5319	PAR477-00009	32	M8	171.342133	53.331300	20.8		20.4	814	84

Table 3 *continued on next page*

Table 3 (*continued*)

ShortName	GrismID	SNR_J	Spt	RA	DEC	F110W	F140W	F160W	Distance(pc)	Distance
WISPJ1023+0409	PAR347-00037	14	M8	155.843643	4.164820	22.2		22.0	1594	213
WISPJ0105+0215	PAR231-00012	89	M9	16.310194	2.257870		18.9		335	10
WISPJ1605+1447	PAR240-00040	17	M9	241.256699	14.783400		22.0		1343	43
WISPJ1007+1004	PAR343-00036	15	M9	151.918076	10.079000	21.5		21.2	942	136
WISPJ1432+0958	PAR428-00062	9	M9	218.003204	9.968530	22.2		22.0	1327	194
WISPJ1618+3340	PAR65-00035	19	L0	244.707458	33.671520	21.7		21.3	832	116
WISPJ0246-0104	PAR483-00077	9	L0	41.721233	-1.079250	23.0		22.1	1346	52
WISPJ1429+3224	PAR378-00052	8	L0	217.333206	32.416400	22.4		21.9	1142	119
WISPJ1007+1004	PAR343-00083	6	L0	151.936081	10.079100	23.0		22.4	1452	111
WISPJ1715+0455	PAR239-00118	6	L0	258.758057	4.925150		22.1		1198	38
UDSJ0217-0509	UDS-25-G141_36758	31	L1	34.318333	-5.153692		21.3	21.0	712	26
WISPJ0015-7955	PAR244-00072	6	L1	3.785810	-79.930220		22.2		1073	34
WISPJ1408+5657	PAR353-00055	13	L1	212.082855	56.956800	22.5		22.0	1000	125
GOODSSJ0332-2742	GOODSS-35-G141_43501	5	L1	53.110023	-27.707857		22.4	22.2	1211	52
WISPJ1154+1941	PAR338-00035	13	L1	178.716644	19.684700	22.2		21.9	937	159
WISPJ0927+6027	PAR21-00005	324	L1	141.989319	60.462970		18.6		199	6
WISPJ1150-2033	PAR199-00009	57	L1	177.706833	-20.561000		19.2		266	8
GOODSNJ1236+6211	GOODSN-33-G141_09283	12	L2	189.223923	62.188259		22.2	22.0	941	40
GOODSNJ1236+6209	GOODSN-31-G141_04491	5	L2	189.082870	62.159412		24.3	24.1	2474	147
WISPJ1544+4844	PAR54-00072	6	L3	236.225174	48.738480		22.9		1092	33
WISPJ1154+1939	PAR338-00136	4	L3	178.720154	19.660000	24.1		23.1	1359	70
WISPJ1133+0328	PAR27-00036	10	L3	173.274353	3.477643	21.6	22.0	21.4	602	133
WISPJ0125-0001	PAR365-00156	4	L4	21.396976	-0.027310	5.6		24.2	1056	1057
COSMOSJ1000+0219	COSMOS-03-G141_14879	6	L4	150.093170	2.331386		23.2	23.0	1174	65
GOODSSJ0333-2751	GOODSS-28-G141_10859	34	L4	53.267498	-27.860249		21.4	21.3	512	45
WISPJ1019+2743	PAR201-00044	4	L4	154.888565	27.720400		22.4		772	24
WISPJ1625+5721	PAR156-00041	19	L4	246.353882	57.357600			21.4	569	25
GOODSNJ1236+6209	GOODSN-32-G141_05180	4	L4	189.159195	62.164200		24.2	24.1	1902	135
WISPJ1004+5258	PAR438-00051	10	L4	151.204559	52.974800		22.6		850	27
GOODSNJ1236+6214	GOODSN-24-G141_21552	19	L4	189.161880	62.247669		22.0	21.8	672	36
GOODSSJ0332-2749	GOODSS-20-G141_19648	6	L4	53.103283	-27.820263		23.2	23.2	1207	89
GOODSNJ1235+6211	GOODSN-11-G141_10603	6	L5	188.967987	62.194958		23.3	23.0	1063	44
WISPJ1124+4202	PAR106-00047	11	L6	171.034760	42.042900			21.5	469	20
UDSJ0217-0509	UDS-23-G141_32939	4	L9	34.250679	-5.165653		23.9	23.7	967	37

Table 3 continued on next page

Table 4. Number of UCDs expected as a function of scale height

h	M7-L0	L0-L5	L5-T0	T0-T5	T5-Y0
100	3	3	1	1	0
200	40	25	7	2	1
250	87	44	10	2	1
300	160	70	15	3	1
350	272	105	18	4	1
400	372	133	20	4	2
600	1014	259	32	6	2
observed	148	26	3	12	2

Table 3 (continued)

ShortName	GrismID	SNR_J	Spt	RA	DEC	F110W	F140W	F160W	Distance(pc)	Distance
UDSJ0217-0512	UDS-11-G141_18287	7	T0	34.451412	-5.214653	24.7	24.5	1335	57	
COSMOSJ1000+0220	COSMOS-09-G141_16730	4	T0	150.178040	2.349691	24.5	25.0	1414	185	
COSMOSJ1000+0217	COSMOS-23-G141_10232	5	T0	150.145950	2.283675	23.8	23.8	910	35	
UDSJ0217-0514	UDS-12-G141_10759	9	T0	34.435657	-5.240000	25.2	25.2	1796	85	
WISPJ1003+2854	PAR191-00077	6	T0	150.918884	28.912800	23.1	661	28		
WISPJ1115+5257	PAR468-00163	5	T1	168.809311	52.951400	24.3	24.4	942	210	
WISPJ0326-1643	PAR467-00135	3	T1	51.511295	-16.722500	23.9	23.9	770	159	
WISPJ1150-2033	PAR199-00124	6	T1	177.704559	-20.565000	23.2	626	21		
GOODSSJ0332-2749	GOODSS-04-G141_17402	13	T3	53.161709	-27.831562	22.6	22.9	453	48	
WISPJ0437-1106	PAR463-00176	4	T3	69.490608	-11.104400	24.3	24.3	816	134	
WISPJ0307-7243	PAR130-00092	12	T4	46.921608	-72.732600	22.7	410	18		
AEGISJ1418+5242	AEGIS-03-G141_17053	21	T4	214.710007	52.716480	22.7	23.1	440	51	
GOODSSJ0332-2741	GOODSS-01-G141_45889	31	T6	53.242542	-27.695446	22.1	22.9	254	51	
WISPJ1232-0033	PAR58-00112	11	T8	188.176712	-0.551850	23.1	144	5		
WISPJ1305-2538	PAR32-00075	11	T9	196.356232	-25.641300	23.1	23.0	22.7	56	12

Table 5. List of pointings searched in this study

Pointing	l	b	G141 Exp (s)	Observation Date	Lim F110	Lim F140	Lim F160
AEGIS-01	96d26m22.7957s	59d29m44.8363s	6618	2011-05-05		23.8	23.7
AEGIS-02	96d22m11.4361s	59d30m03.2299s	5112	2011-05-03		23.5	23.4
AEGIS-03	96d26m09.5835s	59d40m26.0968s	5112	2011-06-13		23.4	23.3
AEGIS-04	96d29m48.3635s	59d36m39.0879s	5012	2011-03-16		23.6	23.4
AEGIS-05	96d29m39.136s	59d39m03.5108s	5112	2011-03-16		23.9	23.8
AEGIS-06	96d21m14.8403s	59d26m16.0626s	5112	2011-10-11		23.7	23.6
AEGIS-07	96d21m23.877s	59d24m09.3001s	5112	2011-10-30		23.7	23.6
AEGIS-08	96d25m54.1875s	59d23m59.1794s	5012	2011-10-24		23.7	23.6
AEGIS-09	96d25m52.9447s	59d35m31.4419s	5112	2011-06-20		23.5	23.4
AEGIS-10	96d25m29.2378s	59d25m56.7607s	5112	2011-10-23		23.7	23.6
AEGIS-12	96d22m19.4975s	59d39m15.5591s	5112	2011-06-18		23.4	23.4
AEGIS-13	96d27m07.2075s	59d36m27.7698s	5112	2011-08-31		24.1	23.9
AEGIS-14	96d26m30.6171s	59d33m15.9555s	5112	2011-06-27		23.4	23.2
AEGIS-15	96d22m22.9309s	59d36m31.0191s	5112	2011-06-21		23.7	23.5
AEGIS-18	96d21m39.6734s	59d37m39.4974s	5112	2011-09-03		23.7	23.6
AEGIS-19	96d29m48.4966s	59d25m36.9587s	5112	2011-10-27		23.7	23.6
AEGIS-21	96d22m04.2749s	59d28m10.0006s	5012	2011-10-28		23.7	23.6
AEGIS-23	96d28m47.1281s	59d31m59.0613s	5112	2011-12-02		23.6	23.5
AEGIS-24	96d27m45.2658s	59d38m29.4777s	5112	2011-09-02		23.9	23.8
AEGIS-25	96d25m23.0474s	59d38m05.6042s	5112	2011-06-20		23.3	23.2
AEGIS-26	96d21m04.5639s	59d22m11.6393s	5112	2011-10-28		23.6	23.5
AEGIS-27	96d29m28.3251s	59d21m43.0347s	5112	2011-10-28		23.6	23.5
AEGIS-28	96d22m35.2627s	59d34m00.8421s	5012	2011-06-27		23.5	23.4
AEGIS-11	96d31m14.5693s	59d29m18.8023s	5112	2011-05-02		23.4	23.5
COSMOS-01	236d34m20.2409s	42d11m45.8981s	4712	2011-04-16		23.1	23.0
COSMOS-03	236d38m59.2639s	42d09m42.5814s	4612	2011-04-06		23.5	23.4

Table 5 continued on next page

Table 5 (*continued*)

Pointing	l	b	G141 Exp (s)	Observation Date	Lim F110	Lim F140	Lim F160
COSMOS-04	236d45m34.3324s	42d13m31.4764s	4712	2011-06-05		23.5	23.4
COSMOS-05	236d43m26.5122s	42d06m56.048s	4712	2011-06-05		23.5	23.3
COSMOS-06	236d45m54.0556s	42d05m47.3817s	4712	2011-06-09		23.3	23.2
COSMOS-07	236d31m49.2007s	42d12m52.8501s	4712	2011-06-09		23.7	23.6
COSMOS-08	236d32m27.3238s	42d15m07.9461s	4612	2011-06-10		23.3	23.2
COSMOS-09	236d43m01.6542s	42d14m31.6546s	4712	2011-06-11		23.6	23.4
COSMOS-10	236d39m41.3114s	42d11m56.3185s	4612	2012-03-09		23.5	23.4
COSMOS-11	236d33m05.7552s	42d17m21.5883s	4712	2011-06-17		23.4	23.3
COSMOS-12	236d44m01.1661s	42d09m08.8201s	4712	2011-06-17		23.5	23.4
COSMOS-13	236d46m29.7279s	42d08m00.2618s	4712	2011-06-12		23.7	23.6
COSMOS-14	236d48m54.611s	42d06m41.8829s	4712	2011-06-12		23.4	23.2
COSMOS-15	236d35m46.9137s	42d16m21.5521s	4512	2010-11-03		23.4	23.3
COSMOS-16	236d38m08.2079s	42d15m12.9157s	4712	2010-10-30		23.5	23.4
COSMOS-17	236d40m24.5941s	42d14m19.9295s	4412	2010-11-03		23.4	23.3
COSMOS-18	236d40m43.7599s	42d15m38.6336s	4712	2011-03-27		23.4	23.3
COSMOS-19	236d50m28.3721s	42d10m34.6583s	4512	2012-03-02		23.5	23.4
COSMOS-20	236d42m52.4314s	42d12m55.7431s	4512	2010-11-03		23.3	23.2
COSMOS-21	236d47m08.6916s	42d10m13.0784s	4712	2011-06-12		23.6	23.5
COSMOS-22	236d48m21.1083s	42d12m13.2377s	4512	2012-03-04		23.7	23.6
COSMOS-23	236d44m46.5672s	42d11m20.6701s	4612	2011-04-07		23.5	23.4
COSMOS-24	236d42m05.8367s	42d10m40.8589s	4512	2010-11-03		23.0	22.9
COSMOS-25	236d37m29.2179s	42d12m57.1516s	4612	2010-12-11		23.2	23.1
COSMOS-26	236d41m19.1745s	42d08m25.8472s	4512	2010-11-03		23.0	22.9
COSMOS-27	236d36m53.985s	42d10m43.5386s	4512	2010-11-03		23.3	23.2
COSMOS-28	236d35m14.0373s	42d14m06.8982s	4512	2010-11-04		23.4	23.3
COSMOS-02	236d49m33.0991s	42d08m53.2557s	4712	2011-05-27		23.4	23.3
UDS-01	169d56m39.106s	-59d54m06.9111s	4712	2011-11-28		23.8	23.7

Table 5 continued on next page

Table 5 (*continued*)

Pointing	l	b	G141 Exp (s)	Observation Date	Lim F110	Lim F140	Lim F160
UDS-02	169d59m35.3003s	-59d55m48.9718s	4712	2011-11-30		23.4	23.3
UDS-03	170d02m31.5858s	-59d57m31.0715s	4712	2011-11-30		23.8	23.7
UDS-04	169d53m35.8828s	-59d55m24.1621s	4712	2011-12-04		23.8	23.7
UDS-05	169d45m19.0766s	-59d56m35.9337s	4612	2011-08-20		24.0	23.9
UDS-06	169d50m22.491s	-59d58m16.764s	4712	2011-08-27		23.8	23.8
UDS-07	169d51m10.577s	-60d00m21.8937s	4712	2012-01-23		23.9	23.8
UDS-08	169d47m19.7632s	-60d00m48.0749s	4712	2012-01-13		24.0	23.9
UDS-09	169d47m48.6102s	-60d03m02.0572s	4712	2012-01-14		24.1	23.9
UDS-10	169d51m44.5632s	-60d02m35.8008s	4712	2012-01-14		24.1	24.0
UDS-11	169d56m31.3347s	-59d57m05.9724s	4712	2011-11-22		24.0	23.9
UDS-12	169d59m27.295s	-59d58m50.2587s	4712	2011-11-24		24.1	24.0
UDS-13	169d46m34.0227s	-59d58m47.1916s	4512	2011-08-27		23.8	23.7
UDS-14	169d56m27.9345s	-60d00m09.8173s	4612	2011-12-01		23.7	23.6
UDS-15	169d42m24.9819s	-60d04m41.9412s	4712	2012-01-20		24.1	23.9
UDS-17	169d53m32.7427s	-59d58m28.4647s	4712	2011-12-21		24.0	23.8
UDS-18	170d06m20.9901s	-59d49m36.8853s	4612	2012-01-28		23.7	23.8
UDS-20	169d36m23.932s	-60d03m09.9533s	4612	2012-01-14		23.9	23.9
UDS-21	169d38m31.9934s	-60d05m07.0527s	4712	2012-01-20		23.9	23.9
UDS-22	169d42m28.4973s	-60d06m33.0776s	4712	2012-01-20		24.2	24.1
UDS-23	169d35m33.8044s	-60d01m15.2368s	4712	2011-08-20		24.0	24.0
UDS-24	169d50m30.1081s	-59d56m42.4416s	4612	2011-12-16		23.9	23.8
UDS-25	169d41m57.2879s	-59d57m58.7204s	4712	2011-08-23		24.1	24.0
UDS-26	169d39m03.4028s	-60d00m10.5448s	4612	2011-08-23		24.1	24.0
UDS-27	169d40m16.1112s	-60d02m24.685s	4612	2011-08-28		23.9	23.8
UDS-28	169d53m32.8421s	-60d01m29.9887s	4712	2011-12-21		24.0	23.9
UDS-16	169d46m16.6063s	-60d04m38.2467s	4712	2012-01-14		24.1	24.1
UDS-19	169d43m09.4875s	-60d00m08.4711s	4612	2011-08-28		24.1	24.0

Table 5 *continued on next page*

Table 5 (*continued*)

Pointing	l	b	G141 Exp (s)	Observation Date	Lim F110	Lim F140	Lim F160
GOODSN-11	126d04m25.445s	54d50m09.1776s	4612	2010-04-15		23.4	23.4
GOODSN-111	126d04m25.445s	54d50m09.1776s	2506	2011-04-19		24.8	24.7
GOODSN-114	125d56m48.3881s	54d46m34.9693s	5012	2011-04-20		23.8	23.7
GOODSN-12	126d01m52.7561s	54d48m57.9318s	3812	2010-04-15		24.3	24.2
GOODSN-13	125d59m20.2713s	54d47m46.4697s	3812	2010-04-15		23.4	23.3
GOODSN-14	125d56m48.3881s	54d46m34.9693s	4312	2010-04-16		23.8	23.7
GOODSN-15	125d54m16.7094s	54d45m23.2533s	5312	2010-04-22		23.4	23.3
GOODSN-16	125d51m45.5105s	54d44m11.5073s	5312	2010-09-25		23.7	23.7
GOODSN-18	125d46m43.7789s	54d41m47.6692s	5312	2010-09-26		23.6	23.5
GOODSN-23	125d56m58.7504s	54d49m26.6386s	4512	2010-04-17		23.6	23.5
GOODSN-24	125d54m26.6825s	54d48m14.9297s	4612	2010-04-17		23.4	23.3
GOODSN-25	125d51m54.9752s	54d47m03.1973s	5312	2010-04-22		23.7	23.5
GOODSN-26	125d49m23.6108s	54d45m51.3422s	5312	2010-09-21		23.3	23.2
GOODSN-27	125d46m52.5728s	54d44m39.2654s	5312	2009-09-16		24.0	23.9
GOODSN-28	125d44m21.8943s	54d43m27.1663s	5212	2009-09-16		23.4	23.4
GOODSN-31	125d59m41.8598s	54d53m29.7889s	4512	2010-04-18		23.6	23.5
GOODSN-32	125d57m08.9541s	54d52m18.3172s	5112	2010-04-18		23.5	23.4
GOODSN-34	125d52m04.3999s	54d49m54.8893s	5312	2010-04-20		23.4	23.3
GOODSN-35	125d49m32.7678s	54d48m43.0338s	5312	2009-09-25		23.2	23.1
GOODSN-36	125d47m01.3421s	54d47m30.9631s	5112	2010-04-23		23.5	23.4
GOODSN-41	125d57m19.3625s	54d55m09.9839s	5312	2010-03-07		23.7	23.6
GOODSN-42	125d54m46.3923s	54d53m58.2959s	5312	2010-04-19		23.8	23.7
GOODSN-43	125d52m14.0268s	54d52m46.5699s	5312	2010-04-21		23.6	23.5
GOODSN-44	125d49m41.7634s	54d51m34.7343s	5112	2010-04-21		23.3	23.2
GOODSN-45	125d47m10.0701s	54d50m22.6629s	5312	2010-04-09		23.5	23.5
GOODSN-46	125d44m38.496s	54d49m10.5819s	5312	2010-04-23		23.2	23.2
GOODSS-01	223d24m10.3726s	-54d17m46.6259s	4712	2011-11-27		23.5	23.4

Table 5 continued on next page

Table 5 (*continued*)

Pointing	l	b	G141 Exp (s)	Observation Date	Lim F110	Lim F140	Lim F160
GOODSS-02	223d33m36.5207s	-54d28m54.8594s	4712	2011-10-18	23.5	23.4	
GOODSS-03	223d22m30.2755s	-54d23m16.2548s	4712	2011-10-13	23.3	23.2	
GOODSS-04	223d38m20.6751s	-54d24m26.6376s	4712	2012-03-22	23.5	23.4	
GOODSS-05	223d43m50.911s	-54d28m38.6367s	4712	2012-03-20	23.5	23.4	
GOODSS-06	223d40m53.9592s	-54d21m45.7524s	4712	2011-03-23	23.7	23.7	
GOODSS-08	223d34m42.8975s	-54d22m12.619s	4712	2011-10-13	23.5	23.4	
GOODSS-09	223d30m02.966s	-54d28m35.0602s	4712	2012-01-22	23.5	23.4	
GOODSS-10	223d39m12.9866s	-54d26m40.1329s	4612	2012-03-21	23.7	23.7	
GOODSS-11	223d24m54.1865s	-54d23m40.386s	4712	2012-01-22	23.4	23.3	
GOODSS-12	223d26m17.3983s	-54d28m03.6025s	4712	2012-01-22	23.6	23.5	
GOODSS-13	223d42m36.1571s	-54d26m11.6958s	4712	2012-03-21	23.6	23.5	
GOODSS-14	223d45m09.5167s	-54d23m29.8534s	4712	2012-03-22	23.7	23.6	
GOODSS-15	223d46m54.4452s	-54d27m55.458s	4712	2012-03-21	24.0	24.0	
GOODSS-16	223d46m01.4244s	-54d25m42.4359s	4712	2012-03-22	23.5	23.4	
GOODSS-17	223d29m32.2206s	-54d26m25.2381s	4712	2012-01-28	23.7	23.6	
GOODSS-18	223d31m12.1782s	-54d21m58.6349s	4712	2011-09-30	23.5	23.4	
GOODSS-19	223d37m06.6053s	-54d29m03.4224s	4712	2011-10-16	23.4	23.2	
GOODSS-20	223d36m27.3672s	-54d26m45.8557s	4712	2011-10-20	23.5	23.4	
GOODSS-21	223d41m44.0431s	-54d23m59.0473s	4712	2012-03-22	23.5	23.4	
GOODSS-22	223d44m18.9127s	-54d21m17.899s	4712	2012-03-22	23.6	23.7	
GOODSS-24	223d27m56.614s	-54d30m00.1967s	4512	2011-06-02	23.3	23.2	
GOODSS-25	223d32m00.3355s	-54d30m05.9971s	4712	2011-12-04	23.5	23.4	
GOODSS-26	223d40m10.3543s	-54d28m21.5254s	4712	2011-06-22	23.4	23.3	
GOODSS-27	223d37m30.1933s	-54d22m14.0921s	4712	2011-04-04	23.7	23.6	
GOODSS-28	223d41m27.817s	-54d18m29.8464s	4712	2011-02-15	23.1	23.1	
GOODSS-29	223d27m51.4148s	-54d21m59.0649s	4712	2012-01-24	23.5	23.4	
GOODSS-30	223d25m45.9696s	-54d25m53.5297s	4612	2012-01-30	23.3	23.2	

Table 5 continued on next page

Table 5 (*continued*)

Pointing	l	b	G141 Exp (s)	Observation Date	Lim F110	Lim F140	Lim F160
GOODSS-31	223d32m56.7649s	-54d26m36.3236s	4712	2011-10-24		23.7	23.5
GOODSS-32	223d32m03.2433s	-54d24m17.59s	4712	2011-10-19		23.4	23.3
GOODSS-33	223d28m40.4044s	-54d24m11.7319s	4712	2012-01-29		23.6	23.5
GOODSS-34	223d32m17.6862s	-54d23m37.6375s	4712	2011-08-21		23.6	23.5
GOODSS-35	223d23m20.0732s	-54d25m34.7626s	4712	2011-10-20		23.6	23.4
GOODSS-36	223d32m12.6925s	-54d23m27.1715s	4612	2011-08-22		23.6	23.5
GOODSS-37	223d32m27.7173s	-54d23m41.5538s	4612	2011-08-24		23.4	23.2
GOODSS-38	223d32m28.113s	-54d23m31.2004s	4712	2011-08-29		23.8	23.7
GOODSN-17	125d49m14.4136s	54d42m59.6527s	5212	2009-09-23		23.7	23.5
GOODSN-21	126d02m03.881s	54d51m49.4868s	3912	2010-04-16		23.2	23.1
GOODSN-22	125d59m31.1441s	54d50m38.1246s	4212	2010-04-16		23.5	23.5
GOODSN-33	125d54m36.6173s	54d51m06.6083s	5212	2010-04-19		23.6	23.5
GOODSS-07	223d35m17.0277s	-54d24m32.5701s	4712	2011-10-13		23.6	23.5
GOODSN-123	125d56m58.7504s	54d49m26.6386s	4812	2011-04-22		23.6	23.5
WISPS-334	248d01m37.1871s	51d34m40.522s	2409	2014-04-09	23.4		23.1
WISPS-1	128d21m15.0574s	-47d33m50.0238s	2609	2009-11-24	22.4	21.3	21.3
WISPS-10	169d37m01.1985s	44d59m58.1595s	2209	2010-01-02	22.4	22.1	22.0
WISPS-101	337d40m43.7467s	62d06m39.7407s	4112	2011-03-11			22.2
WISPS-103	140d28m45.8345s	27d52m16.1255s	3009	2011-03-19			22.2
WISPS-104	238d34m58.5529s	42d42m14.9265s	7218	2011-03-13	23.6		23.4
WISPS-105	340d47m35.3546s	26d43m02.8523s	4112	2011-04-09			22.0
WISPS-106	167d21m48.1265s	66d46m38.0512s	2006	2011-04-25			21.8
WISPS-107	107d57m44.8793s	69d25m24.3327s	4615	2011-04-26		22.6	
WISPS-108	161d33m40.7812s	76d56m49.2195s	4515	2011-04-27			22.3
WISPS-11	239d56m49.3962s	59d38m54.7978s	2006	2010-01-03	22.0	22.0	21.6
WISPS-110	121d10m48.8118s	62d35m18.5169s	3309	2011-05-09			22.2
WISPS-111	348d18m17.7931s	-65d17m53.2129s	2206	2011-05-10			22.1

Table 5 continued on next page

Table 5 (*continued*)

Pointing	l	b	G141 Exp (s)	Observation Date	Lim F110	Lim F140	Lim F160
WISPS-114	241d05m37.2252s	52d33m39.8043s	2909	2011-05-27	23.7		22.8
WISPS-115	257d16m00.4351s	56d43m06.3875s	2106	2011-05-28	24.1		23.2
WISPS-116	232d30m58.4278s	57d39m38.6771s	5215	2011-05-30			22.5
WISPS-119	209d10m36.4938s	69d04m21.8025s	4515	2011-06-02			22.4
WISPS-12	144d21m59.7364s	69d37m03.6496s	3009	2010-01-04	22.5	22.9	22.2
WISPS-120	2d36m26.7952s	71d49m34.8193s	1806	2011-06-10	22.5		22.2
WISPS-121	284d59m39.4219s	47d11m07.5533s	1806	2011-07-25	22.1		21.8
WISPS-122	95d15m56.1391s	48d37m33.8597s	2809	2011-06-12			22.1
WISPS-123	39d55m47.9629s	63d31m29.2718s	4515	2011-06-18			22.4
WISPS-124	82d39m09.492s	24d16m52.9963s	1906	2011-06-21	22.8		22.6
WISPS-125	96d13m19.4386s	34d09m46.3115s	2909	2011-06-22			22.3
WISPS-126	333d40m29.5448s	64d53m13.6619s	3612	2011-06-27			22.0
WISPS-127	291d43m26.9965s	-42d25m04.5331s	2006	2011-06-29			21.8
WISPS-128	227d02m34.5156s	-82d55m04.0317s	4815	2011-06-29			22.4
WISPS-129	221d07m16.59s	64d21m38.2839s	2206	2011-06-30	22.8		22.2
WISPS-13	128d22m32.9706s	-47d34m13.0982s	2409	2010-01-09	22.3	22.1	21.8
WISPS-130	290d14m27.2003s	-40d51m26.9849s	2006	2011-06-30			21.7
WISPS-132	264d09m11.6865s	54d36m40.0913s	1806	2011-07-03	22.9		22.4
WISPS-133	349d02m56.2243s	-46d22m41.0644s	2406	2011-07-10			22.0
WISPS-134	326d12m55.1256s	-24d50m39.1408s	2506	2011-07-14			22.1
WISPS-135	143d47m35.1047s	55d31m30.3336s	1906	2011-07-15	23.0		22.6
WISPS-136	286d32m14.9124s	67d27m29.0153s	7318	2011-07-15	23.6		23.3
WISPS-137	51d01m10.2903s	35d43m35.1234s	2509	2011-07-18			22.1
WISPS-138	18d14m24.8476s	45d24m14.9623s	4515	2011-07-19			22.0
WISPS-139	359d54m20.0031s	75d33m37.9s	4515	2011-07-22			22.5
WISPS-14	174d30m24.7964s	-56d14m37.0116s	2809	2010-01-09	22.4	22.7	21.3
WISPS-140	335d48m49.9238s	59d30m11.0296s	4112	2011-07-26			21.9

Table 5 *continued on next page*

Table 5 (*continued*)

Pointing	l	b	G141 Exp (s)	Observation Date	Lim F110	Lim F140	Lim F160
WISPS-141	18d14m21.6844s	59d31m51.0118s	2709	2011-07-27			22.1
WISPS-143	350d13m13.22s	65d53m21.5411s	3109	2011-08-06	23.4		22.7
WISPS-144	308d26m59.178s	52d07m57.9138s	2309	2011-08-16			21.1
WISPS-145	172d58m06.4623s	-67d10m49.8642s	2406	2011-08-17			22.1
WISPS-146	171d05m25.005s	-62d34m04.7433s	1806	2011-08-21	22.6		22.4
WISPS-147	83d51m12.4292s	-68d59m23.8183s	2106	2011-08-23	23.2		22.5
WISPS-148	42d38m20.9726s	46d49m45.7815s	4615	2011-09-01			22.0
WISPS-149	180d30m14.8975s	-24d13m45.8153s	3812	2011-09-16			21.9
WISPS-15	34d53m40.9433s	72d31m37.58s	2609	2010-02-12	23.7	23.6	21.8
WISPS-150	175d18m58.8179s	-23d36m11.3898s	3812	2011-09-16			21.6
WISPS-151	44d17m15.0997s	55d23m22.0092s	3712	2011-09-17			22.0
WISPS-152	49d56m57.7973s	63d18m34.6899s	4212	2011-09-23			22.4
WISPS-153	106d56m21.7529s	-21d01m29.1953s	4212	2011-09-25			22.3
WISPS-154	97d01m18.0033s	42d53m03.5092s	2809	2011-10-05			22.0
WISPS-155	91d10m28.0679s	36d25m07.6444s	2809	2011-10-05			21.9
WISPS-156	87d13m51.2822s	42d01m48.9903s	2809	2011-10-17			22.1
WISPS-157	93d29m41.8327s	52d03m46.6439s	2809	2011-10-19			22.2
WISPS-158	90d44m55.8226s	47d51m18.3292s	2809	2011-10-19			21.8
WISPS-159	43d39m21.9361s	-29d53m50.9123s	4012	2011-10-20			21.9
WISPS-16	174d29m20.313s	-56d14m44.9874s	2509	2010-02-16	22.3	20.9	20.3
WISPS-160	89d27m49.4896s	54d42m22.8911s	2709	2011-10-21			22.2
WISPS-161	81d15m40.5606s	45d13m42.0826s	3309	2011-10-21			22.2
WISPS-162	60d54m08.5451s	37d30m29.5894s	653	2011-10-29			21.1
WISPS-163	181d19m07.9237s	56d54m22.594s	703	2011-10-29			21.2
WISPS-165	92d43m44.8306s	-35d29m35.3573s	1906	2011-11-02			21.9
WISPS-166	92d45m22.9256s	-35d29m18.7975s	1906	2011-11-02			21.5
WISPS-167	141d03m09.7294s	-47d28m47.8637s	1806	2011-11-07	22.8		22.2

Table 5 *continued on next page*

Table 5 (*continued*)

Pointing	l	b	G141 Exp (s)	Observation Date	Lim F110	Lim F140	Lim F160
WISPS-168	131d59m21.0999s	-20d34m48.2153s	1406	2011-11-09		21.8	
WISPS-169	278d08m56.1591s	24d51m06.9246s	2509	2011-11-09		21.7	
WISPS-17	152d00m55.68s	-45d15m47.0239s	3409	2010-02-18	22.4	21.5	22.2
WISPS-170	265d21m44.3806s	20d43m46.1929s	2206	2011-11-20		21.7	
WISPS-171	265d21m44.3806s	20d43m46.1929s	2206	2011-11-20		21.7	
WISPS-172	15d39m27.0251s	-29d19m02.7019s	1406	2011-11-28		21.2	
WISPS-173	165d49m21.7985s	-66d25m31.4953s	4515	2011-12-04		22.2	
WISPS-174	86d49m10.3985s	49d19m35.3457s	2709	2011-12-18		22.3	
WISPS-175	212d49m28.2952s	-50d34m22.6997s	1906	2012-01-06		22.3	
WISPS-176	212d45m26.3898s	-50d33m10.9251s	1906	2012-01-06		22.5	
WISPS-177	280d14m28.0841s	45d56m06.165s	903	2012-01-06		21.6	
WISPS-179	261d05m54.3s	31d58m12.9997s	1606	2012-01-21		21.6	
WISPS-18	284d14m07.5396s	72d47m46.5254s	3918	2010-02-19	22.8	21.9	22.5
WISPS-181	218d51m04.5556s	86d38m00.5214s	1806	2012-01-29	22.2		22.1
WISPS-182	100d40m32.2556s	-33d47m19.3217s	1203	2012-01-29		21.2	
WISPS-183	212d27m09.1675s	72d56m43.005s	1806	2012-02-01	22.8		22.3
WISPS-186	82d03m12.8489s	79d49m48.4413s	703	2012-02-15		21.2	
WISPS-188	202d59m50.3396s	23d53m47.6013s	1606	2012-02-23		21.5	
WISPS-189	192d44m35.1182s	-20d11m13.6786s	2309	2012-02-26		21.9	
WISPS-19	174d29m06.2462s	-56d14m46.1583s	2809	2010-02-20	22.3	21.4	21.8
WISPS-190	248d03m19.6943s	-41d27m17.1088s	1206	2012-03-11		22.1	
WISPS-191	200d04m14.6013s	53d06m56.5437s	2509	2012-03-11		21.7	
WISPS-192	188d42m58.1646s	50d54m14.5878s	1406	2012-03-18		21.8	
WISPS-193	151d29m37.7767s	48d12m30.6226s	803	2012-04-03		21.3	
WISPS-194	221d59m58.5269s	-34d44m24.5841s	653	2012-04-04		21.1	
WISPS-195	110d33m48.3142s	63d26m03.7236s	803	2012-04-05		21.9	
WISPS-196	239d47m23.7223s	68d19m26.324s	1406	2012-04-07		21.7	

Table 5 *continued on next page*

Table 5 (*continued*)

Pointing	l	b	G141 Exp (s)	Observation Date	Lim F110	Lim F140	Lim F160
WISPS-197	24d57m38.343s	-32d17m10.7193s	803	2012-04-08		20.9	
WISPS-198	299d36m32.078s	-65d54m42.6822s	903	2012-04-10		21.3	
WISPS-199	284d16m41.1946s	40d06m13.6428s	1003	2012-04-19		21.7	
WISPS-2	133d15m48.4472s	-40d32m25.203s	1906	2009-12-12	22.0	21.2	21.6
WISPS-20	34d54m36.769s	72d31m57.4805s	2812	2010-02-21	23.5	22.2	
WISPS-200	239d18m09.5265s	53d53m12.5349s	1606	2012-04-20		21.8	
WISPS-201	202d59m09.8488s	56d25m25.6905s	653	2012-04-20		21.1	
WISPS-202	255d28m33.0203s	56d17m21.0267s	1406	2012-04-24		21.8	
WISPS-203	78d31m36.2082s	-24d41m34.0807s	803	2012-04-24		21.0	
WISPS-204	255d17m46.6094s	58d17m37.806s	1606	2012-04-27		21.7	
WISPS-205	299d37m51.4683s	22d56m14.0725s	803	2012-04-28		21.2	
WISPS-206	269d43m59.7841s	25d22m39.4473s	1003	2012-05-06		21.6	
WISPS-209	327d59m48.9054s	60d27m03.8566s	803	2012-05-18		21.5	
WISPS-21	154d06m26.7606s	42d20m50.023s	2006	2010-03-05		22.8	
WISPS-210	290d19m13.0785s	74d26m26.5068s	653	2012-05-19		21.3	
WISPS-211	193d08m58.5433s	82d44m06.9122s	653	2012-05-20		21.6	
WISPS-212	144d51m41.0893s	69d34m41.8715s	1806	2012-05-20		21.9	
WISPS-214	187d10m06.3456s	54d09m52.6955s	703	2012-06-19		21.1	
WISPS-215	190d29m28.588s	57d02m57.4169s	653	2012-06-19		21.1	
WISPS-216	293d01m16.8512s	60d02m20.1614s	1103	2012-06-19		21.3	
WISPS-217	175d26m58.0091s	87d08m46.4057s	1606	2012-06-22		21.6	
WISPS-218	36d47m32.1902s	68d39m40.852s	703	2012-06-23		21.1	
WISPS-219	210d39m20.5767s	74d29m03.5823s	703	2012-06-23		20.8	
WISPS-22	224d47m22.5184s	28d16m51.5388s	1806	2010-03-05		22.4	
WISPS-220	245d06m55.0491s	66d58m53.4354s	703	2012-06-24		21.3	
WISPS-221	350d38m23.0977s	55d49m55.5438s	1706	2012-06-27		21.7	
WISPS-222	46d43m43.2053s	72d29m57.0152s	1906	2012-06-28		21.9	

Table 5 *continued on next page*

Table 5 (*continued*)

Pointing	l	b	G141 Exp (s)	Observation Date	Lim F110	Lim F140	Lim F160
WISPS-224	136d55m02.3926s	72d17m49.975s	1206	2012-07-04		21.9	
WISPS-226	136d56m03.9679s	72d17m55.2971s	803	2012-07-07		22.0	
WISPS-227	136d55m02.3926s	72d17m49.975s	1206	2012-07-11		21.9	
WISPS-228	123d44m20.0898s	34d29m21.5171s	1706	2012-07-15		21.7	
WISPS-229	294d55m53.4458s	-57d52m43.1983s	1206	2012-07-18		21.5	
WISPS-23	230d04m06.5448s	40d19m31.2837s	4115	2010-03-06		19.4	
WISPS-231	129d56m43.446s	-60d26m30.4506s	1706	2012-07-19		22.6	
WISPS-232	293d13m14.0338s	-80d56m40.9514s	1406	2012-07-20		21.9	
WISPS-233	139d02m33.7352s	70d25m02.4052s	603	2012-07-28		21.0	
WISPS-234	345d50m36.7836s	-58d27m14.7313s	2006	2012-07-28		22.6	
WISPS-235	1d40m08.5156s	47d36m05.6478s	1406	2012-07-30		21.7	
WISPS-236	3d25m29.8479s	44d31m55.0273s	1609	2012-06-10		21.8	
WISPS-237	123d46m11.9635s	77d19m58.473s	1806	2012-08-01		21.8	
WISPS-238	122d56m44.2357s	70d34m36.7083s	1303	2012-08-04		22.0	
WISPS-239	26d05m16.942s	23d40m07.2384s	703	2012-08-04		21.4	
WISPS-24	190d04m01.7752s	82d18m03.7607s	1806	2010-03-21		19.6	
WISPS-240	27d43m45.609s	43d27m18.3994s	2106	2012-08-05		22.0	
WISPS-241	191d32m15.5142s	-23d01m28.7155s	703	2012-08-08		21.1	
WISPS-242	150d48m20.3257s	-54d31m45.4858s	1206	2012-08-13		21.7	
WISPS-243	26d03m56.247s	77d04m12.2577s	1606	2012-08-24		21.8	
WISPS-244	304d54m19.741s	-37d03m35.6467s	803	2012-09-09		21.5	
WISPS-245	160d08m18.659s	47d08m06.0442s	803	2012-09-13		21.0	
WISPS-246	157d51m49.3158s	47d57m15.0682s	1906	2012-09-14		22.1	
WISPS-247	120d03m00.8711s	-75d39m27.9399s	1103	2012-09-17		21.3	
WISPS-248	39d34m58.8552s	-27d17m03.1403s	1906	2012-09-23		21.8	
WISPS-249	305d28m36.3929s	-42d41m46.6499s	703	2012-09-23		22.4	
WISPS-25	232d38m43.401s	46d36m21.9884s	4115	2010-03-29	22.6	22.2	22.3

Table 5 continued on next page

Table 5 (*continued*)

Pointing	l	b	G141 Exp (s)	Observation Date	Lim F110	Lim F140	Lim F160
WISPS-250	150d39m12.8668s	35d43m59.8832s	1406	2012-09-25		21.4	
WISPS-251	189d29m46.0432s	-28d57m14.2944s	803	2012-10-01		21.4	
WISPS-252	189d30m19.7944s	-29d00m06.7566s	803	2012-10-01		20.9	
WISPS-256	200d50m43.0134s	68d25m26.4439s	1706	2012-10-17	21.9		21.6
WISPS-257	227d31m08.3971s	-64d37m01.9404s	3512	2012-10-17	23.2		22.9
WISPS-258	244d54m49.8005s	-66d19m23.5286s	2309	2012-11-02	22.6		22.3
WISPS-259	197d05m10.1345s	74d36m11.2377s	1706	2012-11-06		21.6	
WISPS-26	202d41m08.1345s	34d37m45.2722s	2209	2010-04-01	22.8	21.9	22.5
WISPS-260	320d39m39.5995s	-65d18m58.6253s	2909	2012-11-07	23.4		23.0
WISPS-261	96d11m39.2815s	-67d40m17.4024s	2309	2012-11-10	23.0		22.5
WISPS-262	237d14m11.5197s	60d00m19.3047s	1406	2012-11-11		21.3	
WISPS-263	69d50m07.0953s	-28d11m05.5678s	603	2012-11-12		20.7	
WISPS-264	239d47m23.7358s	59d21m35.2024s	1606	2012-11-15		21.5	
WISPS-267	193d55m27.5541s	47d41m22.1238s	1406	2012-11-21		21.2	
WISPS-268	185d07m48.823s	20d52m44.3029s	1303	2012-11-22		20.8	
WISPS-269	181d53m58.5933s	-57d59m11.6114s	653	2012-11-29		21.4	
WISPS-27	261d11m28.5319s	59d49m49.9219s	2206	2010-04-02	21.6	21.8	21.3
WISPS-270	298d57m14.3776s	65d06m28.9483s	1506	2012-12-01	22.0		21.6
WISPS-271	210d22m21.5669s	39d00m33.0933s	1506	2012-12-02	22.5		22.1
WISPS-272	181d53m34.9726s	-57d58m56.5142s	1103	2012-12-06		22.0	
WISPS-273	164d16m05.7071s	-54d57m12.6234s	1003	2012-12-15		21.7	
WISPS-275	147d08m55.6188s	-45d57m11.6791s	1406	2012-12-18		21.7	
WISPS-277	193d40m13.896s	53d20m41.0186s	1406	2013-01-08		21.7	
WISPS-279	345d49m07.5754s	55d04m31.3743s	1906	2013-01-25		21.5	
WISPS-28	218d14m40.0482s	42d51m36.5265s	3515	2010-04-02	22.6	21.8	22.4
WISPS-281	186d04m00.5935s	-55d18m16.7816s	803	2013-01-27		21.7	
WISPS-288	227d20m43.4831s	40d09m33.9684s	1706	2013-02-22	22.0		21.6

Table 5 *continued on next page*

Table 5 (*continued*)

Pointing	l	b	G141 Exp (s)	Observation Date	Lim F110	Lim F140	Lim F160
WISPS-289	293d02m41.1787s	80d09m50.7787s	2206	2013-02-25		21.9	
WISPS-29	143d57m46.4309s	67d00m46.0505s	1906	2010-04-09	22.3	21.6	22.0
WISPS-290	21d09m35.6644s	46d35m16.9432s	1706	2013-02-25		21.6	
WISPS-292	32d38m22.9535s	67d23m32.4342s	703	2013-03-08		21.4	
WISPS-293	253d51m54.1763s	24d54m10.3794s	1203	2013-03-11		21.6	
WISPS-294	304d28m01.1536s	29d38m12.0766s	1706	2013-03-16	23.0		22.5
WISPS-295	283d52m00.0001s	72d47m27.007s	1706	2013-03-23	22.3		22.1
WISPS-297	264d40m13.4694s	59d00m39.927s	1706	2013-04-11	22.7		22.4
WISPS-299	171d23m14.7388s	43d25m29.2291s	5615	2013-05-05	23.3		22.7
WISPS-30	181d26m20.7418s	57d56m49.0383s	1806	2010-04-21	21.8	22.0	21.5
WISPS-300	175d47m15.3943s	39d23m56.8053s	2709	2013-05-12	22.8		22.5
WISPS-301	33d52m47.993s	69d58m11.0161s	803	2013-05-19		21.6	
WISPS-302	226d20m46.5698s	-64d59m03.7871s	3012	2013-05-27	22.9		22.6
WISPS-303	33d36m02.1452s	77d15m58.0255s	2809	2013-06-02	23.1		22.8
WISPS-304	94d10m25.2173s	58d40m38.3751s	5215	2013-05-29	23.9		23.3
WISPS-307	13d08m10.5712s	-78d06m11.7184s	3012	2013-06-15	23.5		22.6
WISPS-308	35d12m53.8258s	47d34m52.5536s	803	2013-06-21	22.4		22.1
WISPS-309	4d35m42.4947s	-48d32m11.0014s	2209	2013-06-25	23.3		22.6
WISPS-31	198d36m57.5975s	35d12m44.2693s	4412	2010-04-21	22.4	22.4	22.1
WISPS-311	88d42m04.7459s	44d48m55.6229s	3009	2013-07-20	23.2		22.8
WISPS-312	226d24m09.2188s	-64d30m51.8404s	2309	2013-08-09	22.6		22.3
WISPS-313	227d34m11.7937s	-64d11m17.4168s	2809	2013-08-11	23.5		22.9
WISPS-314	24d19m40.2884s	71d41m25.532s	6621	2013-08-13	23.5		23.1
WISPS-315	313d09m50.6072s	-44d50m48.5682s	2409	2013-08-20	23.0		22.7
WISPS-317	156d08m45.3535s	-69d00m32.9386s	1706	2013-09-13	22.4		22.1
WISPS-319	177d01m17.8023s	40d00m57.4424s	3309	2013-10-30	22.9		22.5
WISPS-32	306d51m50.7528s	37d07m50.4335s	3512	2010-05-13	22.1	22.1	21.8

Table 5 continued on next page

Table 5 (*continued*)

Pointing	l	b	G141 Exp (s)	Observation Date	Lim F110	Lim F140	Lim F160
WISPS-320	200d27m35.0953s	20d31m48.0962s	5115	2013-12-06	24.1		23.5
WISPS-321	210d30m48.1403s	-21d01m58.0684s	4915	2013-11-28	23.6		23.2
WISPS-322	212d08m12.6142s	30d51m31.321s	2509	2013-12-09	23.0		22.7
WISPS-324	152d52m45.4658s	-28d35m33.022s	4915	2013-12-18	23.3		22.9
WISPS-325	302d42m32.0182s	39d20m22.2696s	3612	2013-12-21	22.9		22.5
WISPS-326	210d17m50.7267s	-21d26m30.3808s	4315	2014-02-18	23.6		23.2
WISPS-328	166d26m55.0713s	54d39m30.1657s	2609	2014-03-13	22.4		22.1
WISPS-330	186d20m13.1358s	53d49m50.3956s	2709	2014-03-17	23.3		22.8
WISPS-332	11d25m47.6208s	-31d58m17.5188s	2709	2014-04-02	22.7		22.4
WISPS-333	226d17m34.8224s	48d56m21.4803s	6518	2014-04-05	23.8		23.2
WISPS-335	34d01m56.8344s	49d29m06.5561s	3812	2014-04-11	23.9		23.3
WISPS-336	261d14m10.9059s	24d45m35.0511s	2709	2014-04-13	23.2		23.0
WISPS-337	248d02m22.22s	56d04m37.5775s	2409	2014-04-14	22.9		22.5
WISPS-338	239d52m14.6116s	75d03m24.8336s	2309	2014-04-15	22.8		22.4
WISPS-34	232d22m16.5768s	36d45m00.1444s	4215	2010-05-19	21.9	22.3	21.7
WISPS-340	111d36m35.9388s	84d32m53.085s	2909	2014-05-01	23.0		22.6
WISPS-341	208d54m35.7326s	52d45m36.3077s	2309	2014-03-20	22.6		22.3
WISPS-342	40d39m30.283s	-40d57m59.2649s	2709	2014-05-13	23.0		22.5
WISPS-343	228d48m55.2626s	47d52m42.2671s	2309	2014-05-15	22.4		22.2
WISPS-345	351d46m53.3333s	60d20m46.3883s	3209	2014-05-29	23.2		22.9
WISPS-346	29d43m23.746s	68d12m56.5332s	2709	2014-05-31	22.8		22.5
WISPS-347	239d22m44.0819s	47d52m15.3813s	4412	2014-06-03	23.1		22.7
WISPS-348	51d55m44.9997s	87d45m02.8268s	1806	2014-06-04	23.1		22.8
WISPS-349	260d21m48.0329s	25d45m44.8284s	2409	2014-06-05	23.0		22.5
WISPS-35	79d07m23.7057s	86d08m01.8116s	3812	2010-05-21	22.9	22.5	22.6
WISPS-350	71d49m11.0757s	73d59m44.1828s	2309	2014-06-14	23.3		22.9
WISPS-352	267d31m26.9512s	52d40m49.582s	2709	2014-06-01	22.9		22.5

Table 5 continued on next page

Table 5 (*continued*)

Pointing	l	b	G141 Exp (s)	Observation Date	Lim F110	Lim F140	Lim F160
WISPS-353	103d35m25.7623s	57d12m17.4834s	2709	2014-06-28	22.6		22.2
WISPS-354	86d13m08.6916s	-38d08m59.8513s	2709	2014-07-06	23.5		23.2
WISPS-355	350d17m34.003s	-67d40m05.1254s	2609	2014-07-07	23.7		23.2
WISPS-356	339d37m08.5376s	-69d25m58.0458s	3009	2014-07-10	24.4		23.6
WISPS-357	289d52m13.8166s	68d24m24.9566s	3712	2014-05-31	23.2		22.7
WISPS-358	335d56m20.5676s	-69d39m32.2209s	4312	2014-07-08	23.1		22.8
WISPS-359	0d37m50.4659s	-71d42m42.2342s	2309	2014-07-13	22.8		22.5
WISPS-36	90d49m13.748s	72d32m32.6482s	2809	2010-05-27	23.4	23.4	23.1
WISPS-360	347d26m35.2091s	55d08m28.3092s	3109	2014-07-30	22.7		22.3
WISPS-361	4d05m41.7452s	72d54m49.31s	2709	2014-07-31	22.7		22.4
WISPS-362	89d01m18.0985s	85d06m25.0798s	2809	2014-08-09	22.7		22.4
WISPS-364	205d26m40.221s	-46d14m15.6529s	2709	2014-08-20	23.0		22.7
WISPS-365	141d10m36.1029s	-61d40m08.0345s	8123	2014-08-23	5.6		23.6
WISPS-367	2d36m57.6685s	50d17m17.9157s	2509	2014-08-29	22.5		22.3
WISPS-368	5d21m23.0419s	-69d30m24.6956s	2809	2014-08-29	23.3		22.9
WISPS-369	38d16m39.2835s	-43d20m45.4203s	3612	2014-09-03	23.2		22.9
WISPS-37	90d49m13.748s	72d32m32.6482s	2809	2010-05-30	23.1	23.0	22.8
WISPS-370	3d25m52.0175s	28d29m05.8585s	2709	2014-09-03	23.2		22.8
WISPS-371	358d37m35.269s	-30d59m38.3471s	2509	2014-09-06	23.0		22.8
WISPS-372	309d03m48.5634s	-35d26m33.2661s	5112	2014-08-25	23.8		23.4
WISPS-374	65d08m15.1787s	-64d52m12.6691s	5815	2014-10-26	25.2		9.2
WISPS-375	265d41m59.4804s	23d40m35.617s	2709	2014-11-23	23.8		23.3
WISPS-377	94d18m00.0754s	36d06m57.3593s	2709	2014-12-01	23.5		22.9
WISPS-378	52d50m08.1551s	68d08m42.9162s	2609	2014-12-08	22.5		22.2
WISPS-38	289d59m36.9996s	59d23m33.2791s	4312	2010-05-31	22.8	22.7	22.5
WISPS-380	229d05m48.0735s	58d59m57.4851s	2006	2014-12-21	23.0		22.7
WISPS-381	205d05m58.4209s	-44d32m53.6941s	2309	2015-01-05	23.2		22.7

Table 5 continued on next page

Table 5 (*continued*)

Pointing	l	b	G141 Exp (s)	Observation Date	Lim F110	Lim F140	Lim F160
WISPS-382	72d13m09.2013s	31d16m15.3992s	4915	2015-01-13	23.6		23.3
WISPS-385	32d39m11.827s	67d25m44.5151s	2709	2015-03-29	23.4		23.1
WISPS-386	357d38m41.2383s	54d07m13.1932s	2709	2015-06-14	23.1		22.7
WISPS-387	199d40m25.9927s	42d54m31.6677s	2309	2015-11-30		22.6	
WISPS-388	232d36m11.8501s	57d50m06.5625s	2809	2015-12-01		22.4	
WISPS-389	195d20m38.7511s	82d26m41.4987s	3012	2015-12-05		23.0	
WISPS-39	198d29m12.386s	54d32m25.3887s	1706	2010-06-04	21.4	21.5	21.1
WISPS-391	69d50m56.3952s	60d00m12.6597s	4112	2015-12-21	24.2		23.5
WISPS-394	80d53m13.3786s	51d22m17.5987s	4712	2015-12-24		22.9	
WISPS-395	298d33m00.779s	80d32m28.4007s	2509	2016-01-08	22.4		21.9
WISPS-396	113d04m30.9197s	-46d37m26.8218s	1806	2016-01-17	22.2		21.7
WISPS-397	284d45m37.1934s	74d14m57.4674s	2809	2016-01-24	23.5		23.3
WISPS-398	74d24m47.3271s	34d44m34.5395s	2809	2016-02-08	23.5		23.1
WISPS-40	252d16m08.6767s	-68d40m54.1628s	4112	2010-06-04	22.7	22.5	21.8
WISPS-400	141d15m57.292s	-41d51m52.0463s	2409	2016-02-15	22.9		22.5
WISPS-403	24d09m40.372s	84d40m57.5136s	1806	2016-03-08	22.4		22.0
WISPS-404	316d47m10.1292s	-40d45m34.7176s	4012	2016-03-13	24.3		23.4
WISPS-405	194d13m24.4505s	82d27m14.4826s	3012	2016-03-10	23.1		22.7
WISPS-406	246d14m58.365s	39d48m43.7572s	3109	2016-03-13	23.7		23.2
WISPS-408	246d08m42.0093s	39d46m07.227s	1406	2016-03-18	22.5		22.1
WISPS-409	7d58m45.5009s	46d54m37.5622s	2809	2016-03-19	23.3		22.9
WISPS-41	144d53m17.9827s	69d36m22.2476s	2909	2010-06-14	23.0	22.8	22.6
WISPS-411	284d06m11.8136s	66d22m26.8718s	2309	2016-03-21	22.5		22.2
WISPS-412	348d31m51.5325s	60d03m21.5937s	1606	2016-03-22	22.1		21.8
WISPS-413	246d01m22.4795s	64d16m18.8025s	2309	2016-03-23	24.0		23.6
WISPS-416	246d33m44.1867s	65d08m04.8993s	3912	2016-05-17	23.0		22.7
WISPS-417	191d59m18.038s	41d51m50.9014s	1406	2016-03-30	23.1		22.1

Table 5 *continued on next page*

Table 5 (*continued*)

Pointing	l	b	G141 Exp (s)	Observation Date	Lim F110	Lim F140	Lim F160
WISPS-420	137d07m49.3901s	57d50m12.5969s	4612	2016-04-09	21.9	22.6	21.6
WISPS-422	128d41m25.5655s	55d37m37.7774s	4712	2016-04-13		22.9	
WISPS-425	144d30m36.2173s	84d26m23.8364s	2409	2016-04-19	23.2		22.8
WISPS-427	220d52m39.3643s	45d30m06.2306s	14635	2016-05-06	24.5		24.1
WISPS-428	1d49m56.0154s	60d45m11.5829s	1806	2016-05-05	22.9		22.3
WISPS-43	42d02m17.8471s	-32d47m15.1396s	2809	2010-06-16	24.0	23.1	23.8
WISPS-430	289d00m25.9284s	48d10m09.7165s	4612	2016-05-20	23.5		23.1
WISPS-431	191d09m25.8797s	42d26m11.2638s	1606	2016-05-11	21.9		21.4
WISPS-432	0d43m48.4737s	75d20m46.5543s	1906	2016-05-15	22.2	22.3	
WISPS-433	42d28m12.2153s	78d59m06.7198s	3712	2016-05-16	23.6		23.3
WISPS-434	261d14m58.9697s	64d31m03.4199s	2509	2016-05-20	23.5		23.2
WISPS-435	90d12m39.0017s	55d00m27.6752s	4712	2016-05-25		22.8	
WISPS-436	4d10m04.8508s	81d01m19.484s	2509	2016-05-26	22.5		22.2
WISPS-437	185d54m12.6986s	77d07m36.7918s	1909	2016-06-03		22.1	
WISPS-438	161d17m45.4628s	49d50m47.8451s	4712	2016-06-06		23.0	
WISPS-439	134d45m41.2053s	81d17m43.1378s	3812	2016-06-09	23.2		22.8
WISPS-44	184d52m08.1369s	67d16m16.8103s	4415	2010-06-17	22.7	23.1	22.3
WISPS-440	140d01m26.7768s	53d55m16.1388s	4612	2016-06-09		22.7	
WISPS-441	298d09m59.3528s	80d42m11.146s	3412	2016-06-19	23.0		22.7
WISPS-442	165d07m31.0269s	49d53m12.9162s	2009	2016-06-23		22.0	
WISPS-443	333d28m08.0629s	68d15m46.9292s	2509	2016-06-30	22.5		22.2
WISPS-444	39d34m29.1373s	76d46m59.0899s	2509	2016-07-01	23.0		22.6
WISPS-445	33d13m51.1794s	48d19m05.569s	2509	2016-07-01	23.2		22.7
WISPS-446	4d00m44.9211s	40d00m52.4218s	4112	2016-07-03	23.5		22.9
WISPS-449	356d22m30.1143s	33d41m04.4014s	3112	2016-07-16	23.5		23.1
WISPS-45	294d55m00.0008s	64d04m33.8374s	4812	2010-06-20	22.7	22.2	21.9
WISPS-450	30d18m10.801s	73d08m43.1771s	3812	2016-07-10	23.3		22.9

Table 5 *continued on next page*

Table 5 (*continued*)

Pointing	l	b	G141 Exp (s)	Observation Date	Lim F110	Lim F140	Lim F160
WISPS-451	215d57m41.1663s	80d27m55.2878s	2809	2016-07-16	22.8		22.5
WISPS-452	61d25m35.8377s	59d19m06.7235s	2109	2016-07-18	22.4		22.2
WISPS-453	44d13m45.843s	45d09m37.4636s	3912	2016-07-22	24.5		24.0
WISPS-454	246d11m03.6985s	-54d06m04.3193s	6218	2016-08-01	24.4		23.9
WISPS-456	44d17m00.8638s	57d25m35.6713s	3009	2016-08-10	23.0		22.7
WISPS-457	20d43m56.2909s	49d15m38.2353s	2409	2016-08-11	23.0		22.4
WISPS-458	101d58m53.7361s	59d58m03.8465s	2109	2016-08-13	23.6		23.2
WISPS-46	41d09m46.1193s	-58d14m22.935s	1906	2010-06-20	22.3	22.0	22.0
WISPS-461	205d11m03.063s	-27d07m58.0769s	1406	2016-09-16	22.3		22.0
WISPS-462	206d08m36.8265s	-54d07m59.5172s	3112	2016-09-20	22.5		22.1
WISPS-463	207d43m15.3143s	-34d37m46.8497s	1406	2016-09-22	22.6		22.1
WISPS-464	206d31m34.4167s	-27d26m53.1313s	1406	2016-09-22	22.2		22.0
WISPS-465	211d28m55.4328s	-56d49m52.6827s	2009	2016-09-23	22.2		21.9
WISPS-466	203d51m08.1249s	-54d35m09.0773s	1909	2016-09-24	23.1		22.1
WISPS-467	204d51m12.5556s	-52d50m16.0555s	1206	2016-09-25	22.5		22.1
WISPS-468	151d04m18.4141s	58d37m14.0962s	3009	2016-09-28	22.8		22.5
WISPS-469	176d06m58.2024s	37d04m40.433s	4612	2016-09-29		22.6	
WISPS-47	37d26m21.4362s	83d44m56.6229s	3212	2010-06-25	21.9	21.9	21.5
WISPS-471	175d15m23.2774s	63d22m55.5701s	2609	2016-10-05	23.4		22.7
WISPS-472	191d06m06.7993s	42d33m24.5743s	4215	2016-10-05			22.0
WISPS-473	63d36m12.9816s	-55d24m10.7824s	803	2016-10-11	22.3		22.0
WISPS-474	252d43m31.9984s	67d21m37.9431s	2309	2016-11-04	21.7		21.4
WISPS-476	105d41m48.4885s	57d21m16.3737s	703	2016-11-21	22.5		22.1
WISPS-477	148d21m12.9553s	59d19m34.0088s	1906	2016-12-06	22.5		22.2
WISPS-478	164d56m12.5677s	47d50m25.4586s	3109	2016-12-09	23.3		22.8
WISPS-480	227d55m43.8798s	-30d22m25.4031s	4212	2016-12-23	23.3		22.9
WISPS-481	280d13m01.3509s	45d48m46.3564s	3112	2016-12-22	22.8		22.4

Table 5 continued on next page

Table 5 (*continued*)

Pointing	l	b	G141 Exp (s)	Observation Date	Lim F110	Lim F140	Lim F160
WISPS-482	232d10m43.7925s	-57d40m10.9808s	4318	2016-12-31	23.1		22.7
WISPS-483	174d31m38.9379s	-51d59m50.8383s	3912	2017-01-05	23.8		23.1
WISPS-49	56d44m51.9685s	64d40m54.5777s	2406	2010-07-02	23.2	22.9	
WISPS-5	100d51m27.2544s	54d58m33.0291s	5515	2009-12-20	23.1	22.8	
WISPS-50	73d13m37.98s	-38d28m19.5488s	1906	2010-07-08		22.2	
WISPS-51	59d22m30.8036s	58d38m50.1858s	2006	2010-07-09		22.3	
WISPS-52	42d09m24.3987s	81d18m55.8204s	4218	2010-07-16		22.4	
WISPS-53	66d47m53.8345s	58d19m28.9777s	1806	2010-07-17		22.3	
WISPS-54	77d47m57.0117s	50d17m32.4415s	2006	2010-07-18		22.3	
WISPS-55	287d35m45.8759s	59d52m48.8779s	2809	2010-07-22	22.6	22.3	
WISPS-56	19d50m26.4694s	37d12m11.7511s	4312	2010-07-28		22.5	
WISPS-57	131d25m26.5314s	68d56m12.2941s	4615	2010-07-30		22.4	
WISPS-58	292d56m46.4097s	61d56m54.5761s	4315	2010-08-01		22.2	
WISPS-59	63d54m43.6985s	51d01m31.1233s	4515	2010-08-04		22.8	
WISPS-6	144d20m36.2097s	-47d20m24.6613s	5015	2009-12-24	22.8	22.9	22.5
WISPS-64	348d34m28.0356s	51d23m30.072s	2306	2010-08-17	22.4		22.1
WISPS-65	54d31m08.9384s	45d15m05.1431s	2306	2010-08-19	23.1		22.8
WISPS-66	348d34m26.4218s	51d23m24.4951s	2909	2010-08-22	22.9		22.7
WISPS-68	106d53m47.3527s	-21d04m42.7273s	3009	2010-10-14	24.0		23.3
WISPS-69	14d45m23.7916s	50d09m01.3366s	2309	2010-09-12	22.8		22.4
WISPS-71	58d49m09.8116s	58d30m29.7994s	2009	2011-08-04	22.7		22.4
WISPS-72	58d11m27.5063s	50d18m37.8146s	2609	2010-09-21	23.5	23.5	23.3
WISPS-73	91d41m09.9366s	65d24m50.0281s	2509	2010-09-30	22.6		22.4
WISPS-74	219d48m21.4612s	35d34m17.9533s	2306	2010-10-02	23.1		22.8
WISPS-75	171d17m06.9739s	43d35m27.0099s	1003	2010-10-06			21.5
WISPS-76	102d44m19.5004s	71d10m54.3411s	2006	2010-10-07	22.8		22.3
WISPS-77	100d05m08.7756s	-44d44m20.3622s	1906	2010-10-13			21.5

Table 5 *continued on next page*

Table 5 (*continued*)

Pointing	l	b	G141 Exp (s)	Observation Date	Lim F110	Lim F140	Lim F160
WISPS-79	134d00m06.9281s	-64d53m23.9233s	2809	2010-11-08	22.9		22.5
WISPS-80	133d59m05.9633s	-64d50m27.2583s	2809	2010-11-18	23.3		23.1
WISPS-81	133d59m00.4512s	-64d50m27.096s	2809	2010-11-19	23.2		22.6
WISPS-82	91d51m58.2489s	43d07m48.3724s	2809	2010-11-21			22.0
WISPS-83	134d00m41.2864s	-64d52m13.8975s	2109	2010-11-23	22.3		22.0
WISPS-84	133d59m18.0365s	-64d53m22.856s	2809	2010-11-24	22.9		22.6
WISPS-85	196d10m06.0218s	39d10m41.9065s	1906	2010-11-28			21.7
WISPS-86	167d43m19.8135s	64d59m56.3996s	1806	2010-11-29	22.7		22.1
WISPS-87	171d02m36.9501s	48d52m18.0918s	1906	2010-12-03	22.9		22.3
WISPS-88	223d49m57.3884s	45d03m28.4517s	3615	2010-12-04			21.5
WISPS-89	133d59m30.9096s	-64d50m27.7825s	2809	2010-12-07	23.4		23.0
WISPS-90	127d43m56.323s	-60d20m56.6463s	4812	2010-12-10			22.2
WISPS-91	133d58m11.5593s	-64d53m19.2713s	2209	2010-12-10	22.7		22.3
WISPS-92	219d09m36.2989s	39d58m30.6745s	1806	2010-12-10			21.7
WISPS-93	191d06m46.5877s	82d20m11.1929s	1806	2010-12-23			21.7
WISPS-94	59d53m01.5262s	-41d59m04.743s	3309	2010-12-13	23.3		22.7
WISPS-95	133d57m19.1573s	-64d53m14.663s	2209	2011-01-02	22.8		22.5
WISPS-96	166d03m32.5449s	-60d53m34.31s	11429	2010-12-16	23.9		23.7
WISPS-97	133d57m57.9196s	-64d52m00.5156s	2109	2011-01-16	22.3		21.9
WISPS-98	165d03m24.9011s	51d18m57.8371s	2006	2011-01-22			21.9
WISPS-99	197d48m56.2667s	47d26m53.1188s	3812	2011-01-28	22.2	22.3	21.9

REFERENCES

- Allers, K., Jaffe, D., Luhman, K., et al. 2007, \apj, 657, 511
- Antoja, T., Helmi, A., Romero-Gómez, M., et al. 2018, Nature, 561, 360
- Atek, H., Malkan, M., McCarthy, P., et al. 2010, \apj, 723, 104
- Bahcall, J., & Soneira, R. 1981, \apjs, 47, 357
- Baraffe, I., Chabrier, G., Barman, T., Allard, F., & Hauschildt, P. 2003, \aap, 402, 701
- Bardalez Gagliuffi, D., Burgasser, A., Gelino, C., et al. 2014, \apj, 794, 143
- Bardalez Gagliuffi, D. C., Burgasser, A. J., Schmidt, S. J., et al. 2019, arXiv e-prints, arXiv:1906.04166
- Basri, G. 1998, in Astronomical Society of the Pacific Conference Series, Vol. 134, Brown Dwarfs and Extrasolar Planets, ed. R. Rebolo, E. Martin, & M. Zapatero Osorio, 394–+
- Bate, M., Bonnell, I., & Bromm, V. 2002, \mnras, 332, L65
- Bate, M., Bonnell, I., & Bromm, V. 2003, in Astronomical Society of the Pacific Conference Series, Vol. 287, Galactic Star Formation Across the Stellar Mass Spectrum, ed. J. De Buizer & N. van der Blieck, 427–432
- Belokurov, V., Erkal, D., Evans, N. W., Koposov, S. E., & Deason, A. J. 2018, MNRAS, 478, 611
- Bertin, E., & Arnouts, S. 1996, \aaps, 117, 393
- Bochanski, J., Hawley, S., Covey, K., et al. 2010, \aj, 139, 2679
- Boubert, D., Guillochon, J., Hawkins, K., et al. 2018, MNRAS, 479, 2789
- Boubert, D., Guillochon, J., Hawkins, K., et al. 2018, Monthly Notices of the Royal Astronomical Society, 479, 2789–2795
- Brammer, G., van Dokkum, P., Franx, M., et al. 2012a, \apjs, 200, 13
- Brammer, G. B., van Dokkum, P. G., Franx, M., et al. 2012b, The Astrophysical Journal Supplement Series, 200, 13
- Bromm, V., & Loeb, A. 2003, Nature, 425, 812
- Burgasser, A. 2001, PhD thesis, AA(Department of Physics, California Institute of Technology)
- . 2004, \apjs, 155, 191
- . 2007, \apj, 659, 655
- . 2014a, ArXiv e-prints, arXiv:1406.4887
- Burgasser, A.,Looper, D., Kirkpatrick, J., & Liu, M. 2007, \apj, 658, 557
- Burgasser, A. J. 2014b, arXiv:1406.4887
- Burningham, B., Cardoso, C., Smith, L., et al. 2013, \mnras, 433, 457
- Burrows, A., Hubbard, W., Lunine, J., & Liebert, J. 2001, Reviews of Modern Physics, 73, 719
- Carnero Rosell, A., Santiago, B., dal Ponte, M., et al. 2019, arXiv e-prints, arXiv:1903.10806
- Chabrier, G., & Baraffe, I. 2000, \araa, 38, 337
- Chabrier, G., & Mera, D. 1997, A&A, 328, 83
- Collaboration, T. A., Robitaille, T. P., Tollerud, E. J., et al. 2013, arXiv:1307.6212
- Cruz, K., Kirkpatrick, J., Burgasser, A., et al. 2007a, ArXiv Astrophysics e-prints

- Cruz, K., Reid, I., Kirkpatrick, J., et al. 2007b, *\aj*, 133, 439
- Cushing, M., Tokunaga, A., & Kobayashi, N. 2000, *\aj*, 119, 3019
- Cushing, M., Kirkpatrick, J., Gelino, C., et al. 2011, *\apj*, 743, 50
- Davis, M., Guhathakurta, P., Konidaris, N. P., et al. 2007, *The Astrophysical Journal Letters*, 660, L1
- Day-Jones, A., Marocco, F., Pinfield, D., et al. 2013, *\mnras*, 430, 1171
- de Vaucouleurs, G., & Pence, W. D. 1978, *AJ*, 83, 1163
- Delfosse, X., Tinney, C. G., Forveille, T., et al. 1999, *Astron. Astrophys. Suppl. Ser.*, 135, 41
- Downes, J. J., Briceño, C., Mateu, C., et al. 2014, *MNRAS*, 444, 1793
- Dupuy, T., & Liu, M. 2012, *\apjs*, 201, 19
- Faherty, J. K., Bochanski, J. J., Gagne, J., et al. 2018, *The Astrophysical Journal*, 863, 91
- Freeman, K. C. 1987, *ARA&A*, 25, 603
- Gagné, J., Faherty, J. K., Cruz, K. L., et al. 2015, arXiv:1506.07712
- Gaia Collaboration, Brown, A. G. A., Vallenari, A., et al. 2018, *A&A*, 616, A1
- Gallart, C., Bernard, E. J., Brook, C. B., et al. 2019, *Nature Astronomy*, doi:10.1038/s41550-019-0829-5
- Giavalisco, M., Ferguson, H. C., Koekemoer, A. M., et al. 2004, *The Astrophysical Journal*, 600, L93
- Gould, A., Bahcall, J., & Flynn, C. 1997, *\apj*, 482, 913
- Grogin, N. A., Kocevski, D. D., Faber, S. M., et al. 2011, *ApJS*, 197, 35
- Hardegree-Ullman, K. K., Cushing, M. C., Muirhead, P. S., & Christiansen, J. L. 2019, arXiv e-prints, arXiv:1905.05900
- Hayashi, C., & Nakano, T. 1963, *Progress of Theoretical Physics*, 30, 460
- Haywood, M., Di Matteo, P., Lehnert, M., Katz, D., & Gómez, A. 2013, *\aap*, 560, A109
- Helmi, A., Babusiaux, C., Koppelman, H. H., et al. 2018, *Nature*, 563, 85
- Holwerda, B. W., Trenti, M., Clarkson, W., et al. 2014, *The Astrophysical Journal*, 788, 77
- Hunter, J. D. 2007, *Computing in Science Engineering*, 9, 90
- Ivezić, Ž., Beers, T. C., & Jurić, M. 2012, *ARA&A*, 50, 251
- Jurić, M., Ivezić, Ž., Brooks, A., et al. 2008, *\apj*, 673, 864
- Kerins, E. J. 1997, *A&A*, 328, 5
- Kiman, R., Schmidt, S. J., Angus, R., et al. 2019, *AJ*, 157, 231
- Kimble, R. A., MacKenty, J. W., O'Connell, R. W., & Townsend, J. A. 2008, *Wide Field Camera 3: a powerful new imager for the Hubble Space Telescope*, , , doi:10.1117/12.789581
- Kirkpatrick, J. 2005, *\araa*, 43, 195
- Kirkpatrick, J.,Looper, D.,Burgasser, A.,et al. 2010, *\apjs*, 190, 100

- Kirkpatrick, J., Cushing, M., Gelino, C., et al. 2011, *\apjs*, 197, 19
- Kirkpatrick, J. D., Reid, I. N., Liebert, J., et al. 2000, *The Astronomical Journal*, 120, 447
- Kirkpatrick, J. D., Martin, E. C., Smart, R. L., et al. 2019, *ApJS*, 240, 19
- Koekemoer, A. M., Faber, S. M., Ferguson, H. C., et al. 2011, *ApJS*, 197, 36
- Koppelman, H. H., Helmi, A., Massari, D., Price-Whelan, A. M., & Starkenburg, T. K. 2019, arXiv e-prints, arXiv:1909.08924
- Kümmel, M., Walsh, J. R., Pirzkal, N., Kuntschner, H., & Pasquali, A. 2009, *Publications of the Astronomical Society of the Pacific*, 121, 59
- Kuntschner, H., Kümmel, M., & Walsh, J. R. 2013
- Laughlin, G., Bodenheimer, P., & Adams, F. 1997, *\apj*, 482, 420
- Lawrence, A., & Others. 2007, *\mnras*, 379, 1599
- Leggett, S. K., Ruiz, M. T., & Bergeron, P. 1998, *ApJ*, 497, 294
- Lodieu, N., Espinoza Contreras, M., Zapatero Osorio, M. R., et al. 2017, *Astronomy & Astrophysics*, 598, A92
- Lodieu, N., Burningham, B., Day-Jones, A., et al. 2012, *A&A*, 548, A53
- Lopez-Santiago, J., Montes, D., Crespo-Chacon, I., & Fernandez-Figueroa, M. J. 2006, *The Astrophysical Journal*, 643, 1160
- LSST Science Collaboration, L. S., Abell, P. A., Allison, J., et al. 2009, arXiv:0912.0201
- Luhman, K. L., & Mamajek, E. E. 2012, *The Astrophysical Journal*, 758, 31
- Malhan, K., Ibata, R. A., & Martin, N. F. 2018, *MNRAS*, 481, 3442
- Mamajek, E. E. 2015, *Proceedings of the International Astronomical Union*, 10, 21
- Manjavacas, E., Apai, D., Zhou, Y., et al. 2018, arXiv:1812.03963
- Marocco, F., Jones, H. R. A., Day-Jones, A. C., et al. 2015, *Monthly Notices of the Royal Astronomical Society*, 449, 3651
- Martin, E. C., Mace, G. N., McLean, I. S., et al. 2017, *The Astrophysical Journal*, 838, 73
- Masters, D., McCarthy, P., Burgasser, A., et al. 2012, *\apjl*, 752, L14
- Metchev, S., Kirkpatrick, J., Berriman, G., &Looper, D. 2008, *\apj*, 676, 1281
- Miller, A. A., Kulkarni, M. K., Cao, Y., et al. 2017, *The Astronomical Journal*, 153, 73
- Momcheva, I. G., Brammer, G. B., van Dokkum, P. G., et al. 2016, *The Astrophysical Journal Supplement Series*, 225, 27
- Myeong, G. C., Evans, N. W., Belokurov, V., Sand ers, J. L., & Koposov, S. E. 2018, *ApJL*, 856, L26
- Myeong, G. C., Vasiliev, E., Iorio, G., Evans, N. W., & Belokurov, V. 2019, *MNRAS*, 488, 1235
- Pecaut, M. J., & Mamajek, E. E. 2013, *The Astrophysical Journal Supplement Series*, 208, arXiv:1307.2657

- Pedregosa, F., Varoquaux, G., Gramfort, A., et al. 2012, arXiv e-prints, arXiv:1201.0490
- Pirzkal, N., Sahu, K., Burgasser, A., et al. 2005, *\apj*, 622, 319
- Pirzkal, N., Burgasser, A., Malhotra, S., et al. 2009, *\apj*, 695, 1591
- Reid, I. 2003, *\aj*, 126, 2449
- Reid, I., Kirkpatrick, J., Liebert, J., et al. 1999, *\apj*, 521, 613
- Reylé, C. 2018, *Astronomy & Astrophysics*, 619, L8
- Reyle, C., Delorme, P., Willott, C. J., et al. 2010, *Astronomy and Astrophysics*, Volume 522, id.A112, 15 pp., 522, arXiv:1008.2301
- Ryan, R. E., J., & Reid, I. N. 2016, *AJ*, 151, 92
- Ryan, R. E., Thorman, P. A., Yan, H., et al. 2011, *The Astrophysical Journal*, 739, 83
- Ryan, R. E., Thorman, P. A., Schmidt, S. J., et al. 2017, *The Astrophysical Journal*, 847, 53
- Ryan Jr., R., Hathi, N., Cohen, S., & Windhorst, R. 2005, *\apjl*, 631, L159
- Salvatier, J., Wiecki, T. V., & Fonnesbeck, C. 2016, *PeerJ Computer Science*, 2, e55
- Saumon, D., & Marley, M. 2008, *\apj*, 689, 1327
- Schmidt, S., West, A., Bochanski, J., Hawley, S., & Kielty, C. 2014, *\pasp*, 126, 642
- Schmidt, S., West, A., Hawley, S., & Pineda, J. 2010, *\aj*, 139, 1808
- Schneider, A. C., Cushing, M. C., Kirkpatrick, J. D., et al. 2015, *The Astrophysical Journal*, 804, 92
- Scoville, N., Aussel, H., Brusa, M., et al. 2007, *The Astrophysical Journal Supplement Series*, 172, 1
- Skelton, R. E., Whitaker, K. E., Momcheva, I. G., et al. 2014, *The Astrophysical Journal Supplement Series*, 214, 24
- Skrzypek, N., Warren, S. J., & Faherty, J. K. 2016, *A&A*, 589, A49
- Sorahana, S., Nakajima, T., & Matsuoka, Y. 2018, arXiv:1811.07496
- Spergel, D., Gehrels, N., Baltay, C., et al. 2015, arXiv:1503.03757
- Theissen, C. A., West, A. A., Shippee, G., Burgasser, A. J., & Schmidt, S. J. 2017, *AJ*, 153, 92
- Tokunaga, A., & Kobayashi, N. 1999, *\aj*, 117, 1010
- Tolstoy, E., Hill, V., & Tosi, M. 2009, *ARA&A*, 47, 371
- Van Vledder, I., Van Der Vlugt, D., Holwerda, B. W., et al. 2016, *Monthly Notices of the Royal Astronomical Society*, 458, 425
- Virtanen, P., Gommers, R., Oliphant, T. E., et al. 2019, arXiv e-prints, arXiv:1907.10121
- Waskom, M., Botvinnik, O., Hobson, P., et al. 2014, *seaborn*: v0.5.0 (November 2014), v.v0.5.0, Zenodo, doi:10.5281/zenodo.12710
- York, D., & Others. 2000, *\aj*, 120, 1579